2016

Broad Bandwidth Optical Frequency Combs from Low Noise, High Repetition Rate Semiconductor Mode-Locked Lasers

Anthony Klee
University of Central Florida

STARS Citation

Klee, Anthony, "Broad Bandwidth Optical Frequency Combs from Low Noise, High Repetition Rate Semiconductor Mode-Locked Lasers" (2016). *Electronic Theses and Dissertations*. 4925.
https://stars.library.ucf.edu/etd/4925

BROAD BANDWITH OPTICAL FREQUENCY COMBS FROM LOW NOISE, HIGH REPETITION RATE SEMICONDUCTOR MODE-LOCKED LASERS

by

ANTHONY C. KLEE
B.S. Rose-Hulman Institute of Technology, 2010
M.S. University of Central Florida, 2013

A dissertation submitted in partial fulfillment of the requirements
for the degree of Doctor of Philosophy
in CREOL, The College of Optics and Photonics
at the University of Central Florida
Orlando, Florida

Spring Term
2016

Major Professor: Peter J. Delfyett, Jr.

ABSTRACT

Mode-locked lasers have numerous applications in the areas of communications, spectroscopy, and frequency metrology. Harmonically mode-locked semiconductor lasers with external ring cavities offer a unique combination of benefits in that they can produce high repetition rate pulse trains with low timing jitter, achieve narrow axial mode linewidths, have the potential for entire monolithic integration on-chip, feature high wall-plug efficiency due to direct electrical pumping, and can be engineered to operate in different wavelength bands of interest. However, lasers based on InP/InGaAsP quantum well devices which operate in the important telecom C-band have thus far been relatively limited in bandwidth as compared to competing platforms. Broad bandwidth is critical for increasing information carrying capacity and enabling femtosecond pulse production for coherent continuum generation in offset frequency stabilization. The goal of the work in this dissertation is to maximize the bandwidth of semiconductor lasers, bringing them closer to reaching their full potential as all-purpose sources.

Dispersion in the laser cavity is a primary limiter of the achievable bandwidth in the laser architectures covered in this dissertation. In the first part of this dissertation, an accurate self-referenced technique based on multi-heterodyne detection is developed for measuring the spectral phase of a mode-locked laser. This technique is used to characterize the dispersion in several semiconductor laser architectures. In the second part, this knowledge is applied to reduce the dispersion in a laser cavity using a programmable pulse shaper, and thus increase the laser's spectral bandwidth. We demonstrate a 10 GHz frequency comb with bandwidth spanning 5 THz, representing a twofold improvement over the previously achievable bandwidth. Finally, this laser is converted to a stand-alone system by reconfiguring it as a coupled opto-electronic oscillator and a novel stabilization scheme is presented.

For my wife, Kristina, who helped in innumerable ways to make this dissertation possible

ACKNOWLEDGMENTS

I would like to express my sincere gratitude to my advisor Prof. Peter Delfyett for his guidance and support throughout my dissertation research. I would like to thank my colleagues in the Ultrafast Photonics group with whom I had the privilege of working. They are Dr. Ibrahim Ozdur, Dr. Dimitrios Mandridis, Dr. Umar Piracha, Dr. Nazanin Hoghooghi, Dr. Josue Davila-Rodriguez, Dr. Charles Williams, Dr. Dat Nguyen, Dr. Marcus Bagnell, Dr. Sharad Bhooplapur, Dr. Abhijeet Ardey, Dr. Edris Sarailou, Kristina Bagnell, Javed Talukder, Abdullah Zaman, Mina Bayat, and Michael Plascak. Lastly, I would like to thank all my friends, and specifically Dr. Matthew Reichert and Dr. Matthew Mills, for supporting and motivating me and making graduate school a wonderful experience.

TABLE OF CONTENTS

LIST OF FIGURES

LIST OF TABLES

LIST OF ACRONYMS/ABBREVIATIONS

A/D	Analog-to-Digital
CFBG	Chirped Fiber Bragg Grating
COEO	Coupled Opto-Electronic Oscillator
CW	Continuous Wave
DCF	Dispersion Compensating Fiber
FFT	Fast Fourier Transform
FPE	Fabry-Pérot Etalon
FSR	Free Spectral Range
FTS	Fourier Transform Spectroscopy
MLL	Mode-Locked Laser
OE	Opto-Electronic
OEO	Opto-Electronic Oscillator
OFC	Optical Frequency Comb
PDH	Pound-Drever-Hall
RF	Radio Frequency
SCOWA	Slab Coupled Optical Waveguide Amplifier
SMF	Single Mode Fiber
SOA	Semiconductor Optical Amplifier
SNR	Signal-to-Noise Ratio
VOD	Variable Optical Delay

CHAPTER 1: INTRODUCTION

Mode-locked lasers are invaluable tools for studying the physical world due to their unique temporal and spectral properties. As seen in Figure 1.1, the output of a fundamentally mode-locked laser is a periodic train of pulses with a repetition rate, f_{rep}, defined by the cavity round trip time, t_{Cav}. From pulse to pulse, the carrier electric field may develop a lag or lead with respect to the peak of the pulse envelope, known as the carrier-envelope offset, as a result of differences between the phase and group velocities. The optical spectrum of this periodic signal is composed of a set of phase-locked longitudinal modes evenly spaced by the repetition rate frequency. Bearing resemblance to teeth on a comb, this set of frequencies is often called an optical frequency comb (OFC). If this set of comb lines were to extend down to zero frequency, one would find the lowest frequency comb line to lie between zero and f_{rep} at some offset frequency, f_{ceo}, as a result of the carrier-envelope offset. Control of these two parameters, f_{rep} and f_{ceo}, can provide knowledge of the absolute frequency of each comb line with mHz accuracy [1]. Using an f-$2f$ interferometer, the offset frequency can be detected and stabilized to an ultra-low noise microwave oscillator [2]. Furthermore, phase locking a single comb line to a stable CW laser – which is in turn locked to a high-Q optical cavity or ultra-fine atomic transition – can transfer the stability and linewidth of the CW laser to each of the comb lines, thus effectively pinning both degrees of freedom and enabling production of more than 10^5 coherent comb lines with sub-Hz linewidth and absolute frequency stability [3, 4].

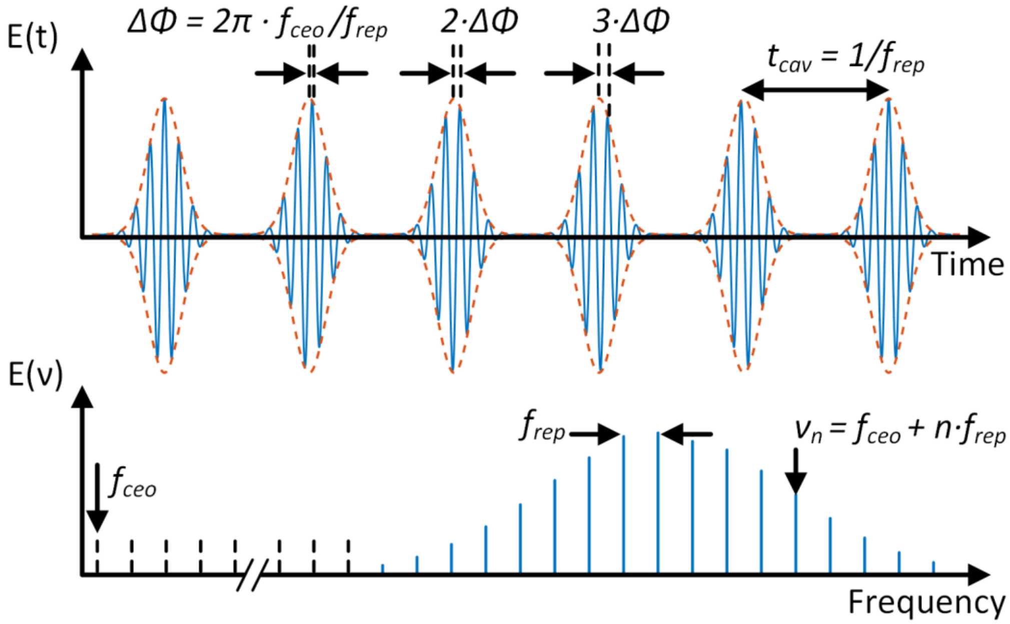

Figure 1.1 Mode-locked laser output in time and frequency. The periodic nature of the pulse train corresponds to a set of evenly spaced frequency components in the optical domain, an optical frequency comb, with comb line spacing of f_{rep} and offset frequency of f_{ceo}.

1.1 Applications of Mode-Locked Lasers

Since the first demonstration of a He-Ne mode-locked laser (MLL) in 1964 [5], mode-locked lasers have garnered significant interest for their usefulness in a wide variety of applications. The ability of mode-locked lasers to generate femtosecond pulses at gigahertz rates with ultralow timing jitter has enormous benefits for timing-based applications like photonic analog-to-digital (A/D) conversion and laser radar. Additionally, frequency domain applications such as spectroscopy and astronomical spectrograph calibration leverage the well-defined, periodic nature of a mode-locked laser’s optical spectrum.

1.1.1 Time Domain: Photonic Sampled Analog-to-Digital Conversion

Naturally occurring signals in the world (e.g. light and sound) which are continuous in time and amplitude are known as analog signals. Information can be transmitted via analog signals, and indeed communication via analog means has been the most common method for much of mankind's history. Digital signals which are discrete in time and quantized in value have also existed throughout time in various forms like smoke signals or the electric telegraph. However, since the birth of the transistor in the mid-20th century, there has been an explosion in the prevalence of digital signals [6].

Compared to analog communications, digital transmission offers a key advantage which has led to its dominance of modern telecommunications. Namely, digital signals do not suffer the noise degradation that analog signals do when amplified, transmitted, or processed [7]. This allows digital signals to be manipulated while maintaining high fidelity, key for achieving low error rates. In addition, digital signal processing techniques have been developed which enable a host of now-common applications such as face or voice recognition, data compression, and medical imaging [8].

Despite the utility of digital communications, there is still a need to transmit signals from analog phenomena. In order to harness the benefits of digital transmission and signal processing while representing analog signals, an analog-to-digital converter can be employed. An A/D converter digitizes analog signals through the two-step process of sampling and quantization. In sampling, the analog signal's amplitude is periodically measured and then sustained or held for short amount of time. The sampled value is subsequently quantized or rounded to the nearest allowed voltage level. The output digitized signal does not perfectly reproduce the input analog signal due to the analog signal continuously varying during each quantized sample period, giving rise to what is known as quantization error. Figure 1.2 shows several examples of the quantization error arising in the A/D conversion process for various sampling rates and resolution levels. Note that both appropriate resolution and sampling rate are needed for accurate representation of the analog signal.

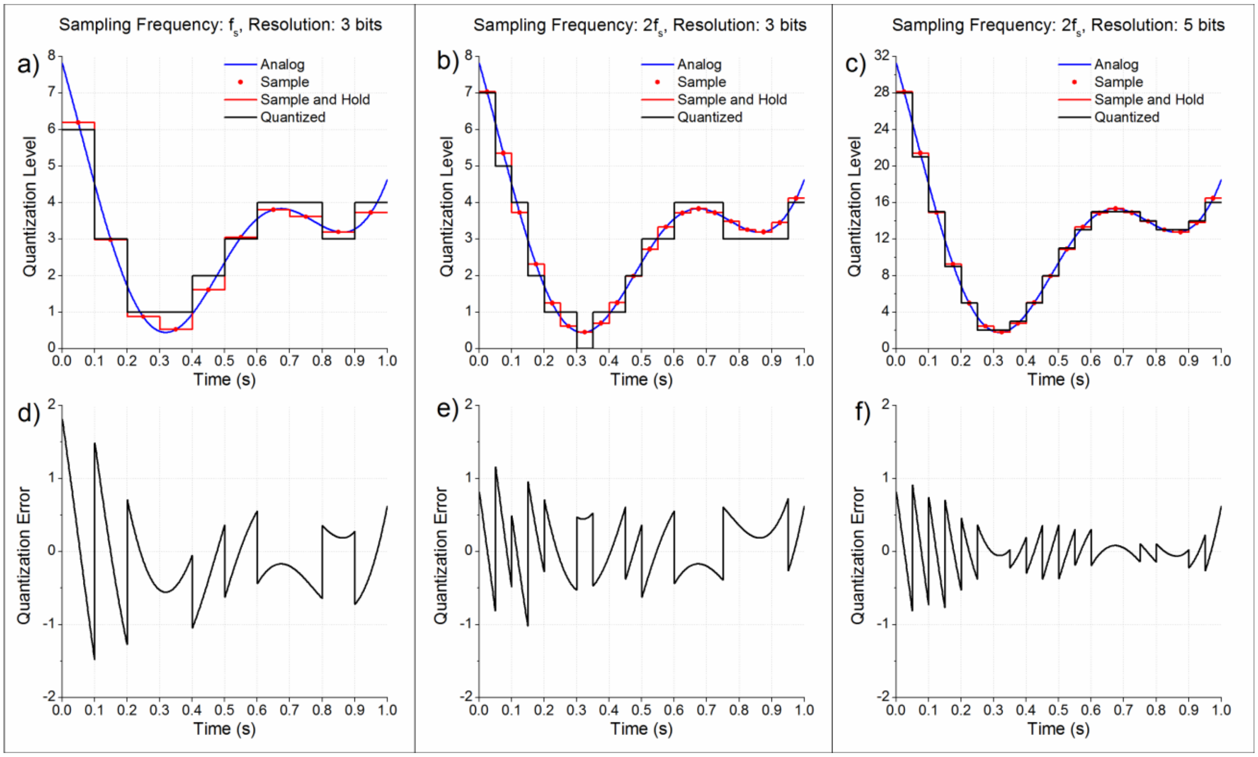

Figure 1.2 A/D Conversion and Quantization Error. a) A/D conversion with sampling frequency of f_s and 3 bits of resolution or 8 quantization levels. b) A/D conversion with sampling frequency $2{\cdot}f_s$ and 3 bit resolution. c) Sampling frequency $2{\cdot}f_s$ and 5 bit resolution (32 levels). d), e), and f) show the quantization error from the A/D converters in a), b), and c), respectively

Traditional A/D converters utilize all-electronic sampling and quantization, but with new advances in optical technologies, photonics have begun to support, and in some cases replace, these electronic functions [9]. So-called photonic A/D converters can be broadly divided into four categories: photonic assisted, in which photonics do not directly execute either function but rather aid the overall system performance [10]; photonic sampled, wherein the sampling function is performed via optical means [11]; photonic quantized, in which the quantization is achieved using optics [12]; and photonic sampled and quantized, where both functions are performed optically [13]. The primary focus of the work in this dissertation is on photonic sampled A/D converters.

A simple illustration of the basic operation of a photonic sampled A/D converter can be seen in Figure 1.3. A mode-locked laser produces a high repetition rate, low timing jitter optical pulse train which samples the analog RF waveform, most commonly via an electro-optic intensity modulator. The modulated pulse train is demultiplexed, photodetected, and quantized to produce a digital representation of the original signal. Demultiplexing the pulse train allows the detection and quantization electronics to operate at lower, more easily achievable processing rates.

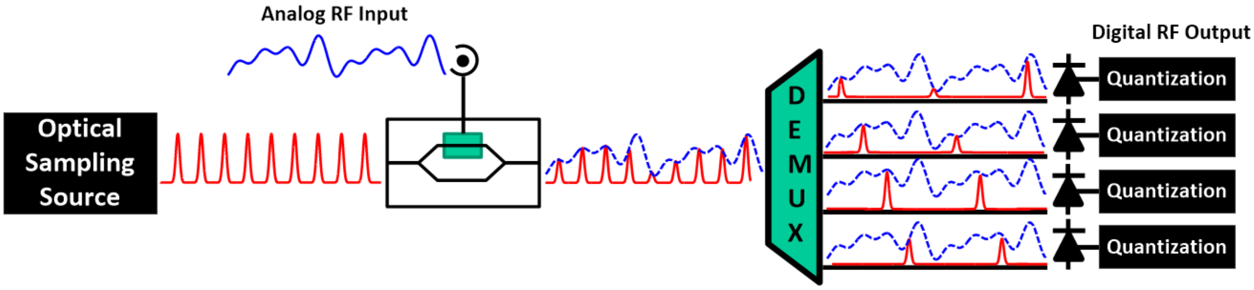

Figure 1.3 General schematic of a photonic sampled A/D converter. The DeMux can be either a temporal or wavelength demultiplexer. Wavelength demultiplexing requires a multi-wavelength optical source, while temporal demultiplexing requires multiple cascaded demultiplexers with timing synchronization. The setup is simplified here for illustrative purposes.

As demonstrated in Figure 1.2 above, high sampling rates are needed to accurately convert rapidly varying analog signals to digital with minimal quantization error. As sampling speeds reach GHz rates and higher, electronic sampling sources increasingly suffer from noise affecting the pulse-to-pulse timing and amplitude, which in turn reduces the effective resolution of the A/D converter. Herein lies the true benefit of using mode-locked lasers for sampling, as they can produce GHz pulse trains with femtosecond levels of timing jitter or better [14], enabling high speed, high resolution A/D conversion. Additionally, mode-locked lasers can easily generate pulses with picosecond or shorter durations, much shorter than electrical sampling pulses, reducing the sampling gate duration and increasing resolution.

1.1.2 Frequency Domain: Dual Comb Spectroscopy

An interesting, relatively new application of mode-locked lasers is in the field of spectroscopy. While mode-locked lasers have long been utilized in this area, a recent advancement has been the development of multi-heterodyne or dual comb detection. By mixing two optical frequency combs from mode-locked lasers with slightly different repetition rates, one can downconvert and compress optical spectra containing information about a sample’s absorption and dispersion into radio frequency bands. A simplified schematic of a typical dual comb spectrometer is shown in Figure 1.4. The signal frequency comb output is split with one branch probing a sample or device under test and the other serving as a baseline. Each arm is then mixed with the local oscillator comb and photodetected. The Fourier spectra are calculated from the resulting interferograms, and the signal spectrum is normalized by the reference spectrum to retrieve the absorption and dispersion of the sample [15].

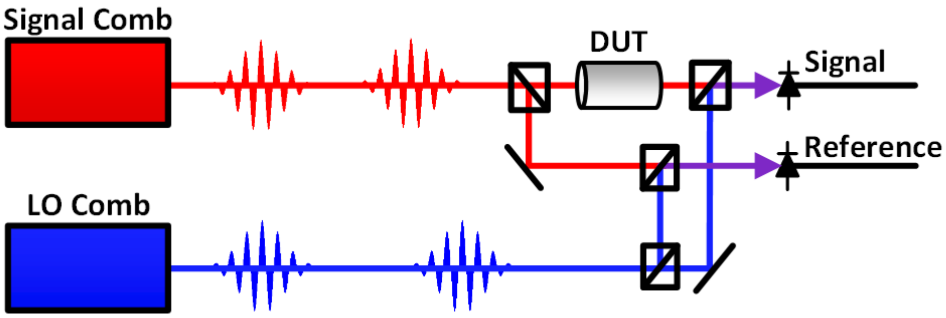

Figure 1.4 Dual comb spectroscopy setup. The high repetition rate signal comb is split to both probe a device under test (DUT) and provide a baseline reference. The signal comb is combined with a lower repetition rate local oscillator comb for multi-heterodyne detection.

Dual comb spectroscopy has several advantages as compared to conventional Fourier transform spectroscopy (FTS). If frequency combs with stabilized repetition rate and offset frequency are used, one may have knowledge of the absolute frequency of each comb line with better than 10^{-12} accuracy, representing four orders of magnitude improvement over the frequency accuracy of FTS [16]. Additionally, as phase-locking a comb line to a cavity-stabilized CW laser transfers the stability and linewidth of the reference laser to each comb line, frequency resolution on the Hz scale is possible, which exceeds that of FTS by six orders of magnitude [15]. Though in a single scan, frequency sample spacing is set by the repetition rate of the laser, several scans in which the offset frequency has been tuned can be coherently stitched together to achieve sampling with linewidth-limited resolution. Finally, the removal of any moving parts enables fast acquisition times in the μs regime and eliminates mechanical instability contributions to the signal-to-noise ratio.

Dual comb spectroscopy faces several challenges. Transformation of a single interferogram period yields a comparatively low signal-to-noise ratio due to fluctuations in the laser repetition rates and carrier-envelope offset phase [16]. To achieve a high signal-to-noise ratio, several avenues have been explored. The comb sources can be locked to a stable CW laser to allow coherent averaging over long time scales (~1s) which increases the signal-to-noise ratio quadratically with averaging time [15-18], but this method greatly increases the complexity of the experimental setup and requires two state-of-the-art frequency combs. Alternatively, a reference signal derived from heterodyne beats from within a narrow optical band [19] or with an external CW laser [20] can be used in post-processing to correct for any fluctuations in time scale, though this prevents real-time operation. A third technique known as adaptive clocking uses a trigger signal proportional to the heterodyne beat between a single comb line from each comb to sample the interferogram on a non-uniform spacing that cancels any timing or phase fluctuations [21, 22]. Though the electronics required to generate the clocking signal increase the system complexity, this approach allows for real-time operation with free-running comb sources. As a note, in cases of a gaseous sample, the signal-to-noise ratio can also be improved by placing the sample in a resonant cavity to increase the interaction length with the signal comb [23]. The timing and phase fluctuations must still be addressed with one of the previously mentioned methods however. Spectral bandwidth and coverage is another area needing improvement. There are a wealth of comb sources in the visible and near-IR, but there are a lack of convenient sources in the important mid-IR molecular fingerprint regime, let alone sources that span UV to mid-IR.

Despite its complexities, dual comb spectroscopy is generating much interest due to the compelling results obtained, such as absorption and phase spectra of CO_2, CH_4, C_2H_2, and H_2O over 43 THz of optical bandwidth being demonstrated with a Signal-to-Noise Ratio (SNR) >3000 and sensitivity of 10^{-4} [24]. The technique has been field-deployed, with demonstrations of open-path spectroscopy of greenhouse gases over 2 km in air yielding quantitative measurements of molecular concentrations [25]. DCS has been extended into nonlinear spectroscopy as well with the development of Raman-induced Kerr-effect dual-comb spectroscopy [26] and dual-comb two-photon excitation spectroscopy [27]. Increasing the bandwidth and stability of optical frequency comb sources could improve these results and will aid in the continued advancement of dual comb spectroscopy.

1.2 Harmonically Mode-Locked Semiconductor Lasers

Harmonically mode-locked semiconductor lasers are exceptionally well-suited to address the requirements of the previously discussed applications as well as many others. Harmonic mode-locking enables the necessary high repetition rates while simultaneously maintaining narrow linewidth longitudinal modes, vital for ensuring low timing jitter sampling and high resolution spectroscopy. As described by the Schawlow-Townes equation [28], narrow linewidth modes can be achieved by increasing the cavity storage time. However, increasing the cavity length necessarily results in a reduced repetition rate. To achieve GHz repetition rates with long cavity lengths (~50 m), one can harmonically mode-lock the laser by driving a Mach-Zehnder intensity modulator in the cavity at a multiple of the fundamental frequency.

As seen in the center panel of Figure 1.5, the output of a harmonically mode-locked laser in the time domain consists of pulses spaced by the modulation or mode-locking period while the spectrum contains modes spaced by the cavity fundamental frequency. One interpretation of this output is that for a laser mode-locked at the N^{th} harmonic, N pulses are simultaneously oscillating in the laser cavity and each pulse generates its own pulse train that is interleaved with the other pulse trains. This interleaved pulse trains picture, depicted in the left panel of Figure 1.5, corresponds to multiple overlapping and interfering spectra in the frequency domain. Another interpretation of harmonic mode-locking is illustrated in the right panel of Figure 1.5, in which energy is shared between every N^{th} mode spaced by the mode-locking frequency. This creates N interleaved supermodes, or sets of phase-locked axial modes, offset from each other by the cavity fundamental frequency. In the time domain, this is equivalent to multiple overlapping and interfering pulse trains with periods equal to the modulation period.

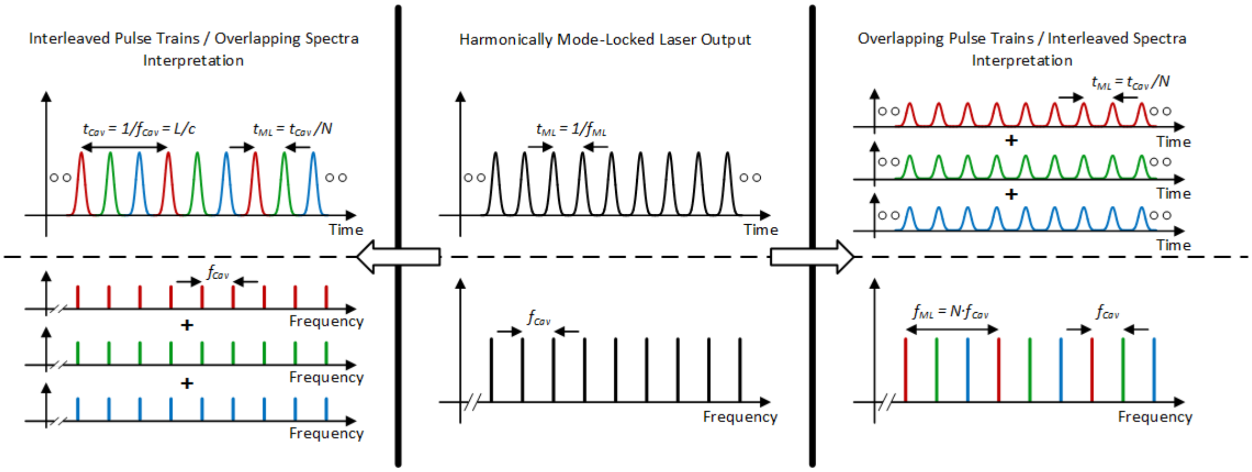

Figure 1.5 Two interpretations of a harmonically mode-locked laser output. t_{ML} and f_{ML} indicate mode-locking period and frequency, respectively. t_{Cav} and f_{Cav} indicate the cavity round trip time and fundamental frequency, respectively. N is the harmonic mode-locking order.

A side effect of the harmonic mode-locking process is the introduction of supermode noise. This noise, which manifests itself in the output pulse train as timing jitter and pulse-to-pulse energy fluctuations at multiples of the cavity round trip time, arises from multiple supermodes simultaneously oscillating and competing for gain [29]. One strategy to select a single supermode for oscillation and mitigate this noise source is through injection locking with a narrow linewidth CW laser [30]. The supermode containing the injection locked cavity mode is preferentially amplified while gain depletion leads to the other supermodes being suppressed. This architecture is further explored in Section 3.2. Another supermode suppression scheme, upon which the majority of the work in this dissertation is based, is the coupling of the laser cavity to a second optical cavity with resonances spaced by an amount equal to the mode-locking rate [31]. The second cavity acts to filter out all but a single supermode for lasing. This is the basis for the lasers in Sections 3.3 and 3.4, and will be discussed in detail in Section 4.1.

The use of semiconductor gain in harmonically mode-locked lasers has a number of beneficial features. Due to the fast gain recovery times, semiconductor lasers have been shown to be effective sources of pulse trains with femtosecond level timing jitter even at multi-GHz repetition rates [14, 32]. These external cavity laser systems have the potential for complete monolithic integration thanks to advances in the development of long, low loss waveguides on chip [33, 34]. These features, along with the inherent high wall-plug efficiency due to direct electrical pumping, make semiconductor based lasers attractive sources to improve the performance and reduce the overall size, weight, and power consumption of larger, multi-component systems. Finally, the ability to engineer the bandgap energy of the gain medium make semiconductor lasers extremely wavelength agile and applicable for use in many spectral regions of interest.

One drawback of lasers based on semiconductor gain is their relatively narrow bandwidth as compared to other common frequency comb sources. For many applications, a broad bandwidth is desirable as it allows for shorter pulses, a greater number of data channels and total information-carrying capacity, or detection capabilities over a wider range. In Figure 1.6 below, the achievable spectral coverage and repetition rates are depicted for several different common comb sources in the visible and near-infrared spectrum, based on data from [35-48]. The solid-state Ti:Sapphire mode-locked laser is capable of directly producing an octave spanning spectrum in the 100 MHz to 1 GHz repetition rate range, though the bandwidth rapidly decreases for higher repetition rates. Fiber based comb sources such as Yb:fiber and Er:fiber are generally limited to lower repetition rates due to the need for long gain sections and the output spectrum is also relatively narrow but can be broadened outside the cavity in highly nonlinear fiber. Recent advances in microresonator technology have led to interest in so-called Kerr combs generated by cascaded four-wave mixing. These comb sources can produce extremely broad spectra with THz mode spacing, but as the resonator size is increased to reduce the mode spacing to more accessible levels, the tight confinement of the devices required for nonlinear broadening is reduced and the bandwidth shrinks. In contrast, semiconductor sources have been limited to bandwidths of approximately 20 nm, but can operate over an extremely wide range of repetition rates from 100 MHz to 100 GHz. Many applications of interest rely on sources with repetition rates in this range, such as spectroscopy which benefits from the high frequency domain sampling density of 100 MHz sources or optical arbitrary waveform generation which benefits from multi-GHz sources for line-by-line pulse shaping. Semiconductor lasers are thus widely applicable, yet more work is required to increase their bandwidth and maximize their utility.

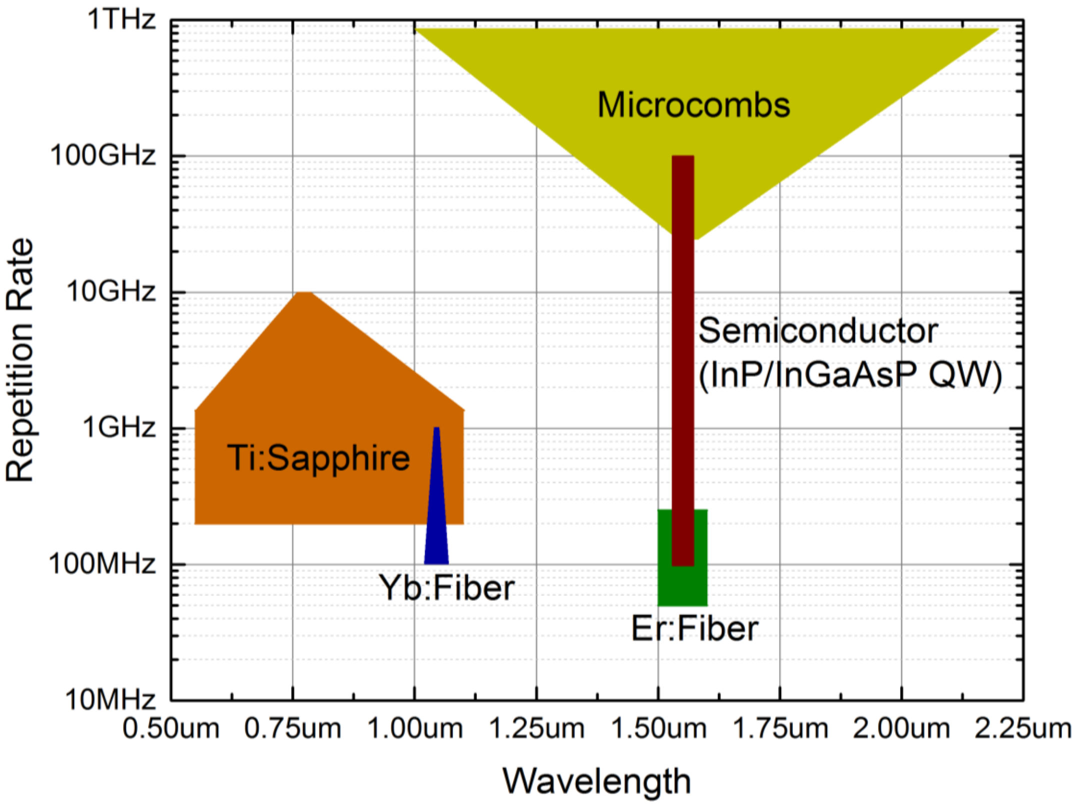

Figure 1.6 Comparison of common comb sources in the visible and near-infrared spectrum.

1.3 Dissertation Outline

In the following chapters of this dissertation, progress toward increasing the bandwidth of harmonically mode-locked semiconductor lasers is described. CHAPTER 2: covers a novel dual-comb measurement technique developed to study the dispersion characteristics of our lasers. The theoretical background of the technique, the self-referenced spectral amplitude and phase retrieval algorithm, and a verification of the method's accuracy are all presented. In CHAPTER 3:, the measurement technique is applied to three different representative mode-locked lasers and the results are analyzed to understand the role which key cavity elements play in limiting the spectral bandwidth. CHAPTER 4: explains the architecture of a new laser system with programmatic control of the intracavity dispersion and gain profiles. Applying the knowledge gained in CHAPTER 3:, the cavity dispersion is optimized to achieve unprecedented performance in terms of bandwidth obtained directly from a GHz semiconductor laser. CHAPTER 5: details work to convert the laser system of CHAPTER 4: to a coupled opto-electronic oscillator, eliminating the need for an external radio frequency synthesizer and making the oscillator a true stand-alone system. A novel stabilization scheme leveraging the broad spectral bandwidth offers the potential for photonic generation of ultralow phase noise microwave signals. A concluding summary and recommendations for future work are contained in CHAPTER 6:.

CHAPTER 2: SELF-REFERENCED MULTI-HETERODYNE PHASE RETRIEVAL ALGORITHM

Multi-heterodyne or dual-comb detection was first proposed in 2002 by Schiller [49] and successfully demonstrated in 2004 by Keilmann and colleagues [50]. The technique was originally intended for spectroscopy applications and indeed today that is its primary use, though it has been adapted for other purposes as well such as length metrology and optical coherence tomography [51]. A notable advancement was made in 2008 by Coddington and coworkers at NIST who used stabilized frequency combs [52] to achieve comb line-resolved Fourier spectra from a multi-heterodyne interferogram [15]. This was a significant step toward the high resolution measurements promised by multi-heterodyne detection, and since then the technique has experienced a rapid growth in interest and attention.

Of interest to this dissertation is the ability to use multi-heterodyne detection to make measurements of the complex spectrum of optical frequency combs. That is to say, multi-heterodyne detection can be used to study comb sources themselves rather than the changes imposed on the combs by a spectroscopy sample. In this way, the spectral phase of a frequency comb from a mode-locked laser can be characterized and compensated to reduce net cavity dispersion and increase the lasing bandwidth.

The first demonstration of using multi-heterodyne detection to characterize a comb source's spectral phase and ultimately measure the source's time-domain waveform profile utilized frequency combs with closely matched mode spacings generated from cascaded modulation of a common CW laser [53]. The magnitude and phase of one comb were flattened using a line-by-line spectral shaper to form a perfect reference comb, and the signal comb was shaped to provide interesting waveforms for measurements. Good agreement between the retrieved and applied phase profiles was demonstrated, with standard deviation between the two on the order of 0.1π radians [53]. This technique was subsequently advanced to allow the two sources to be mutually incoherent, providing more flexibility and opening up new applications [54]. Additionally, it was shown that multi-heterodyne detection could be used to not only measure pulse trains from mode-locked lasers, but also the output from phase-modulated CW lasers and periodically filtered white light [54]. Here again, the reference comb was taken to be a perfect reference with flat magnitude and phase.

The requirement of one comb acting as a perfect reference arises from the fact that the magnitude and phase information of both combs are coupled in the downconverted spectrum. In order to isolate the spectrum of the signal comb, the reference comb was taken to have flat magnitude and phase profile such that the lowest frequency beat set in the RF spectrum was an exact scaled copy of the optical comb of interest [53, 54]. However, by utilizing higher frequency copies of the baseband spectrum, self-referenced measurements of the complex spectrum of each comb source can be simultaneously retrieved using a non-iterative algorithm, thus eliminating the requirement of a perfect reference comb [55, 56].

One challenge for self-referenced multi-heterodyne measurements is the requirement for high speed detection and digitizing electronics [55, 56]. To minimize the RF bandwidth required for self-referenced retrieval, the repetition rate of one comb can be reduced to a small subharmonic of that of the comb of interest [57], though this increases the complexity of the retrieval algorithm. In this chapter, the mathematical basis for the generalized retrieval algorithm for both combs is presented and its accuracy is experimentally verified.

2.1 Multi-heterodyne Background

In simplest terms, multi-heterodyne detection is the mixing of two slightly different optical frequency combs such that an easily characterized electrical frequency comb is produced upon photodetection of the combined signal. To see this, consider two optical frequency combs, Comb A and Comb B, with comb lines occurring at $\nu_n^{(A,B)} = \nu_o^{(A,B)} + n \cdot f_{rep}^{(A,B)}$, where ν_n is the frequency of the n^{th} comb line, ν_o is the lowest frequency comb line in the lasing spectrum (not to be confused with the carrier-envelope offset frequency), f_{rep} is the mode spacing or repetition rate, and superscripts refer to the comb source. Let the complex amplitude of the $\nu_n^{(A)}$ ($\nu_n^{(B)}$) comb line be given by $A_n e^{i\alpha_n}$ ($B_n e^{i\beta_n}$). Assume $f_{rep}^{(A)}$ and $f_{rep}^{(B)}$ are not equal, nor exact harmonics of each other, and take $f_{rep}^{(B)}$ to be the larger of the two. If the two combs occupy the same spectral region, then the combined optical spectrum consists of interleaved combs where the spacing between comb lines from Comb B and the nearest frequency neighbor from Comb A changes across the spectrum, as seen in Figure 2.1. In general, $f_{rep}^{(B)}$ may be several times larger than $f_{rep}^{(A)}$, resulting in multiple comb lines from Comb A falling between any two adjacent comb lines of Comb B. Here it is useful to define the subharmonic order, or integer ratio of repetition rates, as $N_H = \left\lfloor f_{rep}^{(B)} / f_{rep}^{(A)} \right\rfloor$.

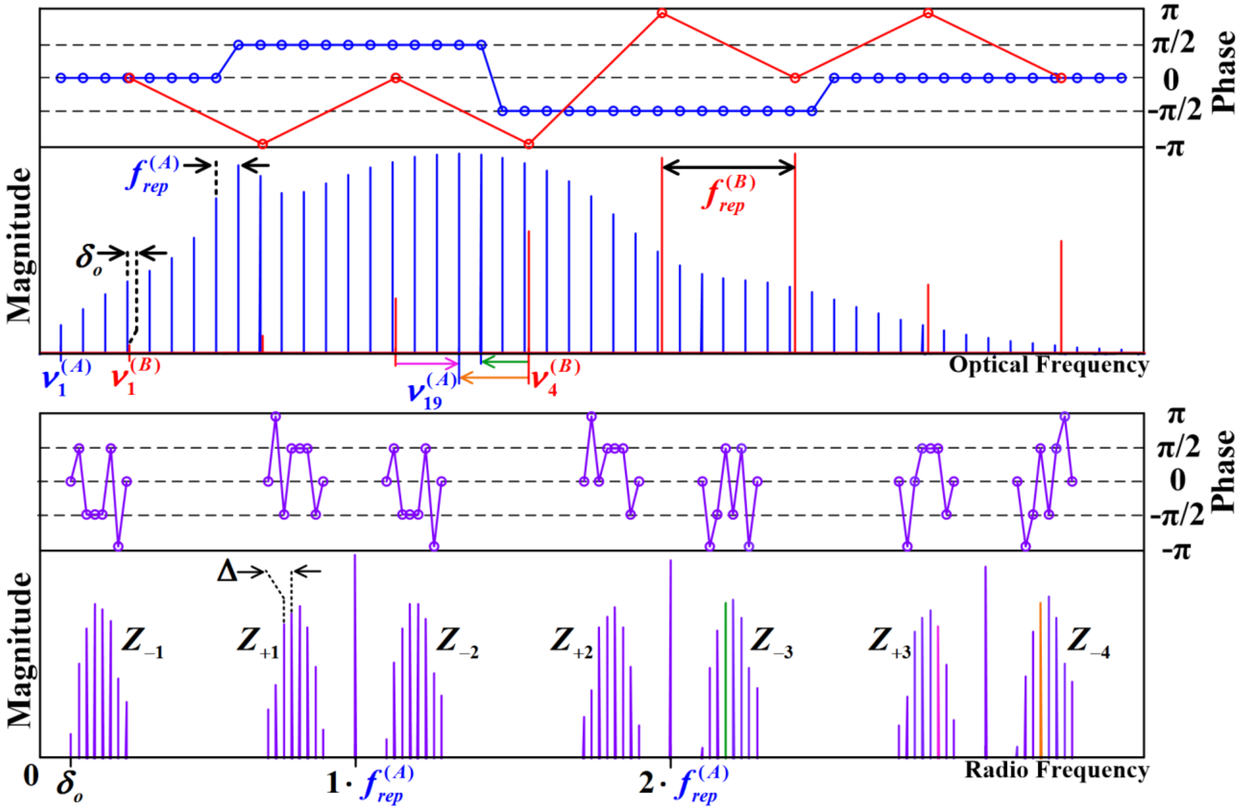

Figure 2.1 Sample multi-heterodyne optical spectrum (top) and RF spectrum (bottom). Comb A (Comb B) is shown in blue (red) with low (high) repetition rate $f_{rep}^{(A)}$ ($f_{rep}^{(B)}$). RF beats are spaced by the effective repetition rate difference, $\Delta = f_{rep}^{(B)} - N_H \cdot f_{rep}^{(A)}$, where N_H is the harmonic order or integer ratio of repetition rates $\left(\left\lfloor \boldsymbol{f_{rep}^{(B)}} / \boldsymbol{f_{rep}^{(A)}} \right\rfloor\right)$ which is equal to 6 in this example. The number of comb lines in Comb B, N_B, is chosen to be 8 here.

Upon photodetection, the mixing products of the two combs are generated as seen in the RF spectrum in Figure 2.1, producing intra-comb heterodyne beat tones at $f_{rep}^{(A)}$, $f_{rep}^{(B)}$, and their harmonics and inter-comb heterodyne beat tones at a multitude of RF frequencies which group into distinct sets provided the carrier-envelope offset frequency and repetition rate of each comb are chosen carefully. Within a given inter-comb beat set, the inter-comb beats are spaced by the effective repetition rate difference $\Delta = f_{rep}^{(B)} - N_H \cdot f_{rep}^{(A)}$, with the first beat occurring at δ_o, the frequency difference between the nearest two optical comb lines. The origin of each of the RF beat sets can be traced to distinct comb line pairs in the optical domain. For optical spectra such as that in Figure 2.1 where the frequency separation between Comb B and the nearest comb line from Comb A increases with optical frequency, the lowest frequency beat set, Z_{-1}, consists of beats between each comb line of Comb B and the closest lower frequency comb line from Comb A. The second set, Z_{+1}, arises from Comb B beating with the closest higher frequency comb line from Comb A. Subsequent sets continue this pattern, resulting from Comb B beating with the second closest lower and higher frequency lines from Comb A and so forth. As an example, consider the beat indicated with a green arrow between the fourth comb line in Comb B ($\nu_4^{(B)}$) and the twentieth comb line in Comb A ($\nu_{20}^{(A)}$). $\nu_{20}^{(A)}$ is the third closest lower frequency comb line to the fourth comb line in Comb B, and thus the beat between these two produces the RF tone $Z_{-3}(4)$ shown in green, where $Z_{-3}(4)$ refers to the complex amplitude of the fourth beat in the Z_{-3} set. Being the product of comb lines from each comb, the RF beat frequencies contain the spectral magnitude and phase information of both sources. The magnitude of $Z_{-3}(4)$ is the product of the magnitudes of $\nu_{20}^{(A)}$ and $\nu_4^{(B)}$, $A_{20} \cdot B_4$, and the phase of $Z_{-3}(4)$ is the optical phase difference, β_4-α_{20}.

As will be seen in the following treatment, it is vital that each inter-comb beat is uniquely determined by a single pair of optical comb lines which can be ensured through proper choice of $\nu_o^{(A,B)}$ and $f_{rep}^{(A,B)}$. To prevent aliasing of the beat tones, which can lead to multiple optical pairs contributing to the same beat frequency, all beats between Comb B comb lines and the nearest low frequency neighbor from Comb A must fall below $f_{rep}^{(A)}/2$, satisfying the condition of Equation (2.1), where N_B is the number of optical comb lines in Comb B. The number of comb lines in Comb B will be less than the number of comb lines in Comb A for all cases of interest.

$$(\boldsymbol{N_B} - \mathbf{1})\Delta + \boldsymbol{\delta_o} < \frac{\boldsymbol{f_{rep}^{(A)}}}{\mathbf{2}} \qquad (2.1)$$

If this condition is satisfied, then it can be seen that the RF beat tones group into sets contained between half-multiples of $f_{rep}^{(A)}$. Using the definition of Δ, Equation (2.1) can be recast to give an upper limit on Δ independent of $f_{rep}^{(A)}$. The lower limit on Δ is given by the linewidth of the RF beats, requiring that the beats do not overlap one another. These limits are described in Equation (2.2). For a fixed Δ, the maximum optical bandwidth that can be sampled without aliasing is then given by Equation (2.3).

$$LW_{RF} < \Delta < \frac{f_{rep}^{(B)} - 2N_H\delta_o}{2N_H(N_B - 1) + 1} \qquad (2.2)$$

$$BW_{opt} = \frac{f_{rep}^{(A)} \cdot f_{rep}^{(B)}}{2\Delta} \qquad (2.3)$$

2.2 Amplitude and Phase Retrieval Algorithm

2.2.1 Retrieval Algorithm Equations

Once a suitable multi-heterodyne signal (as described in Section 2.1) has been obtained, the RF beat sets can then be manipulated to retrieve simultaneous, independent measurements of the spectral magnitude and phase of each optical frequency comb. The essence of the retrieval algorithm is referencing each RF beat tone against a counterpart which contains information about a common optical comb line [57]. Returning to Figure 2.1, taking the ratio of $Z_{-4}(4)$ – the beat between $\nu_4^{(B)}$ and $\nu_{19}^{(A)}$ shown in orange – to $Z_{-3}(4)$ cancels the contribution of $\nu_4^{(B)}$ to yield the relationship between $\nu_{19}^{(A)}$ and $\nu_{20}^{(A)}$. Likewise, the ratio of $Z_{-4}(4)$ to $Z_{+3}^{*}(6)$ – the conjugate of the beat between $\nu_3^{(B)}$ and $\nu_{19}^{(A)}$ shown in pink – cancels $\nu_{19}^{(A)}$ to yield the relationship between $\nu_3^{(B)}$ and $\nu_4^{(B)}$.

For a large number of comb lines, the retrieval algorithm can be most easily visualized by considering a double-sided RF spectrum, where the negative frequency components are the complex conjugates of the positive components due to the photodetected intensity being a purely real signal. Translating a copy of the RF spectrum by $f_{rep}^{(A)}\left(f_{rep}^{(B)}\right)$ and taking the ratio of overlapping beats in a specific order then results in the adjacent comb line relationships over the spectrum of Comb A (Comb B) within the region of overlap [57]. This concept is displayed in Figure 2.2. In the optical domain, this is equivalent to referencing each adjacent comb line pair within a comb to the line from the other comb nearest the midpoint of the pair. For example, when retrieving Comb A in Figure 2.1, both the pair of $\nu_{15}^{(A)}$ and $\nu_{16}^{(A)}$ and the pair of $\nu_{18}^{(A)}$ and $\nu_{19}^{(A)}$ share $\nu_{3}^{(B)}$ as the common line to be cancelled, but the midpoint of $\nu_{19}^{(A)}$ and $\nu_{20}^{(A)}$ is closer to $\nu_{4}^{(B)}$ and so the reference point is changed. For Comb B, $\nu_{19}^{(A)}$ is the closest line to the midpoint of $\nu_{3}^{(B)}$ and $\nu_{4}^{(B)}$ and is thus used as the common point of reference. While any comb line from the second comb can theoretically be chosen as the common reference for the retrieved pair, choosing the one closest to the pair's midpoint as done here represents the most efficient scheme, requiring the least amount of RF bandwidth. This minimum bandwidth required for retrieval is governed by the relationship in Equation (2.4).

$$BW_{RF} \geq (N_H + 1)\frac{f_{rep}^{(A)}}{2} \qquad (2.4)$$

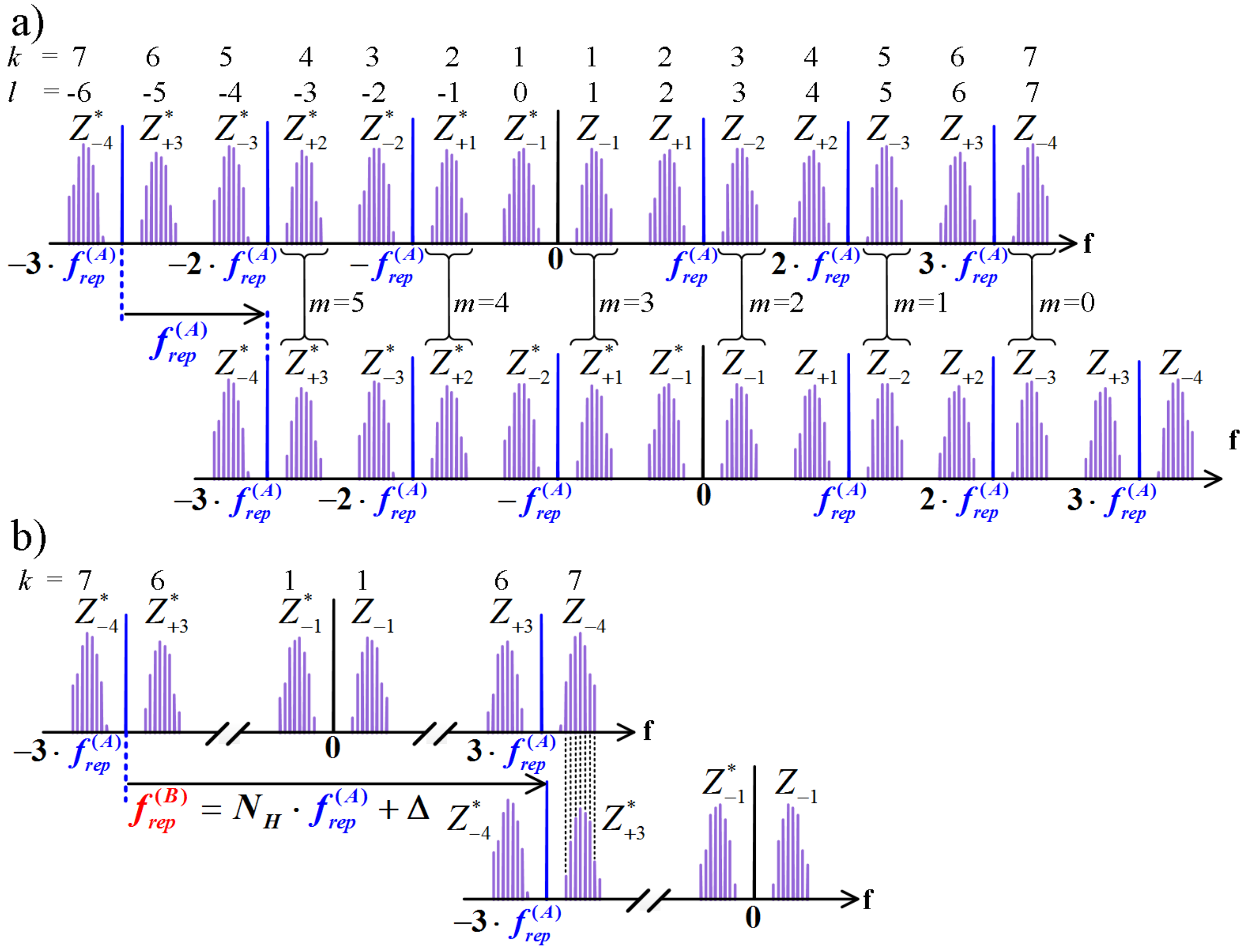

Figure 2.2 Visual representation of retrieval algorithm for a) low repetition rate comb and b) high repetition rate comb. As in Figure 2.1, N_H=6 and N_B=8.

To rigorously establish which beats to compare and in what order for retrieval of Comb A, first notice that if an index value is assigned to each RF beat set starting with l=1 for the Z_{-1} set and continuing in each direction such that l=0 for Z^*_{-1}, l=2 for Z_{+1}, and so on, then the l_1 beat set in the original spectrum is always paired with the l_2=(l_1-2) set in the translated spectrum as seen in Figure 2.2a. Equation (2.5) gives the index values l_1 and l_2 for each of the two beat sets, where m is defined by Equation (2.6) in terms of the optical comb line index n of Comb A which runs from n = 1 to $n = N_H \cdot N_B + 1$ as shown in Figure 2.2. The variable m effectively represents an index value for pairs of beat sets starting with m=0 for the most positive frequency pair and increasing to $m = N_H - 1$ for the most negative frequency pair. The last term in the expression for l_1 accounts for the parity of N_H, ensuring an incorrect mirror image of the spectrum is not recovered for odd values of N_H.

$$l_1 = N_H + 1 - 2m - (N_H \bmod 2); \quad l_2 = (l_1 - 2) \tag{2.5}$$

$$m = (n-1) \bmod N_H \tag{2.6}$$

Computationally, it is more efficient to work with a single-sided RF spectrum, using half the amount of data in the double-sided spectrum, and so the beat set index l is converted to a single-sided spectrum beat set index k using Equation (2.7), where sgn is the signum function.

$$k_{1,2} = \left| l_{1,2} + \tfrac{sgn(l_{1,2})-1}{2} \right| \tag{2.7}$$

While the transparency of the double-sided spectrum indexing is lost since $k_2 \neq (k_1 - 2)$ for negative values of l, retrieval can be performed more quickly by analyzing less spectrum and identifying fewer beat frequencies. The individual beat frequencies to be compared within the k_1 and k_2 beat sets are then given by their indices j_1 and j_2, respectively, in Equation (2.8).

$$j_{1,2} = sgn(l_{1,2}) \cdot \left[\left\lfloor \tfrac{n-1}{N_H} \right\rfloor + 1 - \tfrac{sgn(l_{1,2})-1}{2} \left(N_B - 1 - 2 \left\lfloor \tfrac{n-1}{N_H} \right\rfloor \right) \right] \tag{2.8}$$

It should be noted that negative values of j indicate the complex conjugate of that beat is to be used. Finally, with $k_{1,2}$ and $j_{1,2}$, Equation (2.9) can be applied to recover the magnitude ratio and phase difference of the n and n+1 lines in Comb A [57].

$$\frac{A_n}{A_{n+1}} e^{i(\alpha_{n+1} - \alpha_n)} = \frac{Z_{(-1)^{k_1} \left\lfloor \frac{k_1+1}{2} \right\rfloor}(j_1)}{Z_{(-1)^{k_2} \left\lfloor \frac{k_2+1}{2} \right\rfloor}(j_2)} \tag{2.9}$$

At this point, having retrieved the relationships between adjacent comb lines across the entire spectrum, the magnitude and phase of any one comb line can be arbitrarily chosen and the magnitude and phase of all other comb lines relative to the initial comb line can be calculated easily. The choice of arbitrary initial comb line magnitude translates to a scaling of the retrieved waveform average power, and the arbitrary choice of initial phase creates a constant phase offset across the entire spectrum, equivalent to a shift of the electric field relative to the retrieved waveform envelope in the time domain.

The retrieval algorithm for Comb B illustrated in Figure 2.2b is very similar in principle, but can be greatly simplified as only two beat sets are required for the retrieval. Using the same beat set indexing schemes as before, the two beat sets of interest are identified by Equation (2.10).

$$k_1 = N_H + 1 - (N_H \bmod 2);\;\; k_2 = N_H + (N_H \bmod 2) \qquad (\ 2.10\ )$$

The RF comb line index for the k_1 beat set is simply given by $j_1=n+1$, where n now is the optical comb line index of Comb B running from $n=0$ to $n=N_B-1$, and the RF comb line index for the k_2 set is given by $j_2=N_B+1-n$. Equation (2.11) then describes the proper ratio for recovery of the magnitude and phase relationship of adjacent comb lines in Comb B [57]. Note that the magnitude ratio in Equation (2.11) is the reciprocal as compared to that in Equation (2.9), and that the complex conjugate is always taken of the RF beat in the denominator.

$$\frac{B_n}{B_{n-1}} e^{i(\beta_n - \beta_{n-1})} = \frac{Z_{(-1)^{k_1}\left\lfloor\frac{k_1+1}{2}\right\rfloor}(n+1)}{Z^*_{(-1)^{k_2}\left\lfloor\frac{k_2+1}{2}\right\rfloor}(N_B+1-n)} \qquad (\ 2.11\ )$$

2.2.2 Post-Processing Considerations

While appropriate conditioning of the optical spectra is imperative for producing an RF spectrum suitable for retrieval, proper acquisition and processing of the multi-heterodyne signal is also vital. To obtain the complex RF spectrum, a fast Fourier transform (FFT) is calculated of the multi-heterodyne signal which is digitized by a high speed, real-time oscilloscope. In calculating the FFT, it is desired that the heterodyne beats fall exactly on the points or bins in the FFT vector so as to avoid scalloping losses and to get an accurate measure of the beats' magnitude and phase. Towards this end, the duration of the signal to be transformed is chosen to be an integer multiple of the period corresponding to the effective repetition rate difference of the two comb sources. That is to say, $T_s = a \cdot T_p = b/\Delta$ where T_s is the duration of the signal, T_p is the oscilloscope sampling period, Δ is the effective repetition rate difference, and a and b are integers. Doing so maps the separation between beat frequencies to an integer number of FFT points such that the same segment of the (implicit or explicit) time-domain windowing function's frequency response is consistently sampled.

This exact mapping is not always possible however, as the sampling period of the oscilloscope may not be commensurate with the signal period ($1/\Delta$), in which no integers a and b exist that satisfy $a \cdot T_p = b/\Delta$. In other cases, a and b may exist, but only if T_s is allowed to become very long, at which point one must consider the upper limit on acquisition time imposed by the coherence time of the two comb sources. If the comb sources are phase locked to a common stable reference, it is possible to acquire coherent signals over long times (~1s) and achieve correspondingly high frequency resolution in the Fourier spectrum [15]. In the results shown here, the maximum acquisition time was limited to ~10 μs by the ~100 kHz optical linewidth of the low repetition rate comb. With this time constraint, the constant sampling rate of 25 GS/s dictated by the DAQ card of the oscilloscope, and Δ set by the comb repetition rates, we were unable to identify values of a and b satisfying the above relationship, resulting in a small slippage between beat peaks and FFT bins. As the retrieval algorithm is based on taking the complex ratio of beats which now have different amounts of scalloping loss, this slippage introduces compounding error which ends up dramatically distorting the retrieved spectrum.

To rectify these errors, several options exist, the simplest of which is to choose a smoother time-domain windowing function than the implicit rectangular window to apply to the signal before transforming. A Hann window has been applied to all data shown here to reduce the maximum scalloping loss as well as mitigate the effect of sidelobes on neighboring beats. While windowing helps to improve retrieved magnitude accuracy, the error due to beats not being separated by an integer number of FFT bins must still be corrected. A beat's true magnitude may be estimated by increasing the frequency resolution through transformation of longer duration signals, but again the issue of signal coherence time is encountered. Alternatively, the length of windowed signal can be held constant while zero-padding to achieve arbitrarily fine interpolation of the frequency spectrum, but this becomes too computationally intensive for long lengths.

The approach taken here was to hold the length of windowed signal constant (i.e. fixed frequency resolution) but incrementally zero-pad the vector to compute multiple FFTs of marginally different lengths, effectively sweeping the FFT points across the multi-heterodyne spectrum [57]. The frequency, magnitude, and phase of all relevant beats were tracked for 22 FFTs of different lengths and aggregated to provide a more accurate picture of the RF spectrum with improved sampling density. The results of this process are shown in Figure 2.3 along with a sample FFT. As one can see, a single FFT fails to accurately capture the true magnitude of all beats simultaneously. Even between two adjacent beats, as displayed in the inset, there is significant slippage of the FFT bins relative to the beat peaks due to a non-integer number of signal periods being transformed. By fitting the beat peaks to the frequency response of the windowing function, an accurate measure of the beat's magnitude and center frequency can be obtained. The center frequency is then used in a linear fit of the phase values to calculate the beat's true phase.

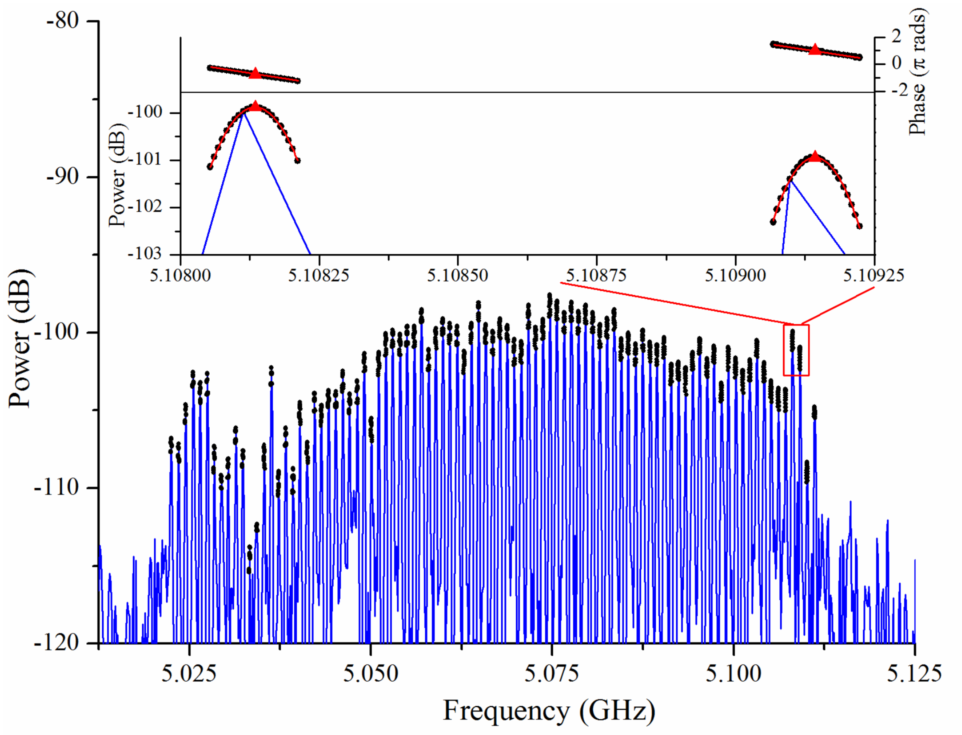

Figure 2.3 Sample heterodyne beat set from multi-heterodyne spectrum. A single FFT is shown in blue and the peak locations from 22 FFTs are shown as black dots. Inset: Detail of two adjacent beats. Fits to magnitude and phase plotted in red, with beat center indicated by red triangle.

In addition to the accurate magnitude and phase measurements, one benefit of this multiple aggregated FFTs approach is the improved processing time. Using 22 different short FFTs (~10^5 samples) is an order of magnitude faster than a single long FFT (~10^7 samples) that achieves the same effective point density seen in the inset in Figure 2.3. If the low repetition rate reference comb is disregarded and only the signal comb retrieved, the total computation time is less than 10 seconds. In contrast, using a single long FFT to perform retrieval takes several minutes. With processing time of seconds, this algorithm enables high accuracy, near real-time complex spectral measurements.

2.2.3 RF Bandwidth Reduction via Subharmonic Multi-heterodyne

The benefit of decreasing $f_{rep}^{(A)}$ from nearly matched (N_H =1) to a small subharmonic (N_H >>1) of $f_{rep}^{(B)}$ is realized as a reduction in the RF bandwidth required to perform spectral retrieval. To demonstrate this, the maximum sampled optical bandwidth as defined by Equation (2.3) and the minimum required RF bandwidth defined by Equation (2.4) are plotted in Figure 2.4 as functions of the effective repetition rate difference, Δ. The difference is normalized to units of $f_{rep}^{(B)}$, which is held constant while $f_{rep}^{(A)}$ is decreased to effect a change in N_H and Δ. In Figure 2.4a and Figure 2.4b, respectively, it can be seen that both the optical bandwidth and the RF bandwidth decrease with larger Δ, and both curves shift downward for increases in N_H. However, the region of large N_H and small Δ can be exploited to achieve sampling of very large optical bandwidths using as little as $f_{rep}^{(B)}/2$ of RF bandwidth. Ultimately, the maximum optical bandwidth that can be sampled is determined by the minimum possible Δ which is in turn limited to the linewidth of the RF beats to avoid overlap. It should be noted that there exist digital post-processing techniques to reduce the RF beat linewidth through phase estimation and frequency drift correction, which allow for reduction of Δ and an increase in optical bandwidth [19, 58].

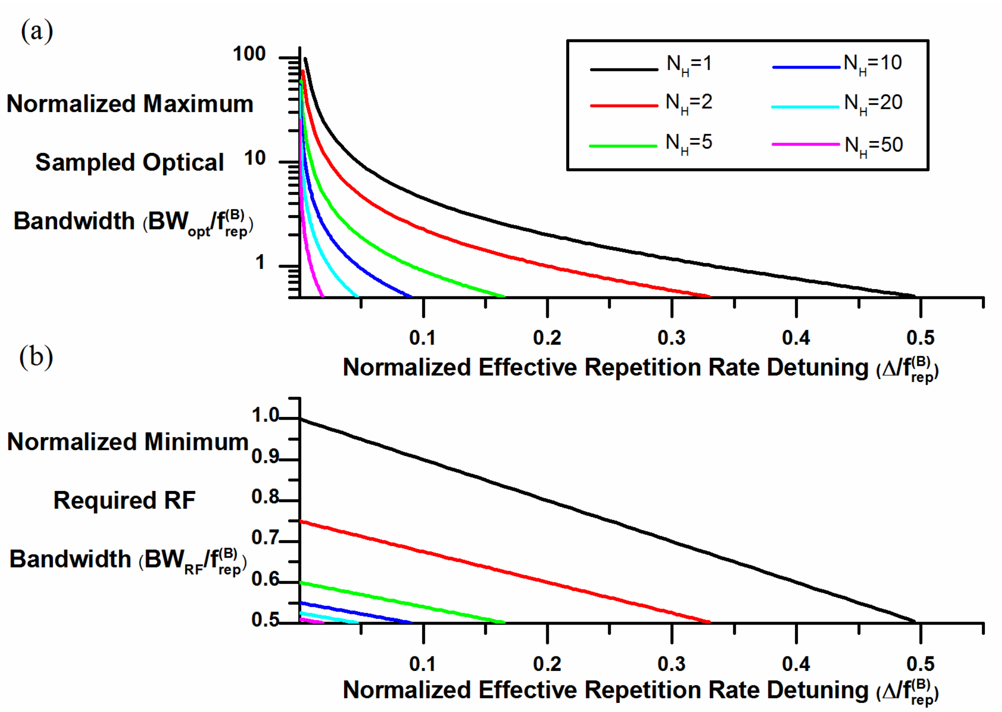

Figure 2.4 Optical and RF bandwidth dependence on repetition rate difference. The high repetition rate, $f_{rep}^{(B)}$, is held constant while the low repetition rate, $f_{rep}^{(A)}$, is reduced from ~$f_{rep}^{(B)}$ to ~$f_{rep}^{(B)}/50$.

One potential drawback of such a drastic difference in repetition rates is the increased power in the fundamental $f_{rep}^{(A)}$ RF tone and its harmonics relative to an individual inter-comb heterodyne beat. For every inter-comb beat, there are N_H in-phase intra-comb beats constructively contributing to the $f_{rep}^{(A)}$ tone, resulting in it dominating the photodetected spectrum and the inter-comb products being lost due to insufficient dynamic range. Equivalently, this can be interpreted in the time domain as the low repetition rate comb producing near transform-limited pulses with high peak power relative to inter-comb beat signals. To mitigate this effect, the low repetition rate pulse train can be strongly dispersed prior to mixing to effectively stretch the pulses to durations longer than the pulse period, creating a quasi-CW waveform and reducing power in the fundamental frequency. Such sampling of arbitrarily shaped pulses with continuous waveforms would not be possible without the above presented self-referenced retrieval algorithm.

2.3 Accuracy Verification

To verify the correctness of the retrieval algorithm and demonstrate the applicability of the measurement technique to high repetition rate, arbitrarily shaped pulse trains, we attempted to measure the spectral phase of a widely spaced frequency comb after applying a known phase mask using a commercial spectral processor based on a liquid crystal on silicon spatial light modulator. The frequency comb to be shaped (Comb B) was produced by a harmonically mode-locked semiconductor laser with a tunable repetition rate around 10.25 GHz [59]. The second frequency comb (Comb A) against which to beat Comb B was a commercially available, carrier-envelope offset stabilized, mode-locked fiber laser with 250 MHz repetition rate. For the purposes of this experiment the repetition rate of Comb B was tuned to 10.251 GHz to give $N_H = 41$ and $\Delta \approx 1$MHz, thus requiring an RF bandwidth of just 5.25 GHz as opposed to 10.251 GHz if measured with a second ~10.25 GHz comb ($N_H = 1$) [56]. The experimental setup to record the interferogram between the two combs consisted of passing Comb B through the spectral processor while Comb A was stretched in a chirped fiber Bragg grating (CFBG) to reduce the peak pulse power and improve the dynamic range. A polarization controller was used after the CFBG to best match polarizations and then the combs were mixed and photodetected. This same setup was used to characterize the laser systems of CHAPTER 3: and can be seen in Figure 3.1.

With the spectral processor in the system but prior to applying any amplitude or phase mask, a baseline interferogram was recorded and the spectra shown on the left in Figure 2.5 were retrieved for Comb B. To show the improvement in retrieval accuracy of our algorithm, we have processed the data three different ways: 1) Using a single FFT with a simplistic rectangular windowing function, shown in black, 2) Using a single FFT with a Hann windowing function, shown in red, and 3) Using multiple FFTs as presented in Section 2.2.2 with a Hann window, shown in blue. The retrieved phase for each of these cases is plotted in Figure 2.5a, exhibiting consistent behavior despite the different processing methods. Fitting the blue phase profile to the third order Taylor polynomial of Equation (2.12) yielded a quadratic phase coefficient of Φ_2=4.21 ps^2 and a cubic phase coefficient of Φ_3= -2.05 ps^3.

$$\Phi = \Phi_0 + \Phi_1(\omega-\omega_o) + \frac{\Phi_2}{2!}(\omega-\omega_o)^2 + \frac{\Phi_3}{3!}(\omega-\omega_o)^3 \qquad (\ 2.12\ )$$

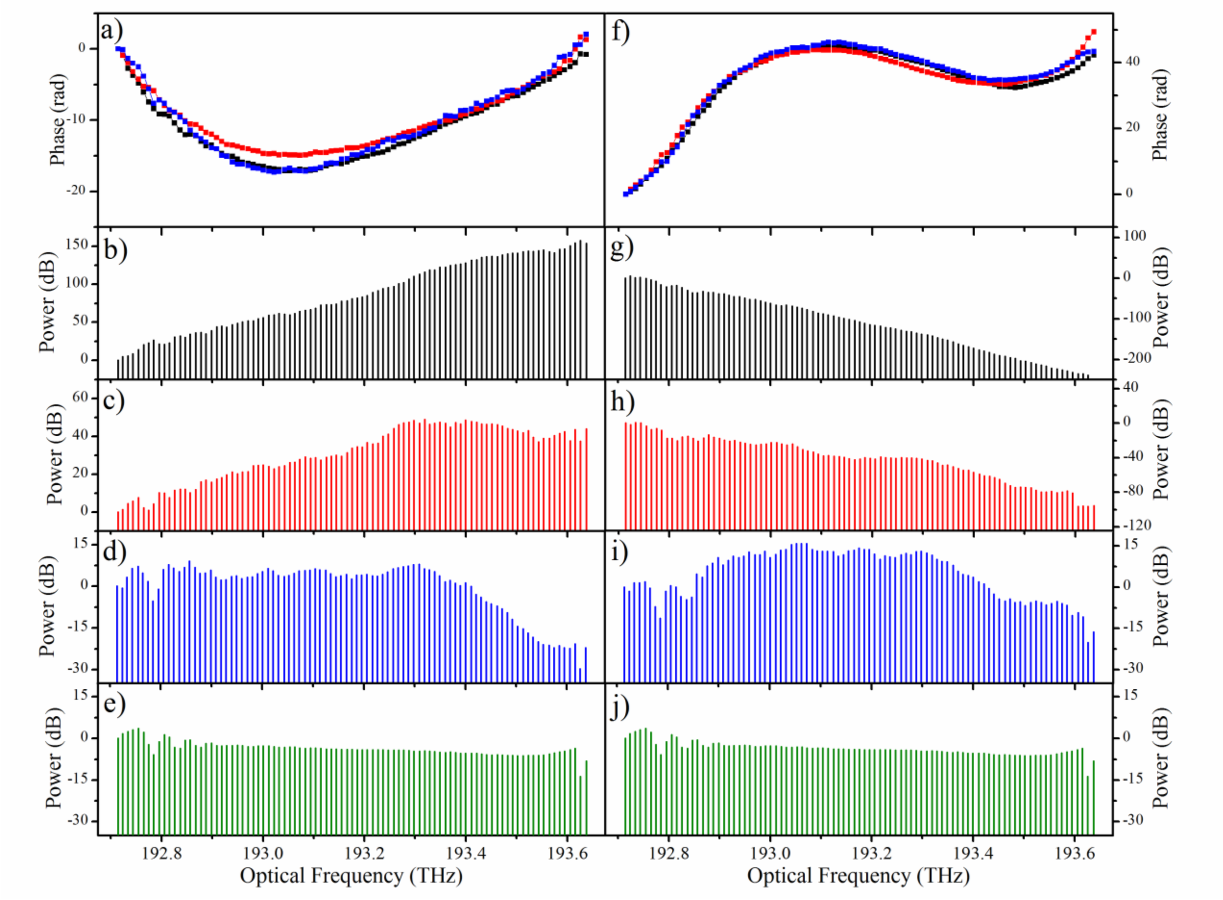

Figure 2.5 Retrieved spectral phase (a, f) and magnitude (b-d, g-i) of high repetition rate comb with comparison of different post-processing methods. The spectrum as measured on an optical spectrum analyzer is shown in (e, j) for reference. The left column of data was taken with no phase mask applied to spectral processor, while a positive cubic phase mask was applied for the data on the right. Second row (black) indicates retrieved spectra with rectangular window. Third row (red) indicates retrieved spectra with Hann window. Fourth row (blue) indicates retrieved spectra with Hann window and multiple aggregated FFTs. Note the independent vertical scales for each plot, though (d, e, i, j) are plotted on the same scale.

In contrast to the phase, the retrieved magnitude varies greatly depending on processing method, with largely different shapes and ranges of power. This can be explained by considering the frequency response of the windowing functions. As seen in Figure 2.3 inset, if the frequency response is sampled at some offset from peak center, the phase is shifted by some small linear amount while the magnitude rapidly drops nonlinearly. Comparing to the spectrum measured on an optical spectrum analyzer and shown in Figure 2.5e, using a rectangular window causes enormous distortion of the spectrum (Figure 2.5b) with a range in excess of 150 dB. Using a Hann window helps to flatten the spectrum (Figure 2.5c), but still produces significant distortion and erroneously predicts increasing power with optical frequency. Aggregating multiple FFTs to predict the true magnitude and phase of RF beats offers clear improvement, with the retrieved spectrum exhibiting the same scale, similar flatness, and distinct features as the measured reference (Figure 2.5d). There is a drop in power at high frequency though, resulting from errors in the calculated magnitude ratio of the beats from those comb lines.

These errors are thought to be due to two factors in this experiment. First, even with adjustment of the polarization controller, Comb A was observed to lack a uniform state of polarization after the CFBG, causing distortions in the photodetected power spectrum as not all comb lines were co-polarized with Comb B. This effect would directly create errors in the retrieved magnitude though not the retrieved phase. In future work, inclusion of a polarizing element after the CFBG to force a uniform state of polarization is expected to mitigate this error. Secondly, the relatively broad optical linewidth of Comb A (~100 kHz) introduces noise in both the magnitude and phase of the RF beats when beating with Comb B. A comb with narrower linewidth will reduce this source of error as well as increase the maximum acquisition time, and magnitude retrieval should be possible. Ultimately however, this issue is not of great concern since the retrieved spectral intensity can be discarded in favor of the easily measured spectrum, similar to what is done in other spectral phase measurement techniques such as Frequency Resolved Optical Gating (FROG) [60].

The spectral processor was then used to apply a purely cubic phase mask with Φ_3=12.09 ps^3 to the output of Comb B. A second interferogram was recorded with the phase mask applied, yielding the spectra in the right column of Figure 2.5 upon retrieval. The retrieved phase in Figure 2.5f is again consistent regardless of processing method, with fit coefficients of Φ_2=4.21 ps^2 and Φ_3=10.05 ps^3 for the blue profile. Comparing these coefficients to those obtained without the phase mask applied, the second-order phase coefficient remained constant, as expected in absence of any quadratic phase change from the mask. The change in the third-order phase coefficient of $\Delta\Phi_3$=12.10 ps^3 is in excellent agreement with the applied mask's cubic coefficient with less than 0.1% error. Similar to the first data set, the retrieved magnitude is observed to be extremely distorted with a rectangular window (Figure 2.5g) and marginally improved with a Hann window (Figure 2.5h). The third approach again produces a flattened spectrum (Figure 2.5i), comparable to the measured spectrum (Figure 2.5j) with the same range.

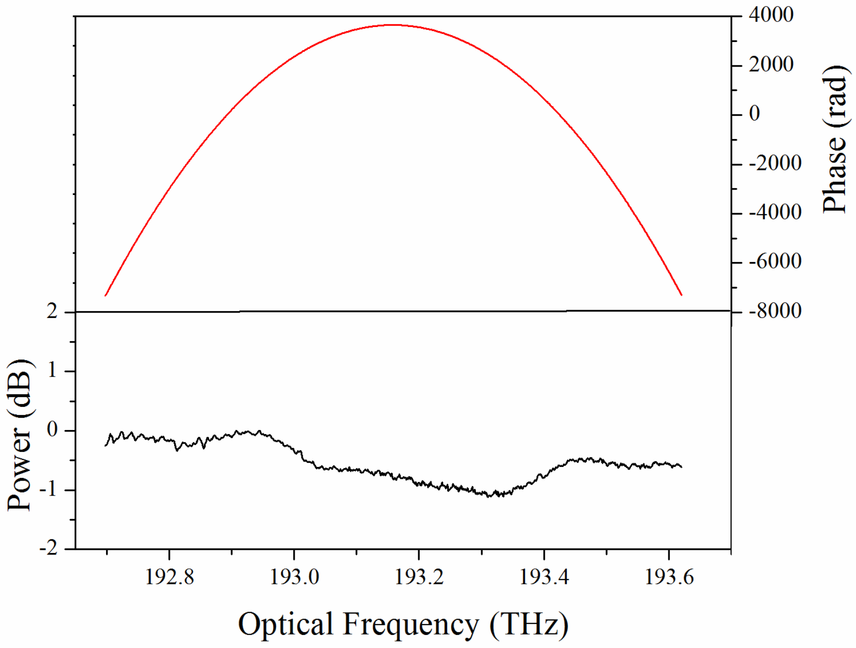

Figure 2.6 Retrieved spectral phase and measured spectral magnitude of 250 MHz frequency comb (Comb A). The spectral phase is primarily shaped by the dispersion of the CFBG.

Using the same interferogram, the spectral phase of Comb A was also retrieved and can be seen in Figure 2.6. Though all fiber and optical components between the comb source itself and the photodetector contribute to shaping the spectral phase, it is expected to be predominantly determined by the highly dispersive CFBG which has a specified dispersion of 2044.64 ps/nm at 1554 nm. The retrieved phase profile is fit with a quadratic phase coefficient of Φ_2=-2616.21 ps^2, equivalent to dispersion of 2042.43 ps/nm at 1554 nm which is just 0.1% less than the specification.

We have demonstrated a rapid, accurate, and self-referenced phase retrieval algorithm based on multi-heterodyne detection. By reducing the repetition rate of one comb source, the required electrical bandwidth can be significantly reduced. In the following chapter, this technique is applied to characterize several different semiconductor mode-locked lasers.

CHAPTER 3: MULTI-HETERODYNE CHARACTERIZATION OF SEMICONDUCTOR COMB SOURCES

In this chapter, the multi-heterodyne measurement technique described in the previous section is used to characterize three different 10 GHz repetition rate semiconductor comb sources. The first source is a harmonically mode-locked laser that is injection locked with a stable CW laser to select one supermode for oscillation. The second source instead uses an intracavity Fabry-Pérot etalon with a free spectral range matching the mode-locking frequency to suppress unwanted supermodes. The third source is similar to the second, but rather than a commercial semiconductor optical amplifier as the gain medium, it uses a prototype device known as a Slab-Coupled Optical Waveguide Amplifier (SCOWA). The third source also contains dispersion compensating fiber to flatten the net cavity dispersion profile and broaden the optical spectrum. By measuring the spectral phase of each of these sources, we can better understand how different cavity elements contribute to the net dispersion and compensate for them to further increase the lasing bandwidth.

3.1 Experimental Setup

To perform each of the following experiments, the setup shown in Figure 3.1 was used. As in Section 2.3, a commercially available, carrier-envelope offset stabilized, mode-locked fiber laser with ~250 MHz repetition rate (OFC A) was mixed with the ~10.25 GHz semiconductor lasers under test (OFC B). These repetition rates represented a subharmonic order of 41, thus reducing the required RF bandwidth from ~10.25 GHz to ~5.25 GHz (See Equation (2.4)). This reduction in bandwidth was critical, enabling the multi-heterodyne interferogram to be recorded with an 8 GHz bandwidth real-time oscilloscope. The complex RF spectrum was obtained by computing a Fourier transform.

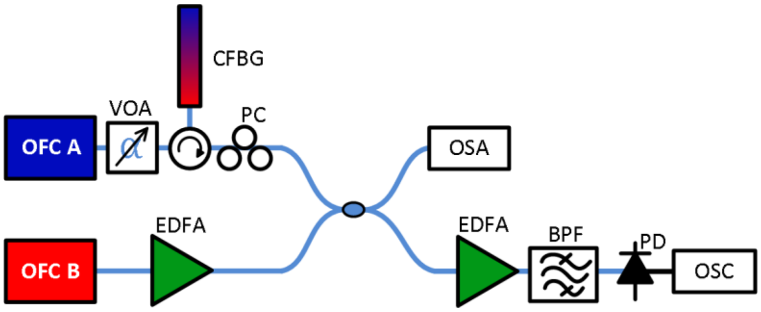

Figure 3.1 Experimental setup. OFC, Optical Frequency Comb; VOA, Variable Optical Attenuator; CFBG, Chirped Fiber Bragg Grating; PC, Polarization Controller; EDFA, Erbium-Doped Fiber Amplifier; BPF, Band Pass Filter; PD, Photodetector; OSC, Real-time Oscilloscope; OSA, Optical Spectrum Analyzer.

Oscilloscope traces lasting 20 µs were saved for off-line post-processing, though only ~8 µs segments were used for calculation of the Fourier spectrum. This time duration was chosen to be equal to N/Δ, where N is an integer satisfying $N/\Delta < 1/LW_A$. LW_A is the optical linewidth of one comb line from OFC A, measured to be ~100 kHz by a heterodyne measurement with a narrow linewidth CW laser. As this linewidth is much broader than that of any of the 10.25 GHz test lasers, the maximum record length was effectively set by Comb A's coherence time to ~10 µs. Thus, record lengths were chosen to be as long as possible to improve the signal-to-noise ratio, but less than the coherence time such that the entire signal was still coherent. Though not done here, phase noise compensation can be performed to increase record lengths and thus improve the signal-to-noise ratio [61].

One downside of such a drastic difference in repetition rates is the increased power in the 250 MHz RF tone and its harmonics relative to an individual inter-comb heterodyne beat. For every inter-comb beat, there are 41 in-phase intra-comb beats constructively contributing to the 250 MHz tone, resulting in it dominating the photodetected spectrum and the inter-comb products being lost due to insufficient dynamic range. Equivalently, this can be interpreted in the time domain as the 250 MHz comb producing transform-limited pulses with high peak power relative to inter-comb beat signals. To mitigate this effect, a chirped fiber Bragg grating was added to the optical path of the 250 MHz comb to effectively stretch the pulses to durations longer than the pulse period, creating a quasi-CW waveform and reducing power in the 250 MHz harmonics.

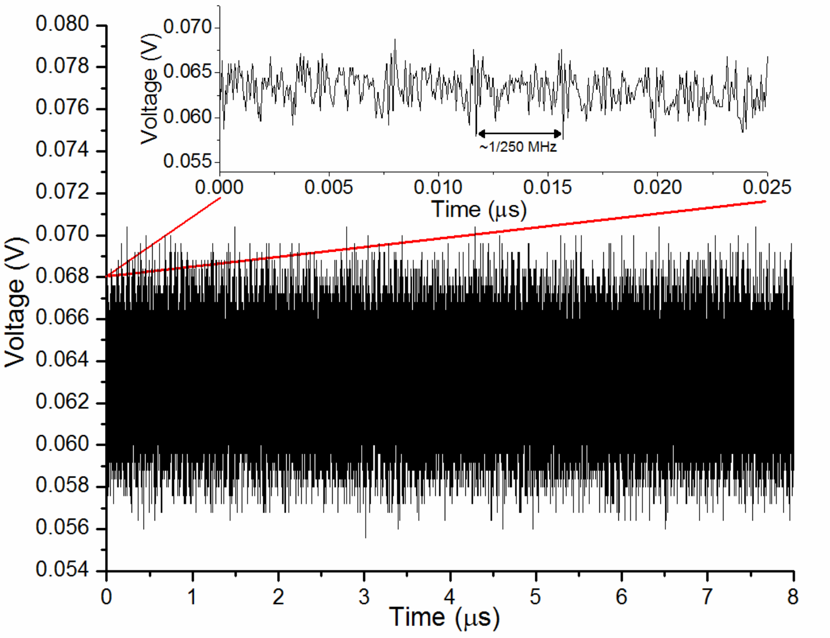

Figure 3.2 Sample oscilloscope trace of multi-heterodyne signal. Inset shows fast time-scale features, with clear periodicity from the 250 MHz comb source.

An example multi-heterodyne beat signal between the stretched 250 MHz comb output and the ~10.25 GHz comb is shown in the oscilloscope trace in Figure 3.2. A large DC background is present due to the quasi-CW pulse train, though some periodicity at 250 MHz can still be observed in the inset. The Fourier spectrum of this signal is shown in Figure 3.3 in which distinct beat sets can be seen. The blue rectangle in Figure 3.3 illustrates the spectrum used to perform retrieval for the 250 MHz comb, while the red rectangle contains the spectrum needed for retrieval of the 10.25 GHz comb. The portion in the red rectangle is expanded in the inset to show beat set structure and individually resolvable comb lines with up to 30 dB SNR. It should be noted that balanced detection can be used to significantly improve the SNR [55], which was not done here due to lack of available detectors.

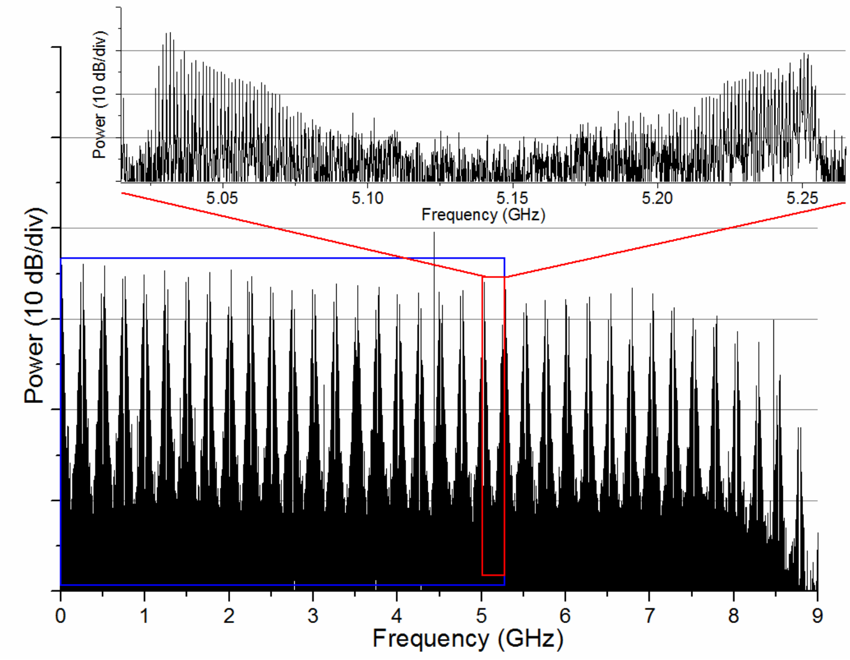

Figure 3.3 Sample multi-heterodyne Fourier spectrum. The blue rectangle highlights the portion of the spectrum required for magnitude and phase retrieval of the 250 MHz comb. The red rectangle, expanded in inset to show beat set structure, indicates the spectral region required for magnitude and phase retrieval of the 10.25 GHz combs.

3.2 Injection Locked Harmonically Mode-Locked Laser

The first laser frequency comb source measured was an injection locked harmonically mode-locked laser such as that of reference [59]. The laser, shown in Figure 3.4, features a commercially available semiconductor optical amplifier (SOA) gain medium coupled into a long fiber cavity (4.26 m) for a cavity fundamental frequency of ~47 MHz. The laser is harmonically mode-locked via an intracavity Mach-Zehnder style intensity modulator at a rate of 10.250984 GHz, resulting in 218 pulses traversing the cavity simultaneously. The harmonically mode-locked spectrum typically consists of multiple groups of axial modes interleaved with an intra-group spacing at the repetition rate.

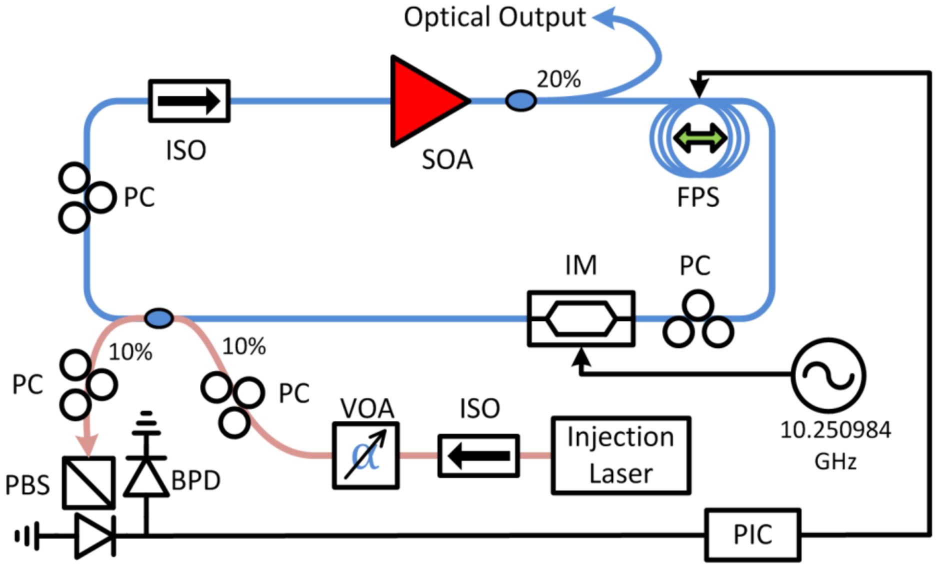

Figure 3.4 Injection locked harmonically mode-locked laser. Slave optical cavity is shown in blue, with the injection arm and stabilization optics shown below it in red. SOA, Semiconductor Optical Amplifier; FPS, Fiber Phase Shifter; PC, Polarization Controller; IM, Intensity Modulator; ISO, Isolator; VOA, Variable Optical Attenuator; PBS, Polarization Beam Splitter; BPD, Balanced Photodetector; PIC, PI Controller.

Generation of a frequency comb in such a spectrum can be achieved by selecting one of these phase correlated axial mode groups to exist. Other techniques, such as those in the following sections, utilize an intracavity etalon with free spectral range equivalent to the mode-locking rate to suppress all other axial mode groups but one. In contrast, this laser uses single frequency injection into one cavity mode to generate the desired widely-spaced frequency comb. The master injection laser is also a commercially available single frequency laser at 1550 nm. When injected into the laser cavity, injection locking of the selected cavity resonance is achieved, resulting in linewidth narrowing and frequency pulling to that of the master laser frequency. Energy is then shared via the mode-locking mechanism with other resonances of the same axial mode-group at spacings of the repetition rate. Due to gain competition, other cavity resonances are suppressed, resulting in a high quality frequency comb.

While the injection laser frequency remains within a ‘locking bandwidth’ around the free-running slave laser resonance frequency, the laser will remain injection locked. Length fluctuations in the long fiber cavity due to environmental factors such as temperature and pressure will interrupt the injection locked state, resulting in an unreliable source of optical frequency combs. Therefore, a scheme is necessary to detect these changes in cavity resonance frequency and feed back into the cavity to maintain the injection locked state with high quality comb output. To achieve this, a polarization spectroscopy technique first conceived by Hänsch and Couillaud [62] is utilized wherein orthogonal polarizations are interrogated in a polarization selective cavity. The scheme is shown in the bottom of Figure 3.4. At the desired injection locking frequency, one polarization is resonant while the orthogonal polarization is directly reflected, providing a convenient phase reference. At reflection, the two beams are projected onto one another again in a balanced photodetection scheme providing a voltage error signal, which is fed into a proportional-integrating controller to adjust an intracavity fiber phase shifter and affect the cavity resonance frequency.

The resulting optical spectra from the injection locked frequency comb source are shown in Figure 3.5a and a high resolution spectrum is shown in Figure 3.5b. When no injection signal is present, the harmonically mode-locked spectrum appears continuous, due to the simultaneous lasing of the tightly spaced (47 MHz) laser cavity modes, below the resolution of both measurement devices. Injection locked spectra, shown in blue, show a high contrast 10.251 GHz spaced optical frequency comb with ~32 dB optical SNR, and 7.4 nm of bandwidth for a total of

90 comb lines. Figure 3.5c shows the photodetected RF spectrum of the laser, showing a strong RF tone at the mode-locking rate and large SNR and no RF supermode noise spurs visible above the noise floor over a large offset band. Ideal supermode suppression while maintaining reasonable injection locked bandwidth was achieved with an injection power of 20 µW. A sampling oscilloscope trace can be seen in Figure 3.5d, clearly showing a ~10.25 GHz pulse train.

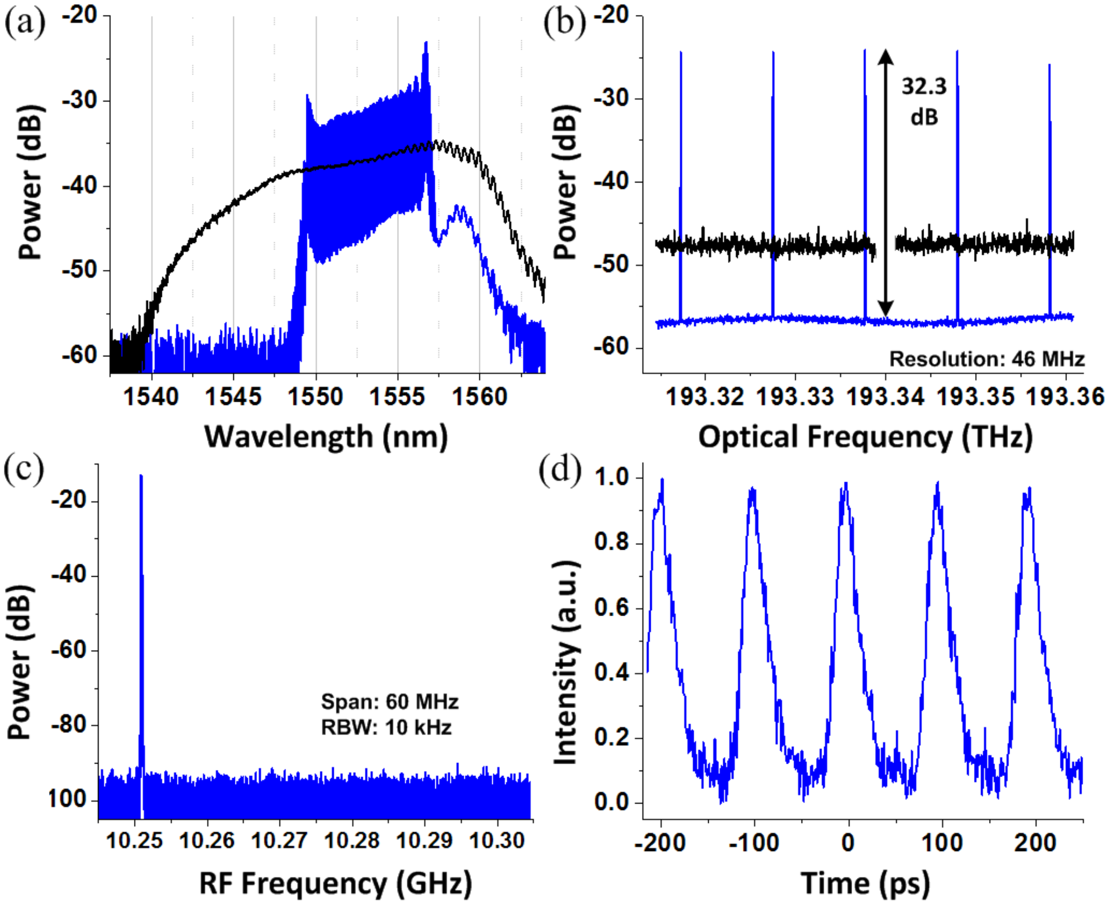

Figure 3.5 a) Output optical spectra and b) high-resolution optical spectra of a harmonically mode-locked laser system with (blue) and without (black) injection locking. c) RF spectrum of photodetected injection locked comb source optical output. d) Sampling oscilloscope trace of photodetected pulse train.

An exceptional feature of this method of frequency comb generation is its versatility. The frequency comb spacing is determined by the mode-locking rate, which can be set to any multiple of the cavity fundamental frequency and finely tuned in a smaller bandwidth as well. In addition, the absolute position of the comb can easily be shifted by adjusting the frequency of the optical injection signal. Therefore, the injection locked laser comb source is an ideal source for use in multi-heterodyne experiments with less versatile frequency comb sources since it effectively enables precise positioning of the entire RF spectrum via δ_o, Δ, and N_H.

In Figure 3.6, the measured spectral intensity and the retrieved spectral phase can be seen, along with a fit of Equation (2.12) to the spectral phase shown in black. From the fit parameters of the quadratic phase and cubic phase, we gain knowledge of the temporal pulse characteristics. The quadratic phase gives an estimate of the linear chirp or pulse broadening as compared to a perfectly transform limited pulse, while the third order phase coefficient provides a measure of the pulse asymmetry. The polynomial fit yields values of 5.23 ps^2 and -1.59 ps^3 for the quadratic and cubic phase coefficients, respectively. From the quadratic phase coefficient, it is determined that the comb source produces down-chirped pulses with linear dispersion of 4.08 ps/nm at 1555 nm. The small, negative value of the third-order dispersion indicates the pulses are slightly asymmetric with temporal broadening on the trailing edge.

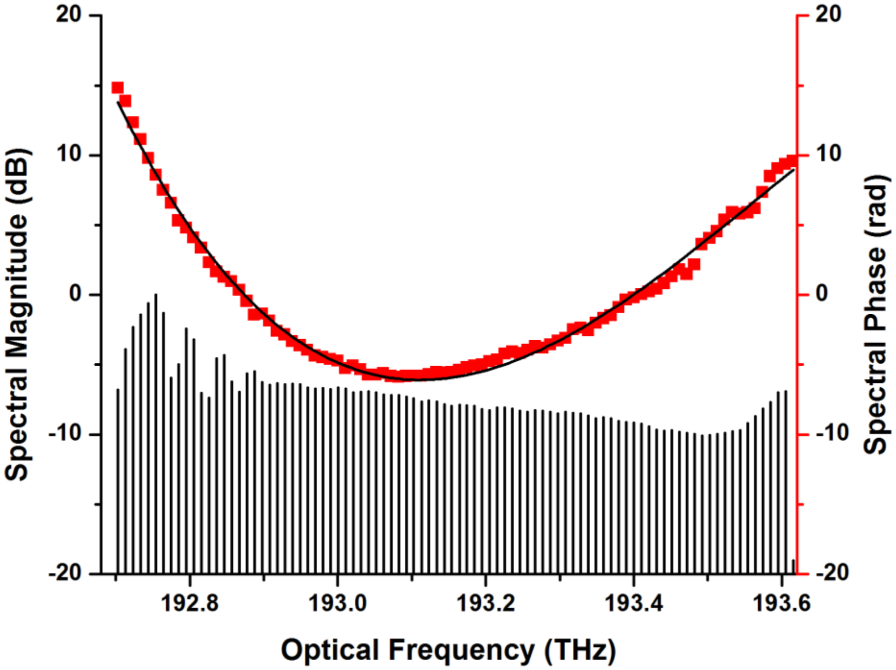

Figure 3.6 Measured spectral magnitude and retrieved phase of injection locked harmonically mode-locked laser.

In Figure 3.7a, the time domain waveform as calculated from the measured spectrum and retrieved spectral phase of Figure 3.6 is plotted. As predicted, the pulse has a sharp peak followed by a long tail at later times. Interestingly, there is a rapid modulation on top of the pulse with a period equal to the inverse of the spectral bandwidth. This is likely due to the sharp edges of the spectrum, as seen in Figure 3.5a and Figure 3.6. A comparison of the autocorrelation calculated from the pulse in Figure 3.7a and an experimentally measured autocorrelation is made in Figure 3.7b. Although the autocorrelation is an ambiguous measurement, the good agreement between the calculated and measured data suggests accurate retrieval from the multi-heterodyne signal. It should be noted that the waveform and autocorrelation are calculated from the retrieved data, not the polynomial fit which is used solely to quantify the dispersion.

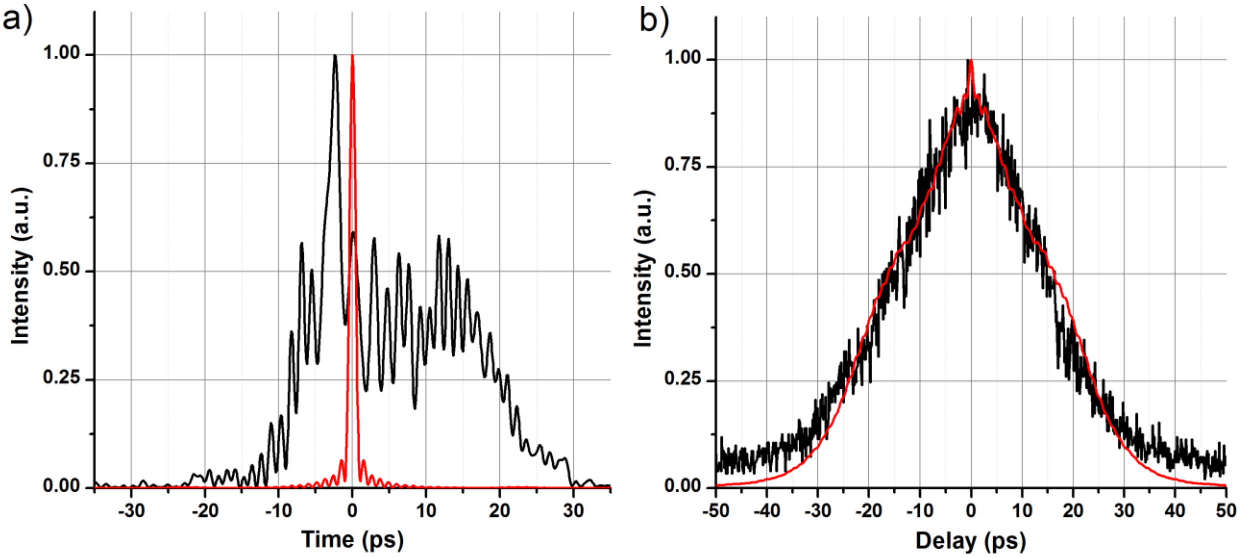

Figure 3.7 a) Calculated pulse intensity profile (black) and transform-limited profile (red). b) Comparison of calculated autocorrelation (red) and measured autocorrelation (black).

3.3 Coupled Cavity Harmonically Mode-Locked Laser

Low noise semiconductor-based harmonically mode-locked lasers have also been shown to produce a stable frequency comb using a cavity design that uses a long optical fiber cavity (~28 m) coupled to a nested Fabry-Pérot etalon (FPE) [14, 63]. In this architecture, narrow linewidth of the individual comb-lines can be achieved due to the long storage time of the fiber cavity, which increases the cavity's frequency selectivity, and the wide mode spacing is imposed by the spacing of the transmission peaks of the transfer function of the FPE. The FPE thus serves the main purpose of selecting an axial mode group out of the N possible ones from N^{th}-order harmonic mode-locking, as explained previously. In the time domain, the FPE can be understood as a storage element that correlates a pulse with N other pulses, up to the decay time of the field in the cavity. If the fiber cavity length is chosen to be such that only one mode falls within the -3 dB bandwidth of the each of the etalon's transmission peaks (or, in the time domain, the fiber cavity is short enough that a pulse comes back to the etalon before its effects have decayed or become negligible), then a single pulse-train of nominally identical pulses with a well-defined (albeit sometimes unknown) carrier-envelope phase slip is generated and, in the frequency domain, this corresponds to a frequency comb.

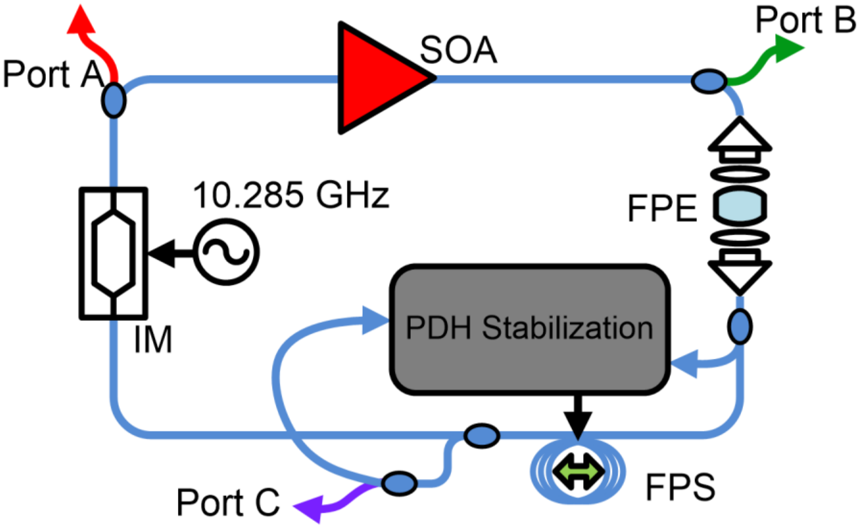

Figure 3.8 Coupled cavity harmonically mode-locked semiconductor laser. SOA, Semiconductor Optical Amplifier; FPE, Fabry-Pérot etalon; FPS, Fiber Phase Shifter; PDH Stabilization, Pound-Drever-Hall Stabilization electronics; IM, Intensity modulator.

The mode-locked laser experimental setup is shown in Figure 3.8. A commercially available SOA is used for the experiments in this section and an optical cavity comprised of standard single mode fiber (SMF) is built around an FPE with a finesse of 10^3. The laser is mode-locked at 10.285324 GHz via loss modulation using an intracavity $LiNbO_3$ Mach-Zehnder electro-optic modulator. This modulator is driven by a radio frequency synthesizer whose frequency is matched to the Free Spectral Range (FSR) of the FPE. Environmental drift makes it necessary to lock the fiber cavity to the FPE. This is achieved using a multi-comb-line Pound-Drever-Hall

(PDH) scheme, indicated by the shaded box in Figure 3.8, which will be explained further in Section 4.1.1.

In order to analyze the evolution of the mode-locked laser pulses and spectrum around the cavity, we have built a cavity that has multiple output couplers (ports labeled A, B and C) at different points, as shown in Figure 3.8. In particular, we are interested in looking at spectral distortions that occur as the pulses go through the gain medium and the intensity modulator. Additionally, the filtering effect of the FPE can be observed by comparing ports B and C.

Figure 3.9 shows a summary of the results for the retrieved spectral phase of the optical pulse at the three different ports as it propagates around the cavity. The salient features are somewhat similar to that obtained with the frequency comb source stabilized with injection locking techniques in that the pulse in this case is also temporally broadened with linear down-chirp. However, the chirp is much larger than in the injection locked case with an average quadratic phase of 16.18 ps^2 and a maximum of 17.12 ps^2 immediately after the SOA. This is equivalent to a dispersion of 16.18 ps/nm at 1555 nm.

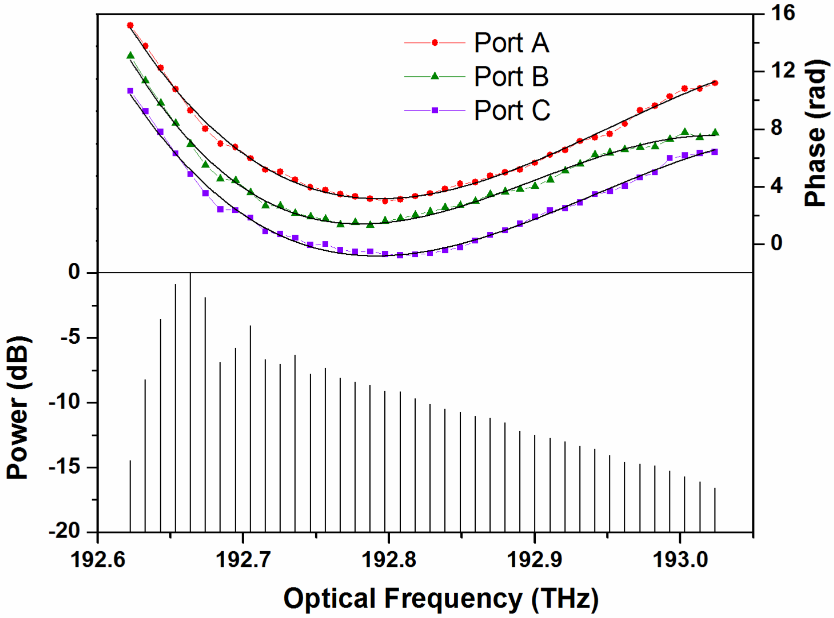

Figure 3.9 Measured spectral magnitude and retrieved phase. Solid black lines in phase plot indicate cubic polynomial fits.

Exact values for the quadratic and cubic phase can be found in Table 1. The relatively large cubic spectral phase suggests significant pulse asymmetry. More importantly, the cubic phase is nearly an order of magnitude larger than the injection locked comb source, which is noteworthy given the fact that the etalon based frequency comb laser is operating with approximately half the bandwidth of the injection locked comb source. It should also be noted that the third order phase is not affected by passage through the intensity modulator, as evidenced by the spectral phase from Port A being nearly identical to that from Port C. On the other hand, the spectral phase after the SOA gain element (Port B) does show a measurable difference suggesting that pulse shaping mechanisms are primarily dominated by the gain media. It is interesting to note the etalon acts as not just a spectral magnitude filter, but also a spectral phase filter due to the odd symmetry of the phase response across each resonance, reducing the amount of cubic phase from Port B to Port C.

Pulse shapes calculated from the spectral information in Figure 3.9 are shown in Figure 3.10. For comparison, the theoretical transform-limited pulse produced by the spectral magnitude of Figure 3.9 is also shown. In each case, the pulse consists of a sharp peak followed by a broad lobe with a long trailing edge. As in Figure 3.7a, rapid oscillations are observed atop the pulses, with period corresponding to the inverse of the spectral bandwidth. Due to the spectrum having smoother edges compared to that in Figure 3.6, these oscillations are not as pronounced as those in Figure 3.7a. The calculated autocorrelations produced by these waveforms match well with the experimentally measured autocorrelations at each output port of the laser cavity.

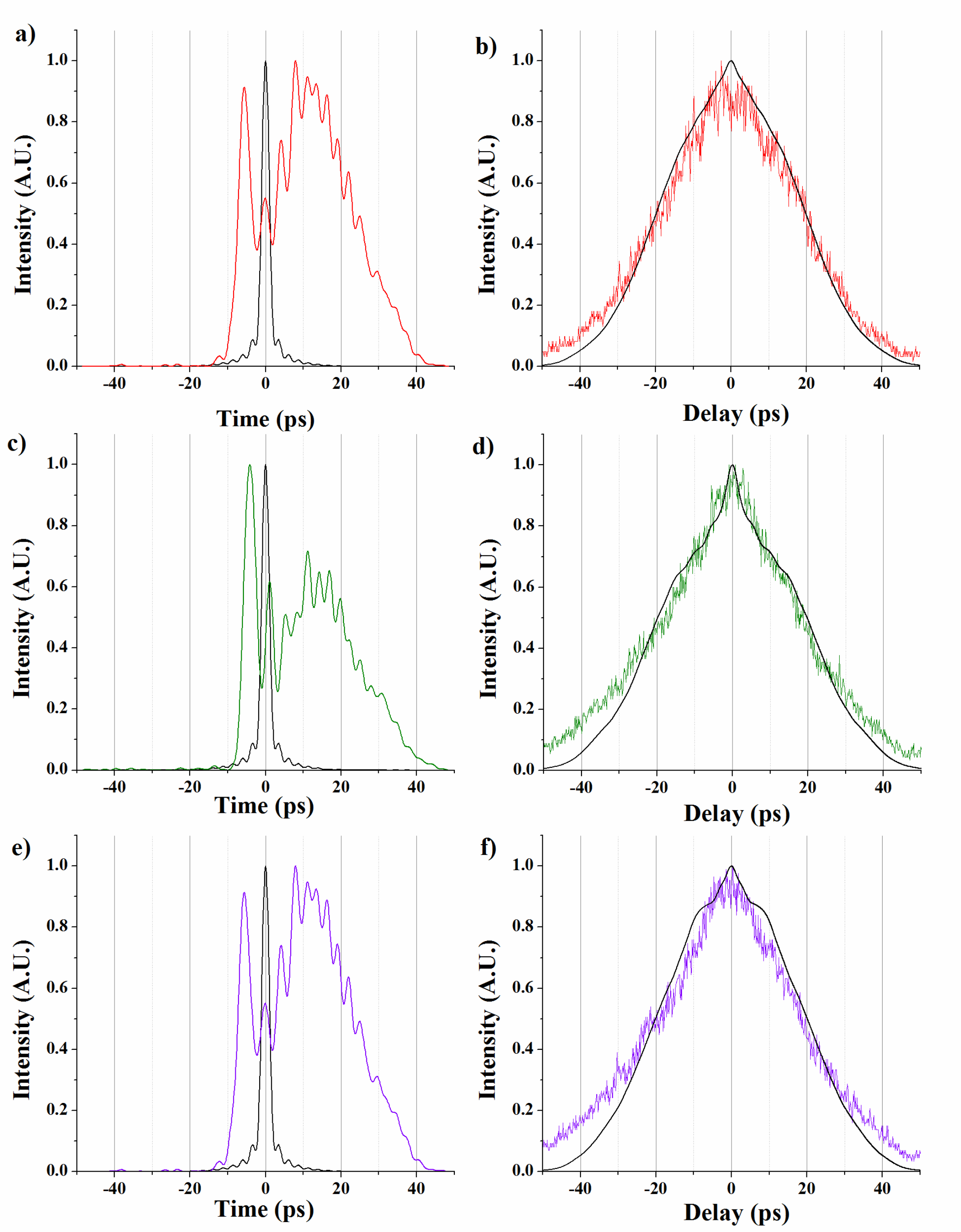

Figure 3.10 Retrieved pulse and autocorrelation profiles. Left column contains retrieved pulse intensities (color) and theoretical transform-limited pulses (black). Right column contains measured autocorrelation (color) and retrieved autocorrelation (black). Colors match ports indicated in Figure 3.8.

3.4 Coupled Cavity Laser with Slab-Coupled Optical Waveguide Amplifier

A laser system similar to the one in the previous section was built separately, using a Slab-Coupled Optical Waveguide Amplifier as the gain medium. SCOWAs have a reduced confinement factor, significantly reducing beam intensity in the active region and thus reducing nonlinearity [64, 65]. This characteristic allows SCOWAs to achieve higher saturation power than standard waveguide SOAs with the trade-off that the gain per unit length is lower. The reduced confinement factor also has the consequence that spontaneous emission is not efficiently coupled to the laser mode. In short, SCOWA devices have shown excellent performance with respect to saturation power, have a low noise figure and have been used in ultra-low noise mode-locked lasers and frequency combs [64, 65].

In this cavity (see Figure 3.11), we have inserted a short section of dispersion compensating fiber (DCF) in order to increase the mode-locked bandwidth. This allows for the generation of a considerably broader mode-locked spectrum. The output pulses have been shown to be compressible to near the Fourier transform limit [32]. The FPE used in this laser has also a finesse of ~1,000, but its FSR is 10.287 GHz (detuned by ~2 MHz from the FPE in Section 3.3).

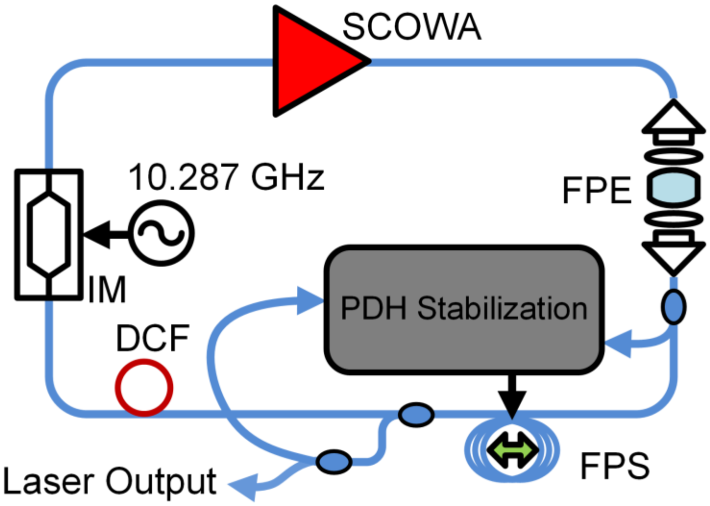

Figure 3.11 Dispersion compensated coupled cavity harmonically MLL with SCOWA gain.

For the experiments presented here, we are aiming to extract fundamental information about the pulse shaping properties as the mode-locked frequency comb is passed through a second external SCOWA. The two initial conditions of importance to measure are the input comb with compressed pulses and with stretched pulses. To provide a clear understanding, 5 key spectra are measured: 1) direct laser output, 2) compressed output, 3) amplified output, 4) amplified and then compressed, and 5) compressed and then amplified. Cases 4 & 5 will shed insight into the role of nonlinear processes in the amplification of the mode-locked comb, since nonlinearities manifest themselves in reciprocal experiments resulting in non-reciprocal results. Results from amplification of short and long pulses are presented in Figure 3.12.

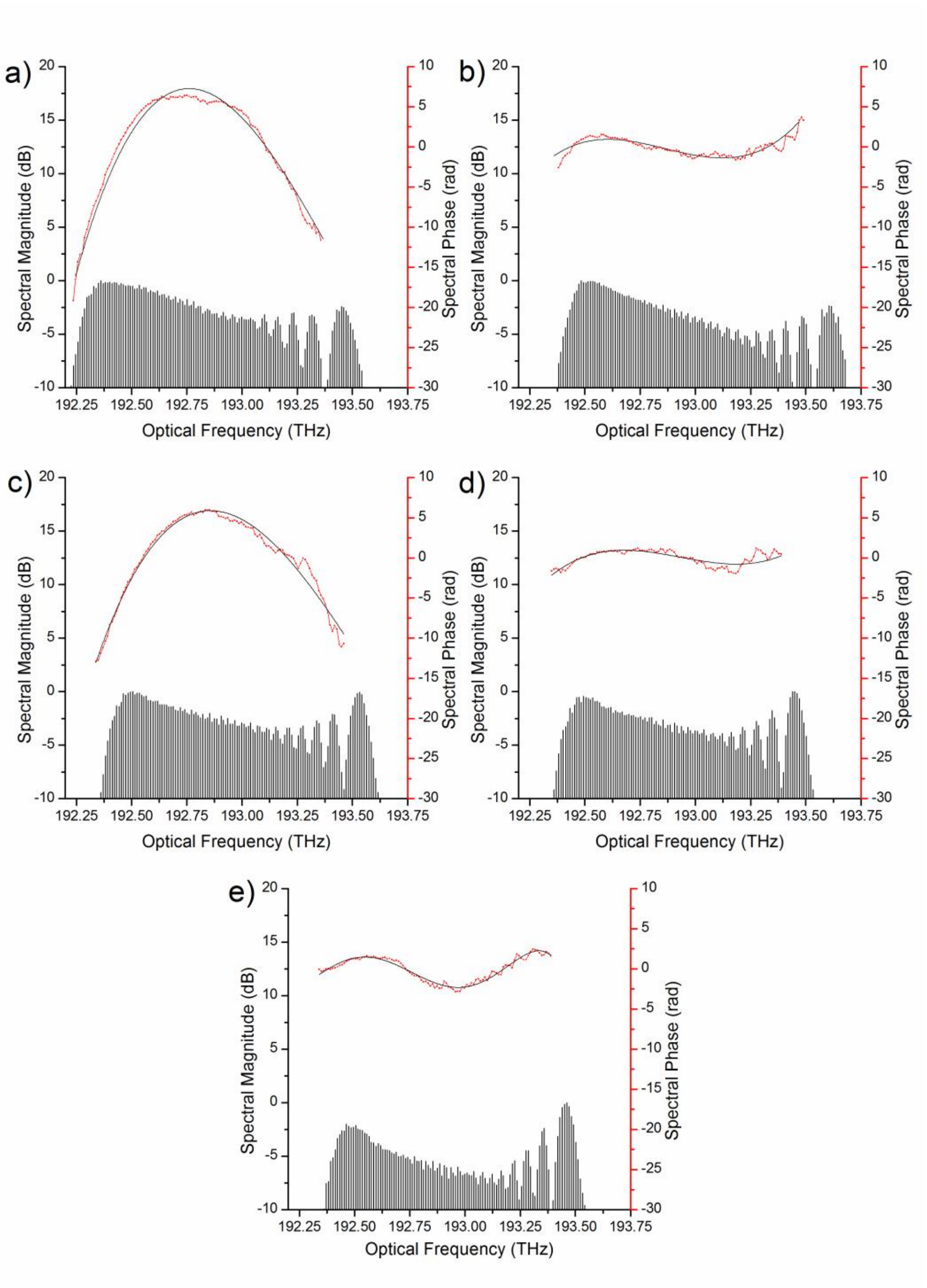

Figure 3.12 Spectra with retrieved phase for a) directly from the laser, b) compression with SMF, c) external SCOW amplification, d) amplification then compression, and e) compression then amplification.

In each of the spectra shown in Figure 3.12, one will notice a distinct ‘lobe’ at the high frequency end of the spectrum over which the phase is not retrieved. Due to a low signal-to-noise ratio in the Fourier spectrum of the photodetected multi-heterodyne signal, the large dip in the spectrum preceding the lobe falls below the measurement noise floor, effectively isolating the lobe from the rest of the spectrum. Though theoretically possible, current implementation of the phase retrieval algorithm is incapable of handling such spectral holes. Accurate prediction of the expected intensity or autocorrelation shapes for these measurements is thus precluded, as there is significant power contained in this lobe over which the phase is not retrieved.

Figure 3.12a shows the measured spectral intensity of the stabilized comb pulse train directly from the output of the laser, along with the retrieved spectral phase. It is recognized immediately that the fundamental shape of the retrieved phase is different in that the sign of both quadratic and cubic phase is opposite of that of the previous two comb sources. Hence, the pulses from this dispersion compensated cavity are up-chirped and mildly asymmetric with a longer leading edge. This sign change can be attributed to the inclusion of the normally dispersive DCF. It should also be noted that the magnitude of both second and third order phase is substantially reduced as compared to the other sources, likely due to both successful dispersion balancing with the DCF and less nonlinearity in the gain from a lower mode confinement factor in the SCOWA. Numerical values for the quadratic and cubic phase from all measurement cases can be found in Table 1.

Compression of the optical pulses was achieved by passing the pulse train through 130 m of SMF to compensate for the quadratic phase. The resulting spectral phase shown in Figure 3.12b suggests that the quadratic component has been significantly reduced, leaving residual third order phase of similar magnitude as that directly from the laser.

The primary feature of interest from the measurement of the spectral phase after external SCOW amplification (Figure 3.12c) is the small, but meaningful reduction in both quadratic and cubic phase. While the quadratic phase reduction can be attributed to extra fiber path length from pigtails, the cubic reduction is likely due to the SCOWA itself. Notice that the SCOWA adds a negative contribution to the cubic phase, similar to the effect of the SOA in the non-dispersion compensated cavity of Section 3.3 between ports A and B, but the magnitude of the contribution is much less, possibly because of the lower mode confinement factor.

In Figure 3.12d, the amplified pulse-train from the previous measurement was passed through the 130 m of SMF. In this case, we observed the quadratic phase to be similar to that from just compression (Figure 3.12b) and the cubic phase to be similar to that from just amplification (Figure 3.12c). This appears to be an effective amplification scheme for obtaining high peak powers, as it results in the lowest overall nonlinear phase and is therefore theoretically the most compressible.

Finally, the pulses were first compressed in the 130 m of SMF and then amplified with the SCOWA. As can be seen in Figure 3.12e, this resulted in a significant distortion of the spectral phase. No longer well-described by a third order polynomial, this phase profile was fit to a fifth order Taylor expansion. The parameters in Table 1 from the fifth order fit indicate a substantial positive increase in the cubic phase. While this value is questionable, the important characteristic of this measurement is the clear, dramatic change in the phase profile, making these pulses difficult to further compress without more advanced techniques.

3.5 Summary

The results from each multi-heterodyne characterization are summarized in Table 1 below. As can be seen from the first two comb sources, in the absence of DCF in the laser cavity, the spectral phase has a positive quadratic component and negative cubic component, leading to the pulses being down-chirped and asymmetric with a long trailing edge. The larger magnitude phase coefficients of the FPE stabilized MLL as compared to the injection locked MLL are likely due to the substantially longer fiber cavity length, increasing the total cavity dispersion. Comparing port A to port B of the FPE stabilized source, it can be seen that the standard waveguide SOA contributes significant negative third order phase to the spectral phase profile. The intracavity FPE is seen to filter and reduce the magnitude of the cubic phase between port B and port C. This effect may be caused by the phase response across an etalon resonance, described by an odd function, acting to balance the cubic phase as laser modes walk off from resonance center.

In contrast to the first two comb sources, the SCOWA based dispersion compensated MLL produces slightly asymmetric up-chirped pulses with a longer leading edge largely due to the negative dispersion and negative dispersion slope of the DCF. The dispersion compensation, along with the low-dispersion gain, results in smaller magnitude phase coefficients than either of the other sources, making the pulses compressible to near Fourier transform limited in 130 m of SMF. Considering the difference between the directly measured output and the externally amplified, the SCOWA is determined to add negative cubic phase, similar to the standard SOA, but an order of magnitude less. The reduction in magnitude is attributed to less nonlinearity in the gain due to a lower confinement factor. Amplification of compressed pulses is shown to increase nonlinearity in the gain and cause distortion of the spectral phase.

In conclusion, we have presented a multi-heterodyne measurement technique for the characterization of spectral phase, independent of reference comb source. We applied this technique to three different semiconductor based optical frequency combs and measured the amount of quadratic and cubic phase in each. The measured phase coefficients were then traced back to effects in the semiconductor gain, fiber cavity, and Fabry-Pérot etalon. With this knowledge, we can hope to more efficiently balance the dispersion of these laser cavities and increase their spectral bandwidth.

Table 1 Summary of Second and Third Order Phase Coefficients

Comb Source	Measurement (Figure)	Φ_2 (ps^2)	D (ps/nm)	Φ_3 (ps^3)
Injection locked MLL	Inj. Lock (Figure 3.6)	5.23	4.08	-1.59
FPE stabilized MLL	Port A (Figure 3.9)	20.52	15.99	-15.13
	Port B (Figure 3.9)	21.96	17.12	-21.32
	Port C (Figure 3.9)	19.80	15.43	-15.57
High power and dispersion compensated FPE stabilized MLL	Direct (Figure 3.12a)	-3.79	-2.95	0.82
	Compressed (Figure 3.12b)	-0.84	-0.65	0.80
	Amplified (Figure 3.12c)	-3.13	-2.44	0.61
	Amp. & Comp. (Figure 3.12d)	-0.42	-0.33	0.64
	Comp. & Amp.* (Figure 3.12e)	-0.17	-0.13	2.83

*The values for the compressed and amplified result are obtained from a fifth-order fit, as opposed to third order fit for all other results.

CHAPTER 4: LOW NOISE, HIGH REPETITION RATE, BROADBAND MODE-LOCKED LASERS

In this chapter, we describe in detail a laser architecture designed to produce broad spectra and stable pulse trains. For the first time, a programmable pulse shaper is added to the laser cavity to optimize dispersion and flatten the gain profile, achieving unprecedented bandwidth from a laser based on this architecture. The laser is then characterized in several different states: a baseline without any spectral shaping, the state corresponding to the lowest noise pulse train, a state with simultaneous low noise and broad bandwidth, and the state corresponding to the broadest spectral bandwidth. Results are also presented for a different configuration of the laser, in which the 10 GHz, 1000 finesse Fabry-Pérot etalon in the cavity is replaced with an 8 GHz, 30000 finesse etalon. This higher finesse etalon allows for longer cavity lengths and hence narrower optical linewidths, but constrains the lasing bandwidth.

4.1 Laser Architecture

A schematic of the laser system is shown in Figure 4.1. The laser cavity is formed by a commercial semiconductor optical amplifier in an external fiber cavity. The semiconductor gain is advantageous as it is directly electrically pumped, enabling high wall plug efficiency, and it features rapid carrier dynamics, making it suitable for low noise operation at multi-GHz repetition rates [66]. The SOA used here is operated with 600 mA current, giving a small signal gain of 28 dB and a saturation power of +14 dBm, as measured at the 1-dB gain compression point. The long fiber cavity is composed of ~40 m of SMF and serves to increase the cavity storage time, effectively decreasing the Schawlow-Townes axial mode linewidth [28]. The long fiber cavity length limits the cavity fundamental frequency to 5 MHz.

To achieve a high repetition rate, an ultralow noise sapphire loaded cavity oscillator at 10.24 GHz is mixed with a 45 MHz oscillator to produce a ~10.285 GHz signal used to drive a $LiNbO_3$ electro-optic intensity modulator and harmonically mode-lock the laser at the ~2057th harmonic of the cavity fundamental frequency. This has the effect of sharing energy and correlating modes spaced by the modulation frequency, leading to the formation of multiple interleaved axial mode groups or supermodes. Little correlation exists between adjacent mode groups, leading to gain competition and ultimately supermode noise which contributes to timing jitter in the output pulse train. Introduction of a Fabry-Pérot etalon with an FSR matching the modulation frequency mitigates the supermode noise by filtering out all but a single mode group for oscillation [31]. In practice, the FSR of the etalon is determined first using a highly sensitive modified Pound-Drever-Hall scheme [67] and the modulation rate is subsequently chosen to match. The FSR of the etalon used here was measured to be 10.285325 GHz and the finesse was 1000, resulting in resonance passbands of ~10 MHz FWHM. This is sufficiently narrow to effectively suppress unwanted mode groups offset from the lasing mode group by multiples of the cavity fundamental frequency of 5 MHz.

A variable optical delay (VOD) line in the cavity enables coarse, long cavity length changes to match the cavity fundamental frequency to a subharmonic of the etalon FSR. Equivalently, the fiber cavity round trip length is adjusted to be an integer multiple of the etalon cavity double pass length. This is accomplished by removing any modulation signal applied to the intensity modulator, monitoring photodetected cavity mode beat frequencies on a RF spectrum analyzer, and changing the VOD until a harmonic of the fundamental frequency is commensurate with the known etalon FSR. Fine tuning and stabilization of the cavity length is achieved using a piezoelectric fiber stretcher.

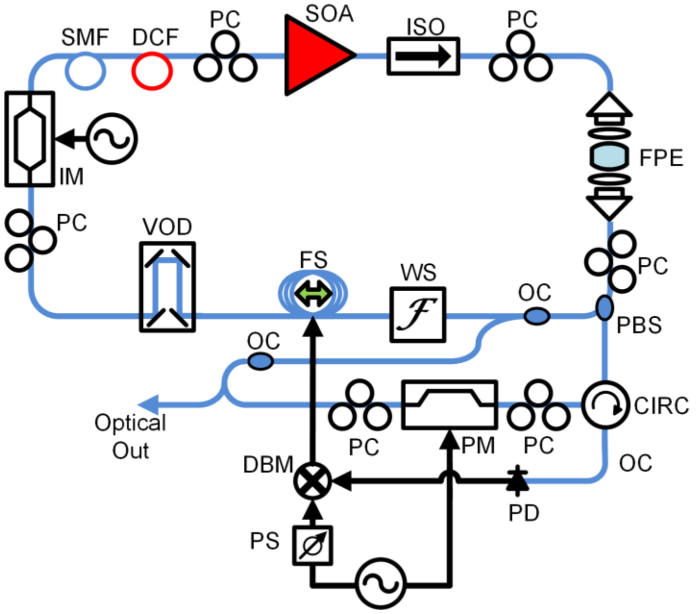

Figure 4.1 Schematic of harmonically mode-locked semiconductor laser with programmatic dispersion control. SOA, Semiconductor Optical Amplifier; ISO, Optical Isolator; PC, Polarization Controller; FPE, Fabry-Pérot etalon; PBS, Fiberized Polarization Beam Splitter; OC, Output Coupler; WS, Finisar Waveshaper; FS, Fiber Stretcher; VOD, Variable Optical Delay; IM, Intensity Modulator; SMF, Single Mode Fiber; DCF, Dispersion Compensating Fiber; PM, Phase Modulator; CIRC, Circulator; PD, Photodetector; DBM, Double Balanced Mixer; PS, Phase Shifter.

Due to dispersion in fiber, the cavity mode spacing changes across the optical spectrum which limits the achievable bandwidth, and so ~2 m dispersion compensating fiber is added to the cavity to reduce the overall net cavity dispersion and increase bandwidth. A commercial programmable pulse shaper, a Finisar Waveshaper, is also added to the cavity to correct for residual higher order dispersion as well as variations in gain flatness. Programmable control over cavity dispersion and loss provides the ability to maximize the lasing bandwidth, enabling ultrashort pulse production and increasing utility for telecom applications such as wavelength division multiplexing.

The output from the laser cavity is split into two branches, one of which is used for the Pound-Drever-Hall stabilization scheme described in the following section. The other portion serves as the primary optical output for the application of interest as well as for diagnostic purposes. The average power of the usable output is typically around 1 mW for this particular system. This is lower than that of the laser systems in CHAPTER 3:, but this can be attributed to the additional intracavity loss introduced by the Waveshaper.

4.1.1 Pound-Drever-Hall Stabilization

The Pound-Drever-Hall stabilization scheme was originally developed for the locking of a CW laser to an optical resonant cavity [68].The primary advantage of the PDH scheme is the ability to decouple intensity and frequency fluctuations, enabling locking of a laser to a resonance peak. Unlike other methods which monitor fluctuations in transmitted power and thus require locking to the side of a resonance for high sensitivity (i.e. the transmitted power exhibits large changes for small shifts in laser frequency) [69], the PDH method minimizes reflected power and adds sidebands to the laser which serve as phase references to indicate the sign of frequency fluctuations relative to the cavity resonance. A schematic of this stabilization method is shown in Figure 4.2.

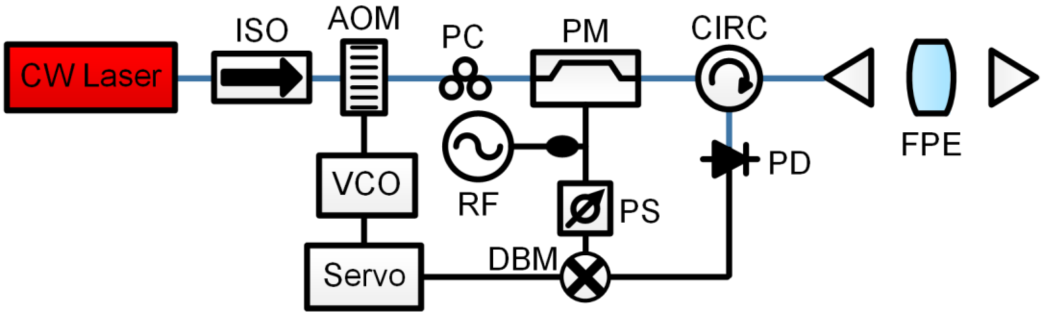

Figure 4.2 Pound-Drever-Hall stabilization setup. ISO, Isolator; AOM, Acousto-Optic Modulator; PC, Polarization Controller; PM, Phase Modulator; CIRC, Circulator; FPE, Fabry-Pérot etalon; PD, Photodetector; DBM, Double Balanced Mixer; PS, Phase Shifter; RF, Radio Frequency Synthesizer; VCO, Voltage Controlled Oscillator.

A phase modulator adds sidebands to the CW laser which is then reflected off a Fabry-Pérot etalon. The modulation frequency is sufficiently large such that the sidebands are far from a resonance and fully reflected while the center laser tone is partially reflected and picks up a phase shift. The laser and sidebands are photodetected and the resulting heterodyne beat signal is mixed with a phase reference from the modulation signal to produce an error signal that is antisymmetric about the etalon resonance [70]. This error signal is used to feedback to an actuator such as an acousto-optic modulator to lock the laser frequency to the etalon.

In the laser system of Figure 4.1, we use a modified PDH scheme in the sense that both the FPE and the stabilizing actuation (i.e. the fiber phase shifter) are contained within the laser cavity. While an intracavity FPE provides the benefits previously discussed, this does also complicate the system and overcorrection by the actuator can disrupt mode-locking. The other main difference from classic PDH is that multiple modes of the MLL are simultaneously locked to multiple FPE resonances rather than a single frequency lock as described above. Even with narrow optical bandpass filtering, multiple modes contribute to the error signal, which has the effect of blurring or reducing visibility of the primary locking feature in the error signal making stabilization more difficult.

4.2 Dispersion Optimization

Optimization of the cavity dispersion was first approached through the inclusion of dispersion compensating fiber with normal dispersion (D<0). A systematic study was performed by incrementally increasing the amount of normal dispersion in the cavity using various lengths of DCF and standard anomalous dispersion SMF [71]. Rather than start with a long length of DCF and gradually cut back to the optimal length, we leveraged the fact that the dispersion of SMF

(16.9 ps/nm/km) is a tenth of the magnitude and opposite in sign of that of DCF (-170 ps/nm/km). So by adding varying lengths of SMF to the DCF, we could finely adjust the added effective normal dispersion. Results of interest from this study are shown in Figure 4.3.

In Figure 4.3a, a baseline optical spectrum is shown when no DCF or SMF is added to the cavity. A spectrum such as this, with a peak on the long wavelength edge and a gradual rolling off toward shorter wavelengths, is a characteristic spectrum for an all-anomalous dispersion cavity of the type described in Sections 3.3, 3.4, and 4.1. Figure 4.3b shows the broadest observed spectrum achieved when 2 m DCF and 4 m SMF were added to the existing cavity. Although the laser is not able to be PDH stabilized in this state and there is significant variation in power across the spectrum, the significant broadening of the spectrum is encouraging.

Using the cavity state from Figure 4.3b as a reference point, Figure 4.3c shows the spectrum when an additional 2 m of SMF is added to the cavity. Adding 2 m of SMF (Figure 4.3c) increases the amount of anomalous dispersion, leading to a spectrum state resembling that of Figure 4.3a from the all-anomalous dispersion cavity. The spectrum is broader as compared to Figure 4.3a, which can be attributed to the overall reduced net cavity dispersion. The ripple across the top of the spectrum is likely due to polarization effects from imperfect alignment of the multiple polarization controllers in the cavity, which needed to be adjusted with each addition of new fiber to the cavity. Also note the presence of an isolated, narrow band of lasing spectrum near 1560 nm. This dual wavelength band behavior was observed only when the net dispersion was low and may represent the simultaneous lasing of a second supermode separate from that in the 1540 – 1550 nm band.

The spectrum in Figure 4.3d is a result of removing 2 m of SMF as compared to the cavity state of Figure 4.3b. This decreases the anomalous dispersion, effectively increasing the amount of normal dispersion, and leads to a spectrum state typically associated with dispersion compensated cavities for this laser architecture. A flat-top spectrum with sharp edges is produced, spanning more than 5 nm. The square spectrum was found to narrow as the amount of normal dispersion increased. Taking this result in context with Figure 4.3a-c, it is clear there are two regimes of operation associated with excess anomalous dispersion (Figure 4.3a,c) and excess normal dispersion (Figure 4.3d) as well as a transition state (Figure 4.3b) exhibiting some characteristics of both regimes and capable of producing broad bandwidth.

The cavity round trip time was also found to have a critical role in determining the final spectral output. In Figure 4.3e and Figure 4.3f, we return to the cavity state from Figure 4.3b (2 m DCF and 4 m SMF added) and the VOD contained in the laser cavity is changed. The VOD is fiber coupled but consists of a free space delay line, so cavity length changes are largely decoupled from changes in the net dispersion. As compared to the cavity from Figure 4.3b, the total cavity length is increased by 330 µm to produce the spectrum in Figure 4.3e and decreased by 300 µm to produce the spectrum in Figure 4.3f. Notice that these short free space cavity length changes are sufficient to change the spectrum from that of Figure 4.3b to states resembling either the excess anomalous dispersion regime or the excess normal dispersion regime. That is to say, a dispersion compensated cavity can be made to switch between regimes with just a small change in free space cavity length. This raises the question of how to identify when the proper amount of DCF has been added to the cavity. From our observations, when changing the cavity length to move from one operating regime to the other, the transition state bandwidth was broadest when dispersion was minimized.

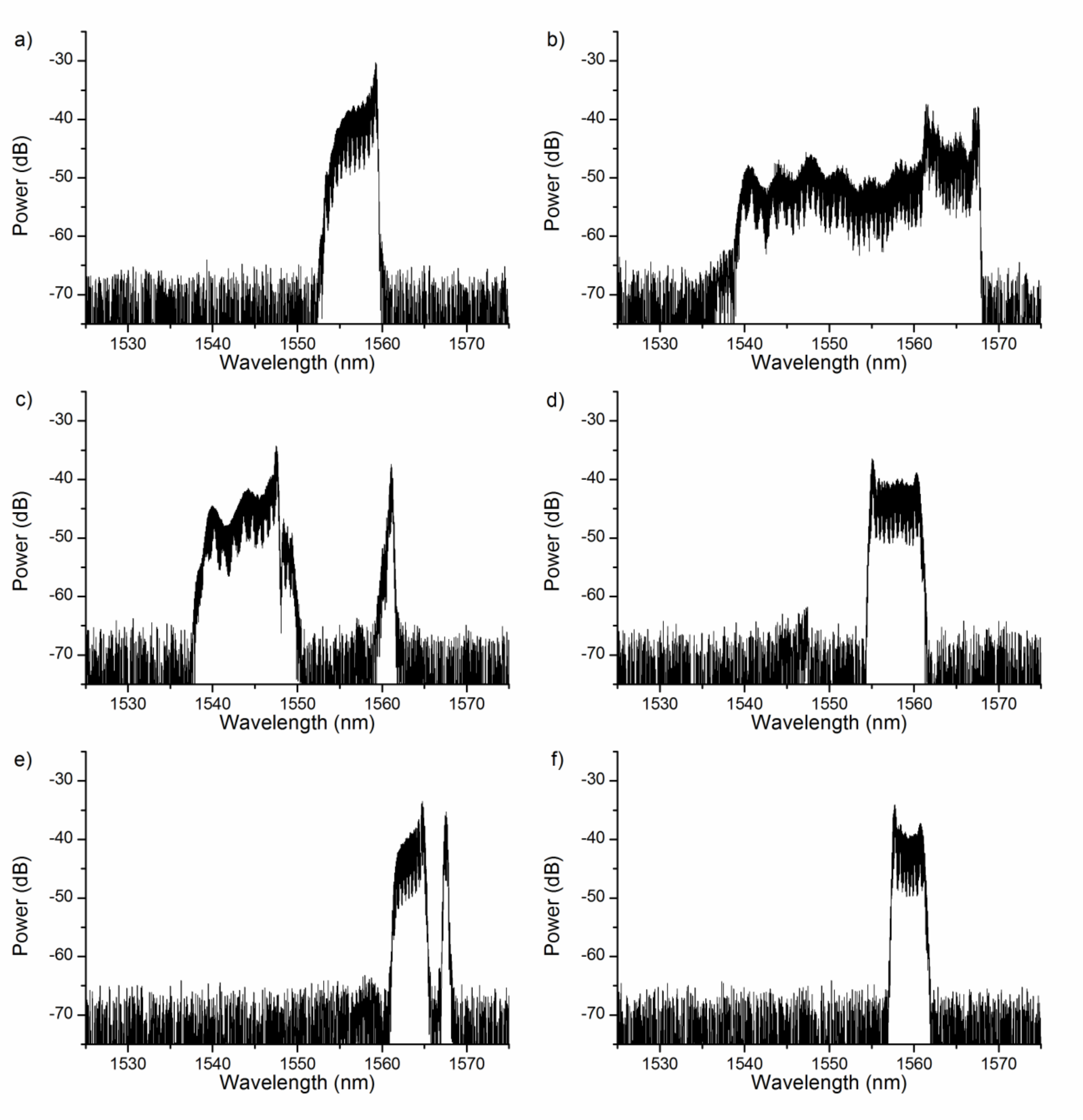

Figure 4.3 Optimization of dispersion compensating fiber length and freespace variable optical delay. a) Baseline spectrum with no DCF in cavity. b) Broadband spectrum with 2m DCF and 4m SMF added to cavity. c) Spectrum with excess anomalous dispersion. 2m DCF and 6m SMF in cavity. d) Spectrum with excess normal dispersion. 2m DCF and 2m SMF in cavity. e) Spectrum from dispersion compensated cavity (2m DCF, 4m SMF) with variable optical delay increasing freespace cavity length by 330 μm. f) Spectrum from dispersion compensated cavity (2m DCF, 4m SMF) with variable optical delay decreasing freespace cavity length by 300 μm.

From this point, the Waveshaper was utilized to further broaden the laser bandwidth and improve spectral flatness. A custom Labview interface was designed and coded to control the Waveshaper and allow for the application of amplitude and phase masks defined by an arbitrary number of polynomials of arbitrary order over an arbitrary range. Masks used the inverse of the retrieved spectral phase profiles from the lasers of CHAPTER 3:, and then were empirically refined from observations of the laser's optical and RF spectra. This was particularly challenging as the Waveshaper was part of the laser cavity and so pulses experienced the Waveshaper's effect every round trip, making the system response highly nonlinear in that small changes in the amplitude or phase mask could cause the laser to operate in an entirely different wavelength band. One observation of note was that in absence of any spectral mask applied, the laser tended to operate at the long wavelength edge of the Waveshaper transmission window, as can be seen in Figure 4.3b where the Waveshaper transmission stops at ~1568 nm. Slight attenuation of the longer wavelengths was found to broaden the spectrum and optimization of the second and third order phase coefficients helped to improve spectral flatness. Finally, fine adjustment of the free space cavity length enabled spectra spanning the entire Waveshaper transmission window from 191.15 THz to 196.275 THz.

This strong relationship between cavity dispersion and achievable bandwidth is related to the uniformity of spacing of cavity modes across the SOA's gain bandwidth. When actively mode-locking with an intensity modulator as done here, cavity modes spaced by the modulation rate share energy and become phase locked. However, the modulation sidebands created by the intensity modulator are inherently evenly spaced, so dispersion may cause cavity modes to walk off from the modulation sidebands. The laser spectrum is limited by the point at which cavity modes have walked off sufficiently far enough from the modulation sidebands that they can no longer be mode-locked. That the bandwidth is primarily limited by this effect is supported by the fact that the operating regimes and behavior shown in Figure 4.3 can also be observed even with the Fabry-Pérot etalon removed from the cavity. The etalon does play a secondary effect in limiting the bandwidth if there is a mismatch between the etalon FSR and the modulation rate, causing the mode-locked spectrum to walk off from the etalon resonances.

4.3 Experimental Results with 10 GHz, 1000 Finesse Etalon

In this section, the laser system described above is characterized in several different states and the results are presented. In each case, the SOA is driven with 600 mA of current, the mode-locking frequency is 10.285325 GHz, and all fiber lengths (DCF and SMF) in the cavity are fixed. What is differed is the freespace variable optical delay and the spectral mask applied by the intracavity Waveshaper to change the net cavity dispersion or loss.

4.3.1 Characterization of Baseline State without Waveshaper Masks

As a baseline characterization, no spectral amplitude or phase mask is applied to the Waveshaper. The best performance in this case is seen in Figure 4.4. A square spectrum spanning 8 nm is achieved, with Optical Signal-to-Noise Ratio of >40 dB. As mentioned in the previous section, it was possible by changing the free space cavity length to switch between the square spectrum operating regime shown here and the broader bandwidth transition state. The state producing the results in Figure 4.4 was chosen as it was lower noise than the broadband transition state and easier to PDH stabilize. Output pulses in this state are up-chirped, but are compressible to autocorrelation widths of 3 ps (2.6 times transform limited) in ~500 m SMF. A sampling oscilloscope trace of the photodetected pulse train in Figure 4.4d shows well-defined, steady pulses, and a >80 dB SNR of the 10 GHz carrier frequency is exhibited in the RF spectrum in

Figure 4.4e. Spurs offset from the carrier by the cavity fundamental frequency are suppressed below the measurement floor, indicating good selection of a single axial mode group.

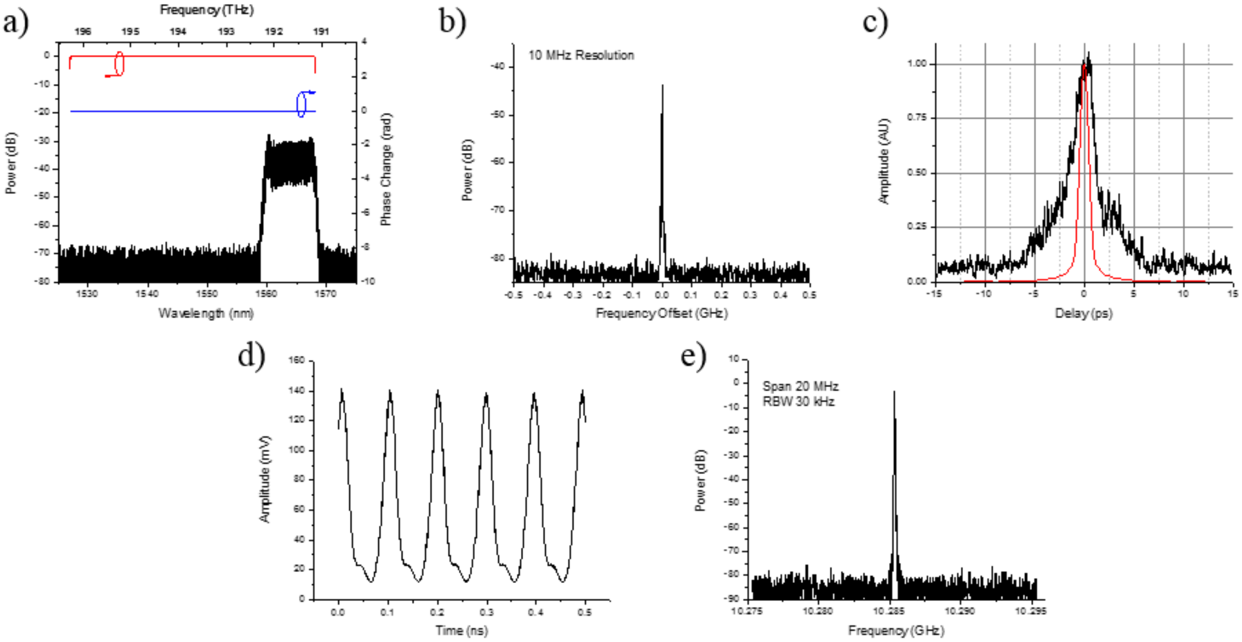

Figure 4.4 Characterization of mode-locked laser with no masks applied to Waveshaper. a) Optical spectrum. Red trace indicates amplitude mask and blue trace indicates phase mask. b) High resolution optical spectrum. c) Pulse intensity autocorrelation. Red trace is the theoretical transform-limited autocorrelation for comparison. d) Sampling oscilloscope trace. e) RF spectrum of photodetected pulse train.

4.3.2 Characterization of Lowest Noise State

In Figure 4.5a, a small amount of attenuation is applied to the long wavelength side of the Waveshaper transmission window to force the spectrum towards shorter wavelengths and into a lockable state. Positive quadratic phase was also applied to slightly broaden the spectrum as compared to the baseline spectrum of Figure 4.4a. With a 10.5 nm wide spectrum, autocorrelation widths of ~3 ps are obtained (3.1 times transform limited) and >75 dB SNR in the RF spectrum.

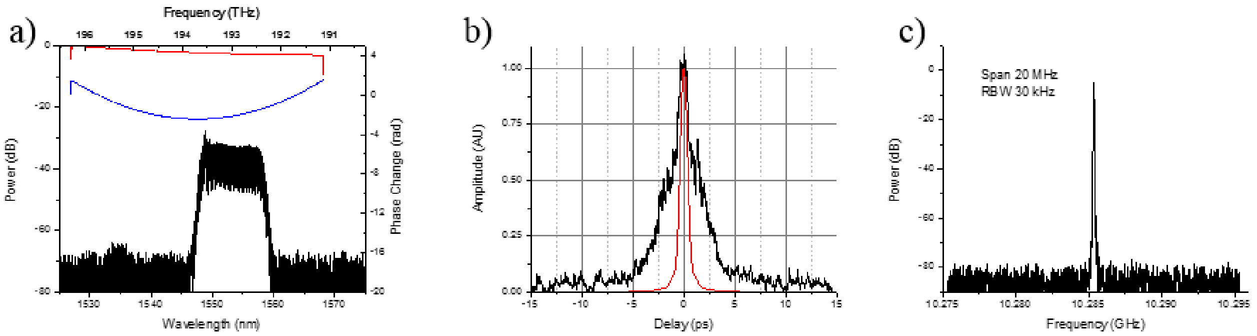

Figure 4.5 Mode-locked laser characteristics in lowest noise state. a) Optical spectrum. b) Pulse intensity autocorrelation. c) RF spectrum.

The comb's axial mode linewidth was characterized by measuring a heterodyne beat between a single comb line and a narrow linewidth (~30 Hz) CW laser. The results of this measurement are seen in Figure 4.6a, where a Lorentzian curve with a width of 1 kHz is fit to the beat signal. The good fit agreement near the peak and the lower noise at higher offsets indicate an axial mode linewidth of less than 1 kHz. In addition to the linewidth measurements, the heterodyne beat frequency was tracked over ~25 seconds to quantify the optical frequency stability. The movement of the beat frequency is shown in the spectrogram of Figure 4.6b, demonstrating less than 400 kHz drift between the CW laser and the MLL comb line over the 25 second record. It should be noted the measured 400 kHz drift represents an upper bound on the MLL's frequency stability, as the CW laser was found to fluctuate significantly over the course of the measurement.

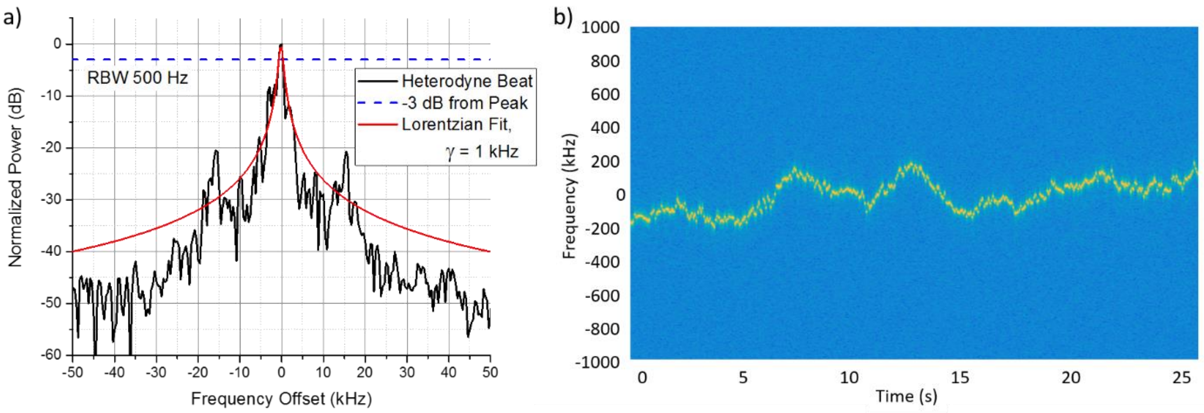

Figure 4.6 Axial mode linewidth (a) and frequency stability (b) measurements obtained from heterodyne beat with ~30 Hz linewidth CW laser.

To determine the pulse train stability in this state, noise measurements are made on the photodetected signal. The residual single sideband phase noise is measured by mixing the photodetected signal in quadrature with the modulation signal from the RF synthesizer and measuring the power spectral density at various Fourier frequencies [72]. Amplitude noise can also be measured through the power spectral density of the photodetected signal. The phase noise measurements are shown in Figure 4.7a along with the integrated timing jitter, totaling 2 fs of jitter integrated from 100 MHz in to 1 MHz and 12 fs integrated from 100 MHz to 1 Hz. At offsets from the carrier of greater than 1 MHz, a noise floor of -160 dBc/Hz is reached. If this noise floor is shot noise limited, then using a photodetector capable of handling higher optical powers [73] and optimally compressing the pulses before detection can further reduce the noise floor. Ultrashort pulses at the photodetector not only increase the power in the carrier frequency, but also lead to correlations in the shot noise which can decrease the noise floor below the classic stationary shot noise floor [74]. The noise spikes at 5.5 MHz and 11 MHz are supermode noise spurs from the harmonic mode-locking process that are incompletely suppressed by the FPE. They can be further mitigated by shortening the cavity length, which increases the cavity fundamental frequency and pushes the spurs outside the FPE passband, or employing a higher finesse etalon. The spurs at 60 Hz and between 100 Hz to 1 kHz are due to line noise and its harmonics. Amplitude noise measurements are shown in Figure 4.7b, exhibiting a pulse-to-pulse energy fluctuation of ~0.09% integrated from 100 MHz in to 1 Hz.

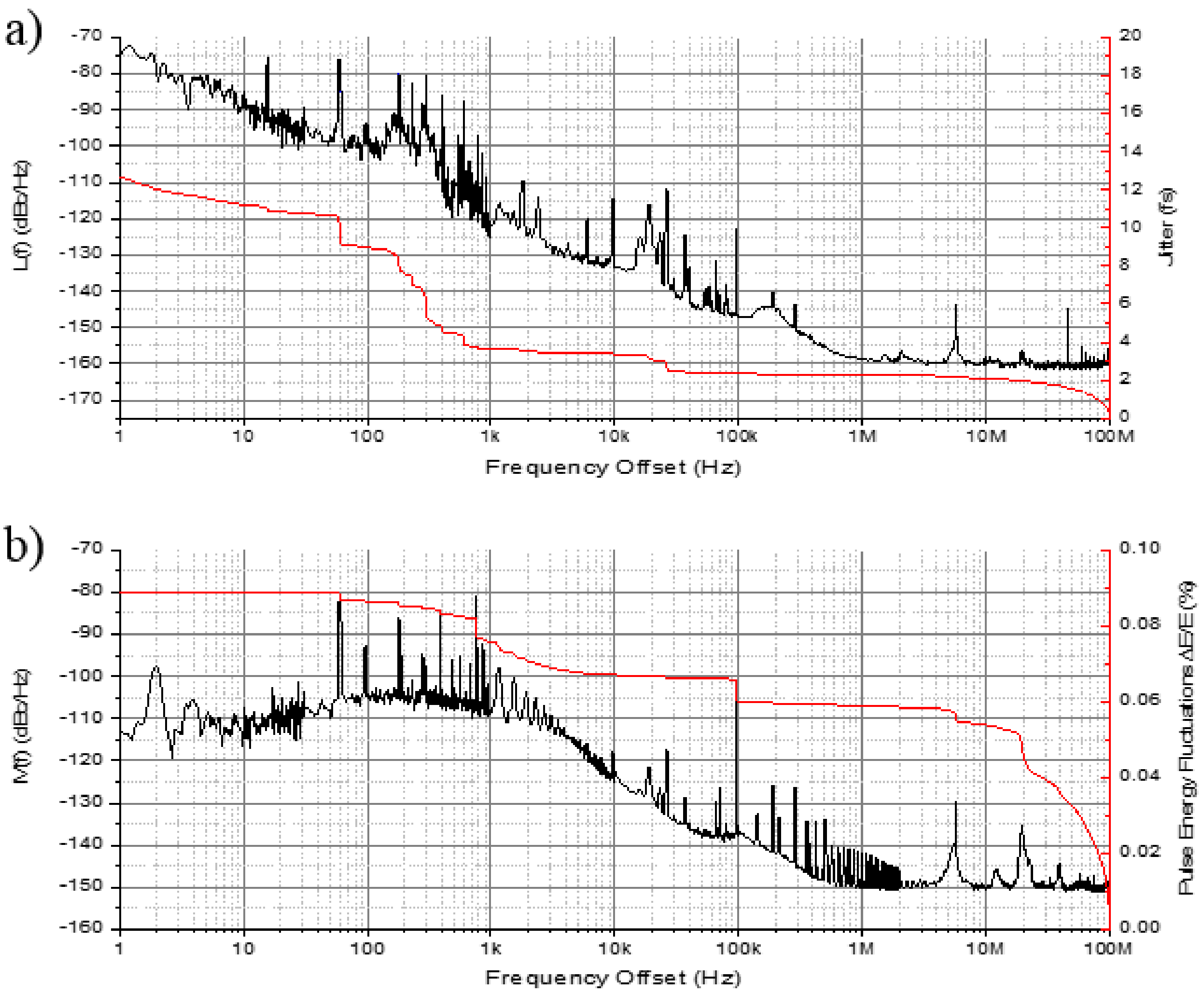

Figure 4.7 Noise characteristics of photodetected pulse train from MLL in lowest noise state. a) Single sideband residual phase noise (black) and integrated timing jitter (red). b) Amplitude noise (black) and integrated pulse-to-pulse energy fluctuations (red).

To investigate the factors limiting the noise floor at high offsets, residual phase noise measurements were later repeated with the laser operating in a similar state, as seen by the 6.5 nm wide spectrum centered at 1550 nm in Figure 4.8a and the 2 ps intensity autocorrelation in Figure 4.8b. Phase noise was initially measured using the same commercial high speed PIN photodiode as the one used in the measurements of Figure 4.7. The black trace of Figure 4.8c shows these results. The commercial detector was then replaced by a prototype device (Freedom Photonics FP1015a) capable of handling higher optical power and the red trace of Figure 4.8c was obtained for the same optical power present on the detector. It should be noted that an RF amplifier was used after photodetection in both cases to increase the RF signal power to a level measurable by the carrier noise test set and a variable attenuator was used to match signal power between test cases. The measured phase noise is nearly identical between these two cases, with the most noticeable differences being the moderately lower noise between offsets of 1 Hz to 10 Hz and slightly *higher* noise at offsets above 10 MHz. To leverage the potential of the high power handling detector, an erbium fiber amplifier was used to double the amount of optical power present on the detector to 20 mW and the blue trace in Figure 4.8c was obtained. The RF signal power was again matched to the previous two cases. The phase noise is measured to be substantially higher at all offsets up to ~100 kHz and at frequency offsets >10 MHz, the phase noise is found to be lower than the previous case with the same detector as expected. However, at offsets >10 MHz, the phase noise exactly matches the original case with the commercial detector despite significantly more power on the detector. This seems to suggest the noise floor is not being limited by shot noise but some other factor. Noise originating from the amplifier used after the RF synthesizer (before splitting between the intensity modulator signal and the reference signal for residual phase noise measurements) could be playing a role, and will be investigated further.

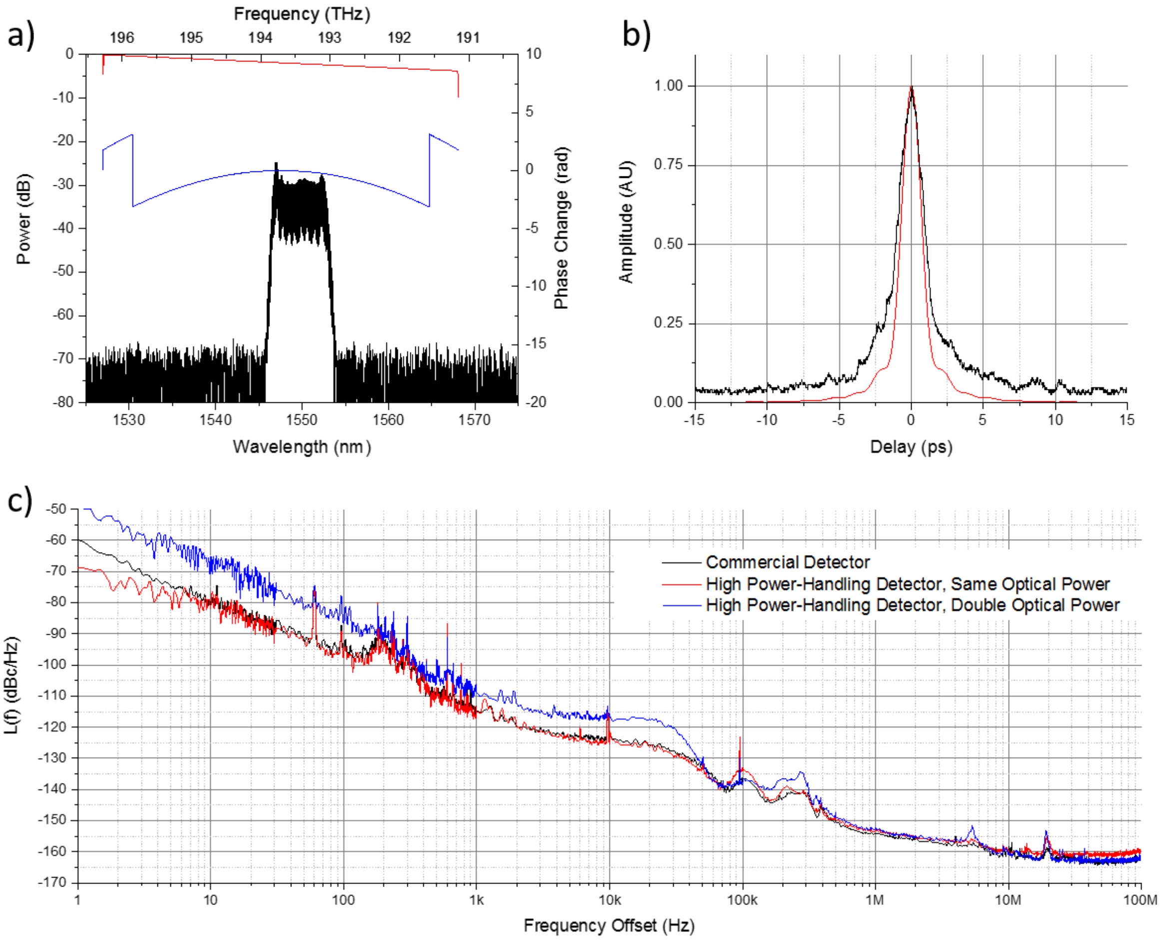

Figure 4.8 Study of impact of optical power and detector power handling capabilities on phase noise floor. Optical spectrum (a) and pulse autocorrelation (b) used during these measurements. Phase noise measurements (c) with commercial detector (black), high power handling detector (red), and double optical power on high power handling detector (red). RF signal power is held constant across measurements.

4.3.3 Characterization of Broad Bandwidth, Low Noise State

Having established a baseline performance level both without any spectral shaping and with shaping for lowest noise possible, we endeavored to broaden the spectrum as much as possible while maintaining a low noise output. These results are shown in Figure 4.9, where the spectrum has been broadened to 28 nm by gradually increasing attenuation as wavelength increases and applying positive quadratic phase (effectively anomalous dispersion) with a small amount of negative cubic phase. With the broadened spectrum, pulses are compressible to sub-picosecond widths. A side effect of the broader spectrum is that more comb lines contribute to the error signal, further obscuring the lockable features and making PDH stabilization more difficult. This produces a moderately noisier pulse train, as evidenced by the sampling scope trace and the broader RF linewidth.

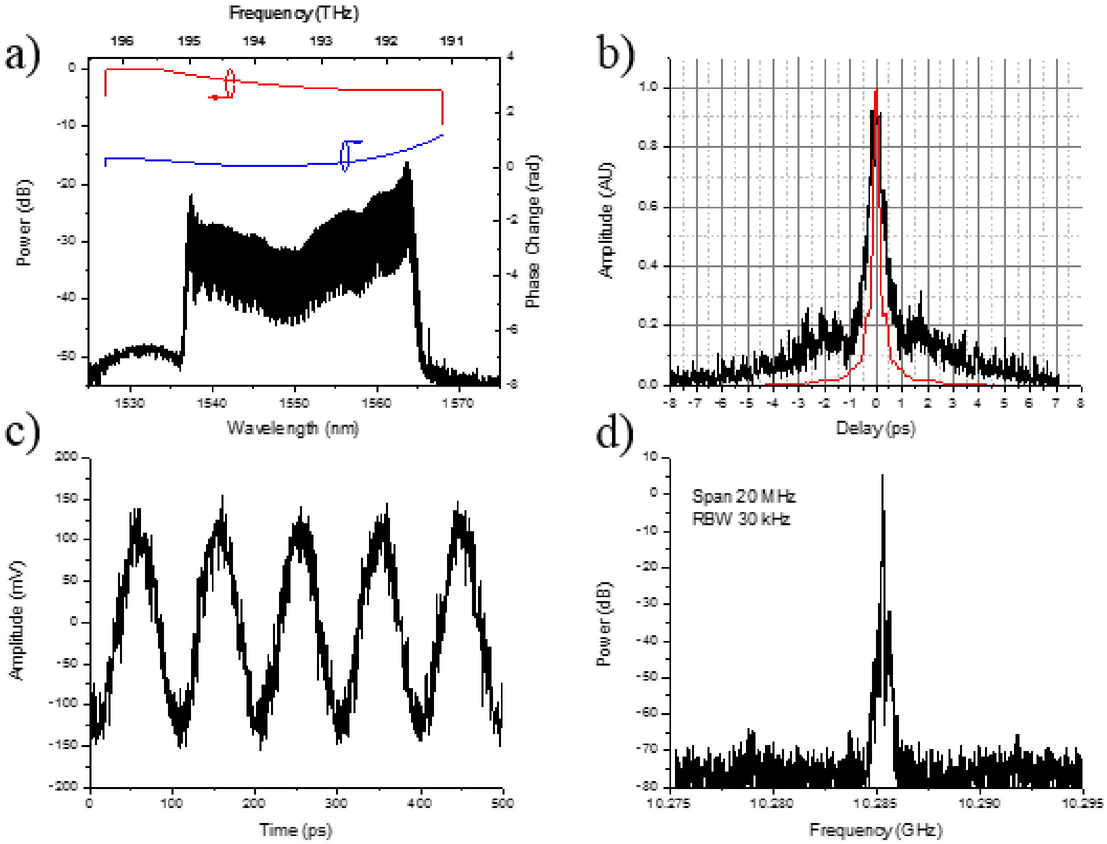

Figure 4.9 Spectrally broadened mode-locked laser. a) Optical spectrum. b) Pulse intensity autocorrelation. c) Sampling oscilloscope trace. d) RF spectrum.

The phase noise was also measured and is shown in Figure 4.10. Compared to the phase noise in Figure 4.7a, the noise here is generally higher across all offsets. At low offsets, the increased noise can be attributed to technical noise and can be reduced with better isolation and PDH locking. The noise bump around 6 MHz was found to be due to noise in one of the RF sources and was later corrected. Finally, less optical power was supplied to the photodetector, which accounts for the higher noise floor at offsets above 10 MHz. Despite the increased noise, timing jitter integrated from 100 MHz to 1 MHz is still only 12 fs and integrating over the entire offset range yields 31 fs of jitter. This represents a promising step towards maximizing the MLL's lasing bandwidth while also producing a low noise pulse train.

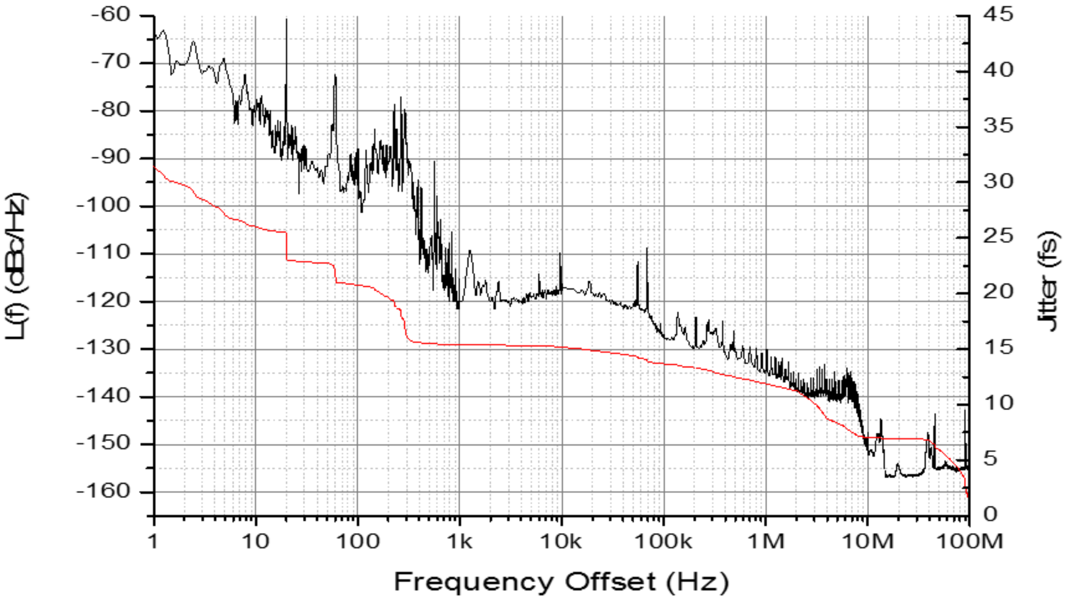

Figure 4.10 Phase noise (black) and integrated timing jitter (red) of spectrally broadened MLL.

4.3.4 Characterization of Maximum Bandwidth State

In Figure 4.11, the spectral amplitude and phase masks are optimally tuned for maximum bandwidth. As in Figure 4.9a, the long wavelength side is more strongly attenuated than the short wavelength side and a phase mask with positive quadratic and negative cubic coefficients is applied. Through application of these masks and careful optimization of the cavity length, the spectrum is broadened to span 38 nm and contains ~500 comb lines, nearly filling the entire transmission window of the Waveshaper. To the best of our knowledge, this is the broadest

10 GHz frequency comb obtained directly from a semiconductor MLL. Stability is degraded in this state, as seen by the presence of large supermode noise spurs in the RF spectrum in Figure 4.11b. Future work is required to be able to stabilize the MLL and reduce noise while preserving the broad bandwidth.

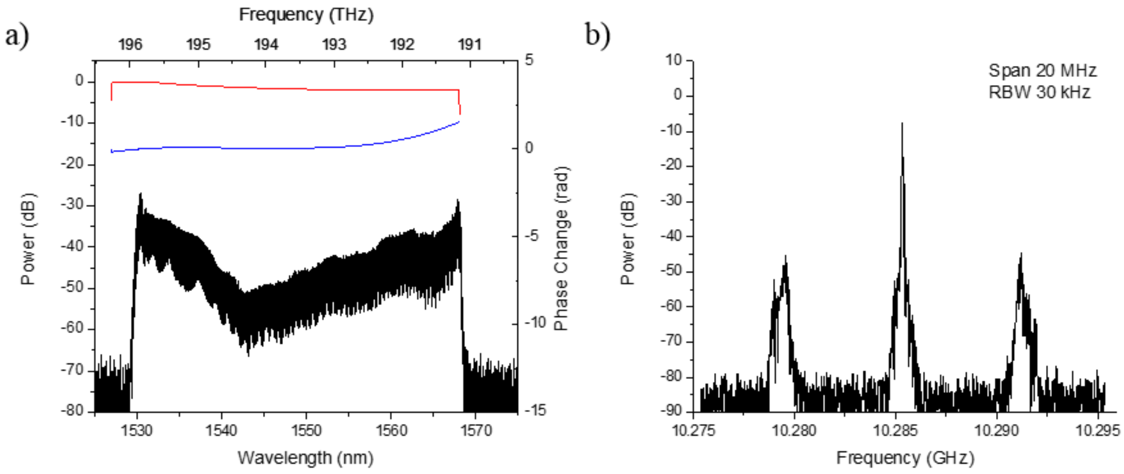

Figure 4.11 Characterization of MLL optimized for maximally broadened spectrum. a) Optical spectrum. b) RF spectrum.

4.4 Experimental Results with 8 GHz, 30000 Finesse Etalon

Replacing the 10 GHz, 1000 finesse etalon with one of higher finesse offers the potential for substantial improvement in laser performance with respect to suppression of supermode spurs, axial mode linewidth, and quality of PDH stabilization. A 30,000 finesse etalon with 8 GHz free spectral range and ~260 kHz passband widths was added to the laser cavity of Section 4.1 in place of the previous etalon. One drawback of incorporating a higher finesse etalon in the laser cavity is the potential reduction in achievable bandwidth due to modes slightly off from an etalon resonance peak being attenuated much more strongly. Results from the operation of the laser in this configuration are shown in Figure 4.12.

Figure 4.12a shows the optical spectrum of the 8 GHz laser along with the applied Waveshaper masks. Bandwidth is significantly reduced as compared to the spectra in Figure 4.9a and Figure 4.11a. This is due in part to the increased filtering by the higher finesse etalon as well as suboptimal free space cavity length adjustment and Waveshaper spectral masks. A clear 8 GHz pulse train is produced however, as seen in the sampling oscilloscope trace of Figure 4.12b, and the photodetected RF spectrum in Figure 4.12c shows supermode spurs have been suppressed below the noise floor of the spectrum analyzer. Linewidth and stability are expected to have improved, which will be verified in future work.

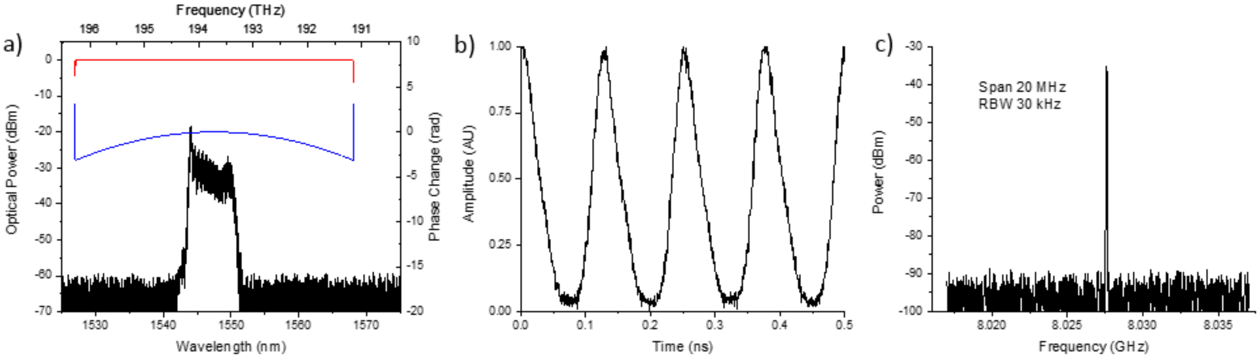

Figure 4.12 Results from 8 GHz mode-locked laser employing higher finesse etalon. a) Optical spectrum. Red trace indicates amplitude mask applied by Waveshaper and blue trace indicates the phase mask. b) Sampling oscilloscope trace. c) Photodetected RF spectrum.

4.5 Conclusion

In this chapter, we have detailed a mode-locked laser architecture capable of producing optical frequency combs with comb lines spaced by 10 GHz and spanning 5 THz of optical bandwidth. This is achieved through careful optimization of the amount of dispersion compensating fiber added to the cavity and the spectral amplitude and phase masks applied by an intracavity pulseshaper. In the time domain, sub-picosecond pulses can be generated in pulse trains with femtosecond level timing jitter. This source holds great potential for many applications.

CHAPTER 5: BROADBAND COUPLED OPTO-ELECTRONIC OSCILLATOR WITH NOVEL STABILIZATION SCHEME

The large, costly RF synthesizers required for the MLL architecture of Figure 4.1 can be eliminated to make the system a stand-alone oscillator by regeneratively mode-locking the laser to form a Coupled Opto-Electronic Oscillator (COEO). In the following chapter, we present this COEO system by first introducing the opto-electronic oscillator (OEO), then a general COEO, and finally the optically filtered COEO. In Section 5.2, we present the opto-electronic loop design of the full system and a stabilization scheme using multiple Pound-Drever-Hall error signals from different regions of the spectrum. Section 5.3 contains results from the characterization of this system.

5.1 Coupled Opto-Electronic Oscillator Background

The COEO can be understood by first examining the simpler OEO [75]. In a standard OEO like that in Figure 5.1, light from a CW laser is modulated usually by an electro-optic intensity modulator. The modulated light is photodetected, producing a heterodyne beat at the modulation frequency and its harmonics. The beat frequency is amplified, bandpass filtered, and then divided, with one arm serving as the RF output and the other being the driving signal applied to the modulator. In this way, a hybrid optical-electrical loop is formed with resonant modes defined by the total loop length. Oscillation at a resonant RF frequency builds up from noise in the photodetected signal of the CW laser. The RF filter selects oscillation at a single resonant RF frequency, but is susceptible to environmental fluctuations which introduce noise to the oscillator.

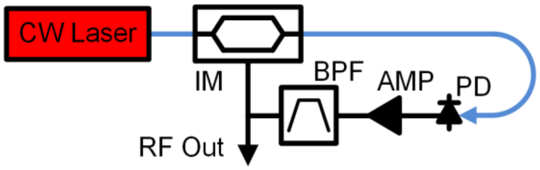

Figure 5.1 Opto-Electronic Oscillator schematic. IM, Intensity Modulator; PD, Photodetector; AMP, Amplifier; BPF, Band-Pass Filter.

A COEO differs from an OEO in that the laser is no longer an independent oscillator outside the OEO loop. In a COEO, the intensity modulator is placed inside a laser cavity to force mode-locking as shown in Figure 5.2, and thus couples the optical oscillator to the opto-electronic oscillator [76]. Heterodyne beats between optical cavity modes on the photodetector seed the opto-electronic oscillation and, as in the OEO, conventionally an RF filter is used to select a single harmonic of the beat frequency [77, 78]. However, care must be now be taken to adjust the opto-electronic (OE) loop length such that an OE loop mode is commensurate with the heterodyne beat frequency. That is to say, a definite relationship must be maintained between the optical loop length and the opto-electronic loop length, whereas the loop length in the OEO is a free parameter provided a single harmonic can still be selected by the BPF.

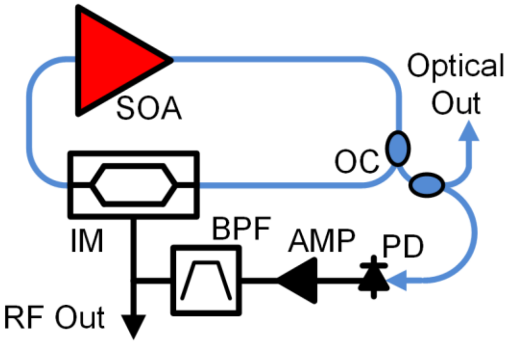

Figure 5.2 Coupled Opto-Electronic Oscillator schematic. SOA, Semiconductor Optical Amplifier; OC, Output Coupler; IM, Intensity Modulator; PD, Photodetector; AMP, Amplifier; BPF, Band-Pass Filter.

The COEO is an appealing system for a number of reasons. Firstly, a COEO can produce low noise RF signals like an OEO, but without the need for a stable CW laser to do so. In addition, the COEO can produce ultrashort pulses at GHz rates at the same time as RF signals, which can be advantageous for synchronization while sampling. Finally, the COEO manages to produce both optical and RF outputs while eliminating large and expensive external RF oscillators like that required for the system of Section 4.1, enabling this to be a stand-alone system with reduced size and cost. One disadvantage of the conventional COEO is the reliance on the RF filter to select the oscillation frequency. The temperature sensitivity of the filter's center frequency can adversely affect the COEO stability [79]. Additionally, there is no mechanism in an RF filtered COEO to select a single optical axial mode group. As such, the output optical spectrum is that of a harmonically MLL with modes spaced by the cavity fundamental frequency (MHz level or less) [78], preventing access to individual modes and thus precluding applications such as wavelength division multiplexing and line-by-line pulse shaping.

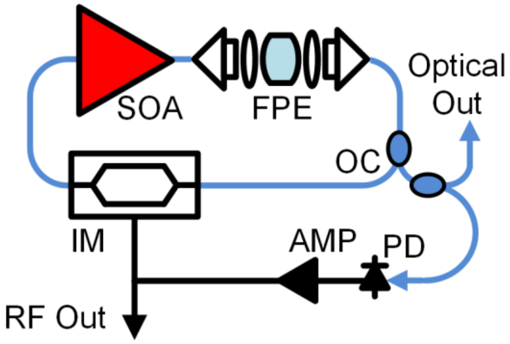

Figure 5.3 Coupled Opto-Electronic Oscillator with optical filtering. SOA, Semiconductor Optical Amplifier; FPE, Fabry-Pérot etalon; OC, Output Coupler; IM, Intensity Modulator; PD, Photodetector; AMP, Amplifier.

One way to eliminate the RF filter from the OE loop is to add an FPE to the optical cavity [63] as seen in Figure 5.3. The FPE effectively moves the mode filtering from the electrical domain to the optical domain. Rather than selecting a specific RF harmonic, the FPE filters a selection of optical modes whose spacing – and hence RF beat frequency – corresponds to the desired OE oscillation frequency and harmonics thereof are filtered by the bandwidth limitations of the photodetector and amplifier. As a result, not only is the same OE oscillation frequency achieved without the RF filter, but a GHz spaced OFC can also be obtained. Figure 5.4 illustrates the difference between electrical and optical filtering in a COEO.

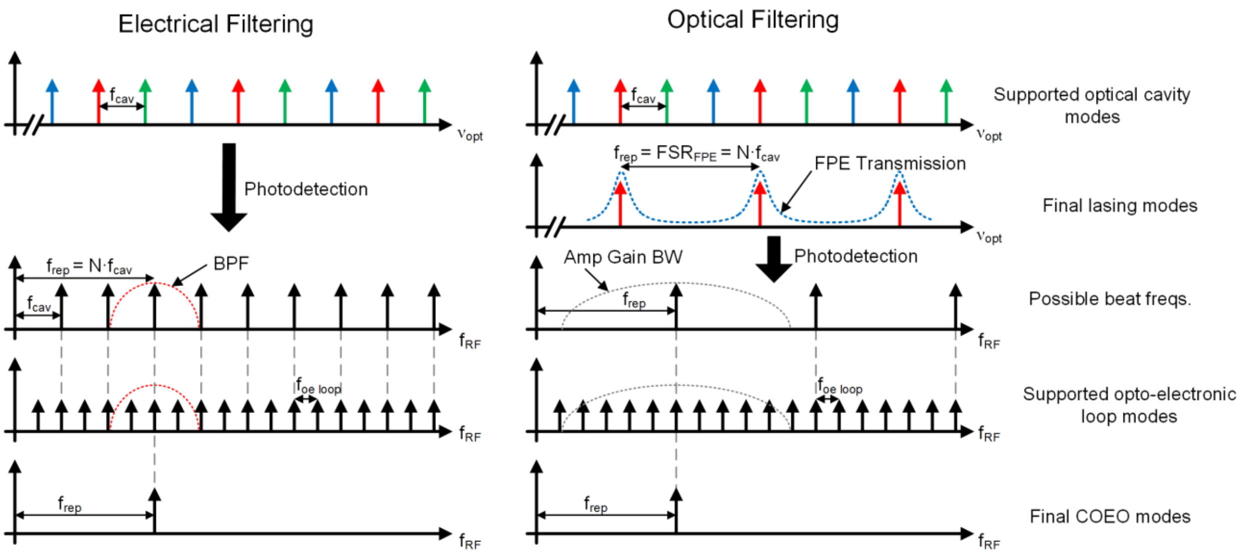

Figure 5.4 Frequency domain representation of filtering schemes in a COEO. Electrical filtering requires a narrowband RF BPF to select a single heterodyne beat harmonic for oscillation. Optical filtering with a FPE produces optical modes spaced by the desired OE oscillation frequency, thus generating only a single heterodyne beat within the system bandwidth and eliminating the need for the temperature-sensitive RF BPF. Adapted from [63, 76].

5.2 System Architecture

5.2.1 Design of Optical and Opto-Electronic Cavities

The full coupled opto-electronic oscillator architecture is shown in Figure 5.5. The laser of Figure 4.1 is used as the optical cavity of the COEO. A portion of the usable optical output is tapped off for diagnostics and the remaining majority is detected with a high speed (>16 GHz) photodiode. The photodetector filters out harmonics of the pulse train carrier frequency due to its limited bandwidth, leaving just an RF signal at the pulse train's repetition rate. This photodetected signal is amplified with a low noise amplifier and fed back to the intracavity intensity modulator, forming the hybrid opto-electronic loop. Some of the photodetected and amplified signal is frequency divided to use as a driving signal for the phase modulator in the Pound-Drever-Hall stabilization scheme. An RF phase shifter is included in the opto-electronic loop to ensure the carrier frequency round trip phase is a multiple of 2π (i.e. the photodetected beat signal is a harmonic of the opto-electronic loop mode spacing).

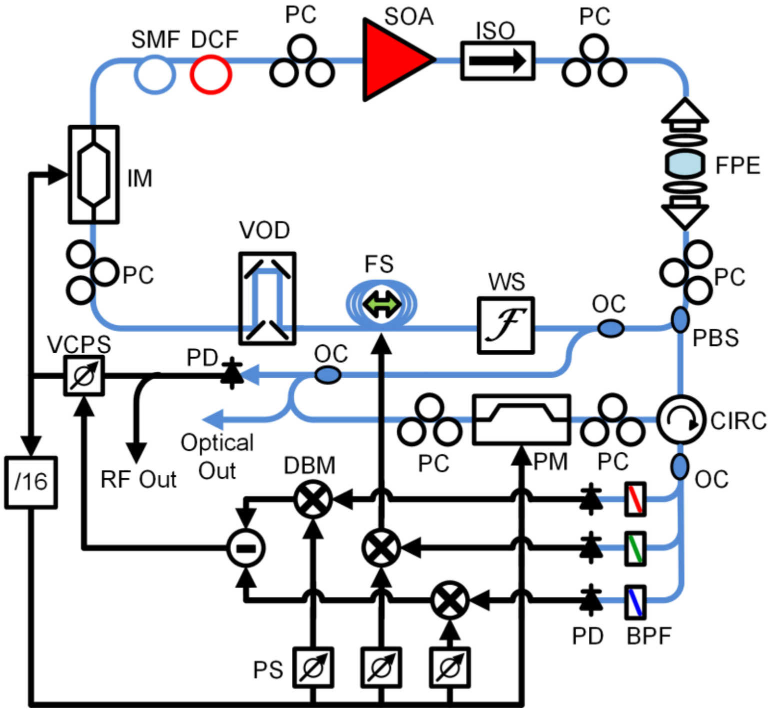

Figure 5.5 Frequency and repetition rate stabilized COEO architecture with three-point PDH stabilization. SOA, Semiconductor Optical Amplifier; ISO, Isolator; PC, Polarization Controller; FPE, Fabry-Pérot Etalon; PBS, Polarization Beam Splitter; OC, Output Coupler; WS, Finisar Waveshaper; FS, Fiber Stretcher; VOD, Variable Optical Delay; IM, Intensity Modulator; SMF, Standard Single Mode Fiber; DCF, Dispersion Compensating Fiber; PM, Phase Modulator; CIRC, Circulator; BPF, Optical Band Pass Filter; PD, Photodetector; DBM, Double Balanced Mixer; PS, Phase Shifter; VCPS, Voltage Controlled Phase Shifter.

5.2.2 Scheme for Simultaneous Decoupled Stabilization of Frequency and Repetition Rate

To stabilize both the frequency and the mode spacing of the optical frequency comb, a novel three-point Pound-Drever-Hall stabilization scheme is employed. The scheme uses the difference of two error signals to cancel fluctuations in optical frequency and isolate mode spacing changes. A third error signal for stabilizing the optical frequency is derived from the region of the spectrum insensitive to mode spacing changes. Knowledge of the fixed point frequencies for different system parameters along with the multiple error signal approach enables independent stabilization of frequency and mode spacing for ultralow noise performance

5.2.2.1 Fixed Point Analysis

When implementing a PDH stabilization scheme, it is critical to understand how feedback to a particular system parameter affects the MLL frequency and repetition rate. Changes in a parameter such as cavity length will cause both the frequency and repetition rate to vary, but these fluctuations will effectively cancel at some frequency, creating a "fixed point" that is insensitive to changes in the associated cavity parameter [80]. Though the fixed point frequency for a parameter may not coincide with an actual laser mode, frequency changes due to the parameter will appear to breathe or expand and contract about this point. As such, parameters with opportune fixed point frequencies can be particularly effective in stabilizing either the MLL frequency or mode spacing.

Determining the fixed point frequency for a given parameter can be achieved by measuring the changes in both the MLL repetition rate and optical frequency due to a known variation in the parameter. This can be shown following the derivation in [52], where $\Delta f_o = \Delta X \cdot \partial f_o / \partial X$ is the variation in the offset frequency f_o due to a change of ΔX in parameter X and similarly $\Delta f_{rep} =$

$\Delta X \cdot \partial f_{rep}/\partial X$ for the repetition rate f_{rep}. Changes in an optical frequency defined as $\nu \equiv n \cdot f_{rep} + f_o$ can be represented by changes in the repetition rate and offset frequency, $\Delta\nu = n \cdot \Delta f_{rep} + \Delta f_o$. The fixed point frequency does not vary due to ΔX, hence $\Delta\nu_{fix} = n_{fix} \cdot \Delta f_{rep} + \Delta f_o = 0$. Substituting the expressions above for Δf_{rep} and Δf_o, we find $n_{fix} = -\frac{\partial f_o/\partial X}{\partial f_{rep}/\partial X}$ and $\nu_{fix} = -\frac{\partial f_o/\partial X}{\partial f_{rep}/\partial X} \cdot f_{rep} + f_o$. The process of measuring changes in the repetition rate and offset frequency due to a known parameter modulation can be repeated for each relevant system parameter to map out the different fixed point frequencies.

This process has been performed for a fiber laser system [52] as well as a COEO system similar to the one described in this dissertation [81]. In both cases, changes in the fiber cavity length had a fixed point located far below the optical spectrum, meaning small changes in the fiber length could provide large changes in the position of the entire spectrum making it a suitable candidate for stabilization of the optical frequency. In the COEO, optoelectronic loop phase changes conveniently had a fixed point located near the center of the optical spectrum causing modes to breathe inward and outward from spectrum center, providing an effective feedback point for repetition rate changes [81].

5.2.2.2 Three-Point PDH

To fully leverage the identified fixed point frequencies, it is important to generate appropriate error signals sensitive to the parameter of interest and insensitive to fluctuations in other parameters. It is to this end that our system generates three separate PDH error signals from different filtered regions of the optical spectrum. The error signal used to feed back to the cavity fiber length and stabilize the optical frequency is derived from optical modes in the middle of the spectrum nearest the fixed point frequency for opto-electronic loop phase changes. In this way, the modes contributing to the error signal are insensitive to repetition rate changes and maximally sensitive to optical frequency changes.

Generating an error signal for stabilizing the repetition rate is more difficult than that for frequency stabilization since the fixed point for cavity length changes affecting the optical frequency is outside the optical spectrum bandwidth. To generate an error signal insensitive to frequency fluctuations, a difference is taken between error signals from opposite edges of the spectrum. Consider an error signal proportional to frequency fluctuations of a comb line from the short wavelength, blue side of the spectrum, $V_b \propto \delta\nu_b = \delta\nu_o + n_b \cdot \delta f_{rep}$, and likewise $V_r \propto \delta\nu_r = \delta\nu_o + n_r \cdot \delta f_{rep}$ for an error signal from the red wavelength side. The difference of these error signals only contains contributions from the repetition rate fluctuations, $V_b - V_r \propto (n_b - n_r) \cdot \delta f_{rep}$. This difference signal can be conditioned and applied to a phase shifter in the optoelectronic loop to stabilize the repetition rate. A summary of the fixed points, error signal generation, and feedback locations is illustrated in Figure 5.6.

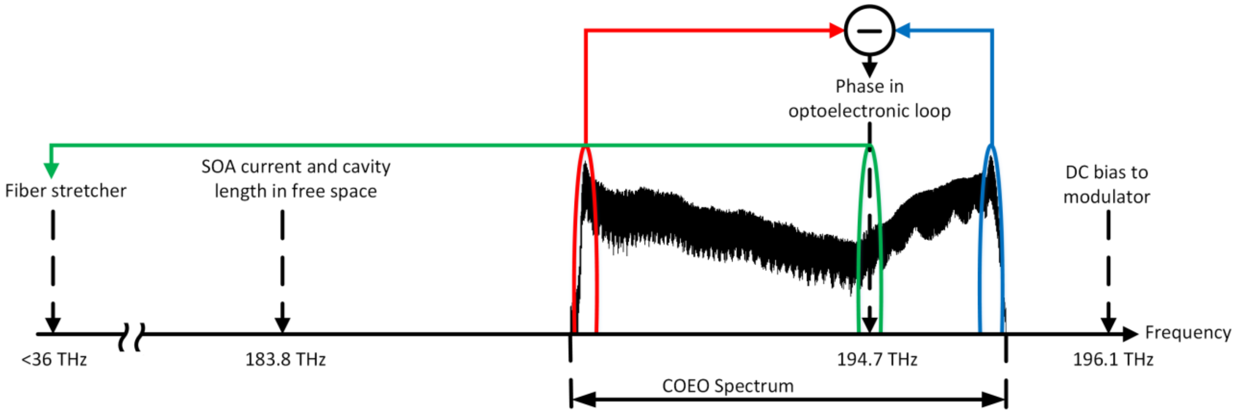

Figure 5.6 Summary of three-point PDH stabilization scheme. Black dashed arrows indicate fixed point frequencies for various parameters. Colored lines indicate the region of spectrum used for error signal generation and to which parameter the error signal is fed back.

5.3 Experimental Results

5.3.1 COEO Characterization

Figure 5.7a shows the optical spectrum of the COEO spanning 8.7 nm. The Waveshaper is used to intentionally limit the COEO spectrum due to the regeneratively mode-locked COEO being free to drift in repetition rate and becoming less stable as bandwidth increased. Figure 5.7b shows a pulse autocorrelation width of 2.4 ps (2.6 times transform-limited) and the RF spectrum of the pulse train in Figure 5.7c shows a repetition rate of 10.285 GHz.

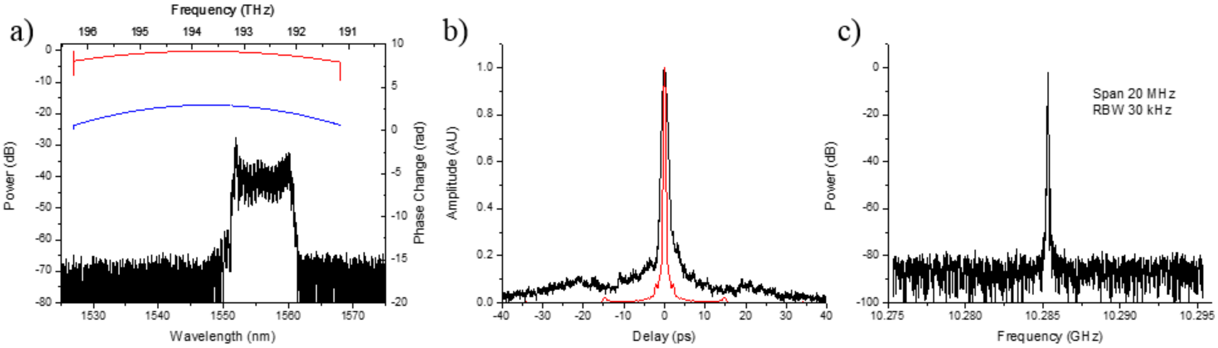

Figure 5.7 Characterization of frequency stabilized COEO. a) Optical spectrum. b) Pulse intensity autocorrelation. c) RF spectrum.

As the COEO is a stand-alone oscillator, residual phase noise cannot be measured as done previously. Absolute phase noise could not be measured either due to the lack of a second oscillator capable of following the COEO frequency via a phase locked loop. As an initial characterization of the stability of the COEO repetition rate, a Max Hold measurement of the RF spectrum was made over the course of one minute. The Max Hold function of an RF spectrum analyzer stores the maximum value measured in each frequency bin over the duration of the measurement. In this way, the maximum extent of fluctuations in the repetition rate over the chosen time period can be determined.

In Figure 5.8, Max Hold measurements of the repetition rate are presented when only the COEO's optical frequency is being stabilized via feedback to the piezo fiber stretcher. No attempt was made here to directly stabilize the repetition rate through feedback to the optoelectronic loop phase shifter. Figure 5.8a shows the stability when the entire optical spectrum is allowed to contribute to the error signal used for stabilization, while Figure 5.8b is the result when a 0.7 nm wide optical BPF is used to select a small segment of the spectrum for error signal generation. Using a single narrow spectral slice for stabilization leads to a drift in repetition rate of 200 Hz over the course of one minute, a more than twofold improvement over when the entire spectrum is used. This improvement is a result of less comb lines contributing to the error signal, providing a cleaner signal that can be stabilized to a finer level. A downside of using less comb lines is a reduction in optical power at the detector and thus a reduction in the error signal SNR, but this can be overcome with the added complexity of another optical amplifier.

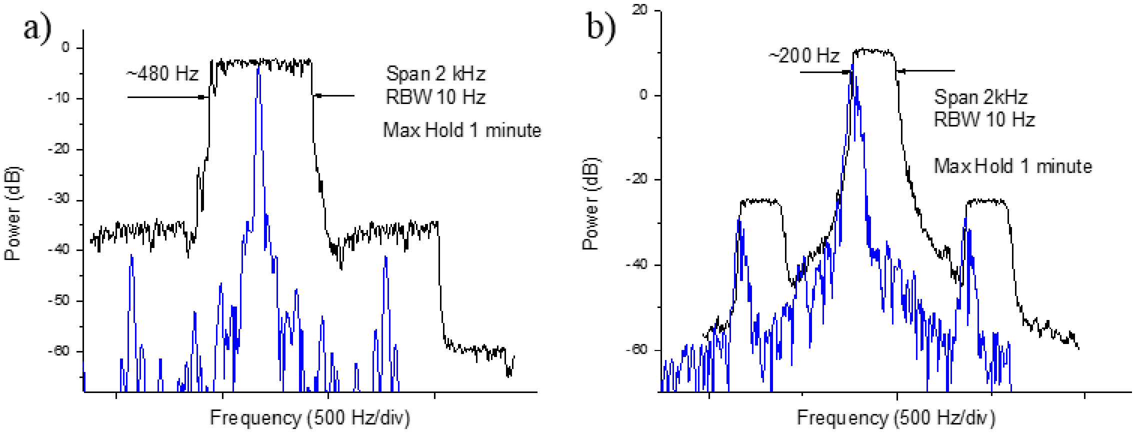

Figure 5.8 COEO repetition rate stability. Black traces are the Max Hold measurements and blue traces are single sweep measurements. a) Stability when entire optical spectrum contributes to error signal. b) Stability when narrow filtered region of spectrum is used for error signal generation.

5.3.2 Three-point PDH Error Signal Generation

The previous section illustrated the benefit of a single point PDH lock over an "all points" lock where the entire optical spectrum contributes to the error signal. Implementation of the full three-point PDH stabilization where the difference signal from the spectrum edges is used to stabilize the COEO repetition rate should improve stability, but preliminary efforts found feedback to the OE loop RF phase shifter tended to have a destabilizing effect. To better understand the source of this effect, we studied the behavior of the three generated error signals in response to different fluctuations in the optical spectrum. The three-point error signal generation is implemented by power dividing the phase modulated spectrum after reflection from the FPE into three channels with approximately a 30/35/35 power distribution. Each channel is filtered with a 0.7 nm wide tunable BPF centered at a different wavelength and then photodetected, amplified, and mixed with a phase reference to produce an error signal.

Figure 5.9a illustrates conceptually how the error signals change when the relevant comb lines are swept across their associated FPE resonance due the fiber stretcher changing the offset frequency. For illustrative purposes, the repetition rate is taken to be slightly less than the FPE FSR, such that the three comb lines are swept through the FPE at different times with the lowest frequency comb line passing through first. In this case, the error signals exhibit correlated motion with some delay related to the difference in repetition rate and FSR. If the repetition rate matches the FSR, the error signals would be perfectly correlated with zero delay, and for a repetition rate greater than the FSR, the error signal from the high frequency comb line would lead that from the low frequency comb line.

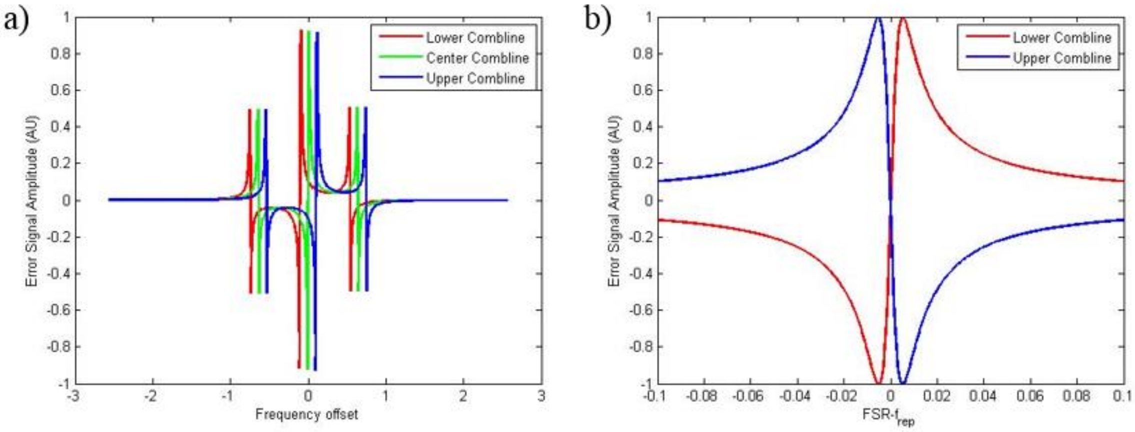

Figure 5.9 Correlated and anti-correlated error signal behavior, assuming $f_{rep} < FSR_{FPE}$. a) Optical frequency sweep shows correlated movement of error signals with delay. b) Repetition rate sweep with locked center comb line shows anti-correlated movement of outer comb lines' error signals.

Once the error signal from the center comb line has been used to lock the optical frequency, the repetition rate is still free to drift due to changes in the optoelectronic loop phase. Figure 5.9b simulates the error signal behavior when the repetition rate is swept from less than to greater than the FPE FSR while maintaining a lock on the center comb line. In this situation, the outer comb lines will symmetrically expand and contract about the center frequency. The comb lines will pass through the etalon resonances at the same time but in different directions, leading to anti-correlated changes in the error signals.

Experimentally, we were able to lock the center comb line frequency and study the fluctuations in the outer comb lines' error signals. Figure 5.10 is a series of three snapshots taken at 2 second intervals of the error signals as measured on an oscilloscope. The center green trace is the error signal from the middle of the spectrum, and it remains locked and unmoving over the course of the measurement. The top cyan trace is the error signal from the high frequency blue side of the spectrum and the bottom pink trace is the error signal from the low frequency red side of the spectrum. Through these three snapshots, there is clear anti-correlated movement between the blue- and red-side error signals as expected. However, we also observed correlated fluctuations where both error signals moved in the same direction despite the center error signal remaining locked. These unexpected fluctuations, likely due to variations in system parameters with nearby fixed point frequencies, seem to be the cause of difficulty in stabilizing the difference signal. Further investigation of the error signals may determine how to mitigate these fluctuations.

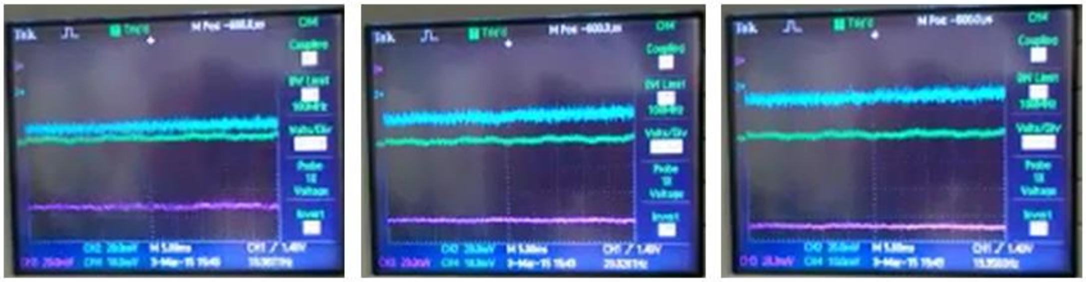

Figure 5.10 Time lapse of error signal movements while the center frequency is locked. The blue, green, and pink traces are the error signals from the short, mid, and long wavelength regions of the spectrum, respectively.

CHAPTER 6: CONCLUSION AND FUTURE WORK

6.1 Summary

The focus of the work in this dissertation has been to improve the performance of semiconductor mode-locked lasers by increasing their spectral bandwidth. A broader bandwidth is beneficial for many telecom applications such as wavelength division multiplexing, and it also enables the production of shorter pulses which benefit several time-domain applications. Dispersion in the external fiber cavity is the primary factor limiting the bandwidth of semiconductor lasers of the design discussed in this dissertation. This interplay between dispersion and bandwidth is related to how evenly spaced the cavity modes are across the spectral region of interest, such that they do not walk off from the periodic Fabry-Pérot etalon resonances nor the evenly spaced sidebands generated via the intensity modulator. Any mismatch between the mode-locking frequency driving the modulator and the etalon FSR also acts to limit the bandwidth.

To study dispersion in our laser cavities, we developed an efficient multi-heterodyne measurement technique that enabled accurate, self-referenced measurements of an optical frequency comb’s spectral phase. Using this technique, we characterized three different semiconductor based comb sources and quantified their quadratic and cubic phase coefficients. These phase measurements then served as a starting point for programmatically compensating the cavity dispersion using an intracavity pulseshaper. Optimizing the amplitude and phase masks applied to the pulseshaper lead to record bandwidth obtained from a GHz repetition rate semiconductor mode-locked laser. Spectra were limited by the pulseshaper transmission window and spanned 5 THz, containing 500 individual comb lines. In the time domain, sub-picosecond pulses were produced with femtosecond level timing jitter.

This system was converted to a coupled opto-electronic oscillator by photodetecting the output and using that signal to drive the intracavity intensity modulator. This eliminated the need for an external, low noise microwave oscillator, but also allowed the repetition rate to drift. To stabilize both the repetition rate and optical frequency, a novel three-point Pound-Drever-Hall scheme was developed and demonstrated. The use of three unique error signals from different regions of the optical spectrum allows us to decouple and independently stabilize fluctuations in the repetition rate and frequency. The COEO repetition rate of 10 GHz demonstrated a drift of just 200 Hz over a period of one minute, and further development of the three-point PDH scheme is expected to improve this stability.

6.2 Future Work

6.2.1 Automated Waveshaper Mask Optimization

Development of an algorithm to automatically optimize the Waveshaper mask would be a boon to the advancement of this laser architecture. Manually adjusting the applied masks to increase the lasing bandwidth is a time-consuming process that consists of repeatedly making slight modifications and observing the response of the system. One potential solution would be an automated routine which systematically varies the amplitude and phase mask polynomial coefficients while making measurements of the optical and RF spectra to evaluate the lasing bandwidth and the presence of any supermode spurs.

6.2.2 COEO Repetition Rate Stability Improvement

With regards to the three-point Pound-Drever-Hall scheme in the coupled opto-electronic oscillator, more work is required to be able to use the difference signal between the spectrum edges' error signals to stabilize the opto-electronic loop phase and hence the COEO repetition rate.

Changing the center wavelength of the filtered spectrum edges and increasing the bandpass filters' width may increase the optical power contributing to the error signals and result in stronger signals to which to lock. Once this has been implemented, a possibility for future improvement would be to compress the output pulses to near transform-limited and then pass them through highly nonlinear fiber to generate nonlinear broadening of the spectrum. Error signals could then be obtained from the edges of the broadened spectrum, improving the difference signal's sensitivity to repetition rate fluctuations.

APPENDIX A:
MATLAB CODE FOR MULTI-HETERODYNE PHASE RETRIEVAL

Top Script

```
tic; format long; clc; close all
clearvars -except data pn fn data1 pn1 fn1 fMeas aMeas pksMeas LocsMeas a2MI
f2Meas a2Meas

global frepLow fA frepHigh fB tB threshold offset ZeroIndex delta deltaIndex
df
global kmax Nc nPeriods NH EO fMeas aMeas pksMeas LocsMeas strtFrqInd a2MI
%% User Parameters
offset=.5; Ns=1; numLengths=24;

% 7/10/12 Chuck Laser %thresh=-107
threshold=-110; frepHigh=10.250984e9; frepLow=250e6; Nc=90; nPeriods=6;

%% Import the data file
%     fn='71012MHA000.txt';pn='H:\Home\UP\acklee\Lab Data\2012\7_10_12\';
% %     pn='\\s3.creol.ucf.edu\Home\UP\acklee\Lab Data\2012\7_10_12';
% [fn,pn]=uigetfile('Pathname’,'Get MH Signal');
% A=importdata([pn fn]); data=A.data; clear A

%% Calculate relevant parameters
dt=data(2,1)-data(1,1);
delta=rem(frepHigh,frepLow); NH=floor(frepHigh/frepLow); kmax=NH+1;
EO=rem(NH,2);

%% RF Peak Location and Spectral Retrieval
L0=ceil(nPeriods/delta/dt);
PeaksAllFFTs=zeros(Nc,2,kmax,numLengths,Ns);
Peaks=zeros(kmax,Nc,Ns); PeakLocs=zeros(kmax,Nc,Ns);
% Peak=[Combline #, Frq or Amp, Beat set #, FFT length iter., Time Chunk]
% TempPeaksAllFFTs=zeros(Nc,2,kmax);

for m=1:Ns
    for j=1:numLengths
        dL=-numLengths+(j-1)*4;
        L=L0+dL; T=L*dt; df=1/T;
        frq=linspace((-L/2)*df, (L/2-1)*df,L); frq=frq';
        x0=floor(1+(m-1)*L*offset); %index shift of FT window
        window=blackmanharris(L);

        Iw=fftshift(1/L*fft(data(x0:x0+L-1,2).*window)); %FT
        [PeaksAllFFTs(:,:,:,j,m)] = MH_Peak_Locator_v25b(Iw,frq);

%          figure(500)
%
plot(squeeze(PeaksAllFFTs(:,1,:,j,1)),10*log10(abs(squeeze(PeaksAllFFTs(:,2,:
,j,1))).^2),'.');hold all
    end

%     figure(500)
%     plot(frq,10*log10(abs(Iw).^2))
```

```
    [Peaks(:,:,m),PeakLocs(:,:,m)]=MH_TruePeaks_v28(PeaksAllFFTs);
    plot(frq,10*log10(abs(Iw).^2));
    [dPhiA,PhiA,MagA,dPhiB,PhiB,MagB] =
MH_AmpPhase_Retrieval_v27(Peaks(:,:,m));

MH_RFSpectrum_Plots_v27(frq,Iw,PeakLocs(:,:,m),Peaks(:,:,m),dPhiA,MagA,PhiA,d
PhiB,MagB,PhiB)
end
toc
```

Peak Locator Function

```
function [Peaks] =
MH_Peak_Locator_v25b(Iw,frq)%,threshold,frepLow,frq,nPeriods,ZeroIndex,kmax,d
f,Nc)

global frepLow
global threshold
global nPeriods
global ZeroIndex
global kmax
global Nc

% figure(100);clf
% plot(frq,10*log10(abs(Iw).^2));hold on

%Initialize arrays
Peaks=zeros(Nc,2,kmax);
PeakVals=zeros(Nc,kmax);
PeakLocs=zeros(Nc,kmax);
df=frq(2)-frq(1);

%Find starting beat note and distance in index values from 0, thus
%giving theoretical start position of every beat set

% % ind = find(10*log10(abs(Iw))>threshold & frq>.03*frepLow &
frq<(.45*frepLow));   %Every point above threshold in first beat set
% % % ind = find(10*log10(abs(Iw))>threshold & frq>.0677*frepLow &
frq<(.45*frepLow));   %Every point above threshold in first beat set
% % dMinInd=find(10*log10(abs(Iw))==max(10*log10(abs(Iw(ind(1)-
floor(nPeriods/2):ind(1)+floor(nPeriods/2))))) & frq>0); %Find first peak
within range of +- nPeriods
% % dMin=dMinInd-ZeroIndex; %Index offset from 0
% % dMI=dMinInd;

%Use N_H beat set for identification
ind = find( 10*log10(abs(Iw).^2)>threshold & frq>1.001*(kmax-2)/2*frepLow ...
    & frq<((kmax-1)/2*frepLow));
dMinInd = find(10*log10(abs(Iw).^2)==max(10*log10(abs(Iw(ind(1)-
floor(nPeriods/2):...
    ind(1)+floor(nPeriods/2))).^2)) & frq>0); %Find first peak within range
of +- nPeriods
maxHarmInd=find(abs(frq-(kmax-2)/2*frepLow)<df/2);
```

```
dMin=dMinInd-maxHarmInd;
dMI=dMin+ZeroIndex;

calb=0;
for k=1:kmax
    R=rem(k,2);
    %Correction for slightly incorrect rep-rates and rep-rate harmonics
    %not being integer multiples of frq spacing (df)
    if k==1
        calb=0;
    else
        harmonic=floor(k/2)*frepLow; %Theoretical harmonic of frepLow
        harm1 = find(abs(frq-harmonic)<df/2); %"Nearest" frequency available
        %Look for a harmonic peak near harm1. Shifted by previous calb factor
        realHarm = find(10*log10(abs(Iw))==max(10*log10(abs(Iw(harm1-...
            floor(nPeriods/2)+calb:harm1+floor(nPeriods/2)+calb)))) & frq>0);
        %Index difference between theoretical harmonic location and located
peak
        calb=floor(abs(frq(realHarm)-harmonic)/df).*sign(frq(realHarm)-
harmonic);
    end

    %Set starting beat frequency for given beat set. Start is frequency
    %closest to harmonic of frepLow. -> Even k's search going to
    %smaller f, Odd k's search going to larger f

    %Lower and Upper index bounds of given beat set
    lowI=find(abs(frq-(k-1)/2*frepLow)<df/2);
    highI=find(abs(frq-k/2*frepLow)<df/2);

    low  = highI + R*(lowI-highI) + (2*R-1)*dMin - floor(nPeriods/2)+calb;
    high = highI + R*(lowI-highI) + (2*R-1)*dMin + floor(nPeriods/2)+calb;

    start=find(10*log10(abs(Iw).^2)==max(10*log10(abs(Iw(low:high)).^2)) &
frq>0);

    beatPos=start;
    Peaks(Nc+R*(1-Nc),1,k) = frq(start);
    Peaks(Nc+R*(1-Nc),2,k) = Iw(start);

    for l=2:Nc %Locate all beat notes in given beat set
        [~,temp]=max(10*log10(abs(Iw(beatPos+(2*R-1)*nPeriods-1:beatPos+(2*R-
1)*nPeriods+1)).^2));
        beatPos=(beatPos+(2*R-1)*nPeriods-1)-1+temp;

        Peaks((Nc+1-l)+R*(l-(Nc+1-l)),1,k) = frq(beatPos);
        Peaks((Nc+1-l)+R*(l-(Nc+1-l)),2,k) =  Iw(beatPos);
%         plot(frq(beatPos),10*log10(abs(Iw(beatPos)).^2),'r.')
    end

%     plot(Peaks(:,1,k),10*log10(abs(Peaks(:,2,k)).^2),'r.')
end
```

```
% PeakVals(:,:)=Peaks(:,2,:);
% PeakLocs(:,:)=Peaks(:,1,:);
```

Function for aggregating multiple FFTs of different zero-padded lengths

```
function [Peaks,PeakLocs]=MH_TruePeaks_v28(PeaksAllFFTs)

global kmax Nc delta df
Peaks=zeros(kmax,Nc); PeakLocs=zeros(kmax,Nc);
for k=1:kmax
        for i=1:Nc
            Temp=[]; minPointSep=5e4;
            Temp(:,1) = squeeze(PeaksAllFFTs(i,1,k,:,1));
Temp(:,2)=squeeze(PeaksAllFFTs(i,2,k,:,1));  Temp=sortrows(Temp);
            medPos=median(Temp(:,1)); badPoints=abs(Temp(:,1)-
medPos)>delta/2; Temp(badPoints,:)=[];
            badPoints=[]; badPoints=(Temp(2:end,1)- Temp(1:end-
1,1))>minPointSep;
            numBreaks=sum(badPoints);
            for w=1:numBreaks
                badPoints=[];
                badPoints=(Temp(2:end,1)- Temp(1:end-1,1))>minPointSep;
                [~,ind]=max(badPoints);
                if Temp(ind+1)>medPos
                    Temp(ind+1:end,:)=[];
                else
                    Temp(1:ind,:)=[];
                end
            end

            medAmp=median(10*log10(abs(Temp(:,2)).^2));
badPoints=10*log10(abs(Temp(:,2)).^2)< medAmp-5; Temp(badPoints,:)=[];
            opts=optimset('Display','off','MaxFunEvals',1000);

[bestcoeffs,error,exitflag,output]=fminsearch(@SincFit,[max(abs(Temp(:,2)))
1/df mean(Temp(:,1)) 0],opts,Temp(:,1),abs(Temp(:,2)));
            warning('off','MATLAB:polyfit:RepeatedPointsOrRescale');

p=polyfit(Temp(:,1),(unwrap(angle(Temp(:,2)))+2*pi*(angle(Temp(floor(length(T
emp)/2),2))>.5*pi)),1);

            PeakLocs(k,i)=bestcoeffs(3);

Peaks(k,i)=(bestcoeffs(1)+bestcoeffs(4)).*exp(1i*(p(1)*bestcoeffs(3)+p(2)));

            %%
            figure(900);
            a=rand(1);b=rand(1);c=rand(1);
            plot(Temp(:,1),10*log10(abs(Temp(:,2)).^2),'.','Color',[a b c]);
hold on
            yfit=bestcoeffs(1)*sinc(bestcoeffs(2)*(Temp(:,1)-bestcoeffs(3)))+
bestcoeffs(4);
            plot(Temp(:,1),10*log10(abs(yfit).^2),'r');
            plot(Temp(:,1),angle(Temp(:,2))/pi-90,'.','Color',[a b c]);
```

```
plot(Temp(:,1),(unwrap(angle(Temp(:,2)))+2*pi*(angle(Temp(floor(length(Temp)/
2),2))>.5*pi))/pi-90,'o','Color',[a b c])
            plot(PeakLocs(k,i),10*log10(abs(Peaks(k,i)).^2),'k*')
            plot(PeakLocs(k,i),angle(Peaks(k,i))/pi-90,'k.')
        end
end
```

Amplitude and Phase Retrieval Function

```
function [dPhiA,PhiA,MagA,dPhiB,PhiB,MagB] = MH_AmpPhase_Retrieval_v27(Peaks)

global Nc NH kmax EO

%Initialize
PhiA=zeros(Nc*NH+1,1);MagA=ones(Nc*NH+1,1);
dPhiA=zeros(Nc*NH,1);dMagA=zeros(Nc*NH,1);
PhiB=zeros(Nc,1);MagB=ones(Nc,1);
dPhiB=zeros(Nc-1,1);dMagB=zeros(Nc-1,1);

%CombA(Low) Retrieval
for y=1:Nc %Number of comblines in a beat set
    for x=1:NH  %Step through beat sets except Z-1
        k1=kmax-2*(x-1)-EO; n1=y; pm1=1;
        k2=kmax-2*x-EO;     n2=y; pm2=1;
        if k1<1
            k1=abs(k1)+1;
            n1=Nc+1-y;
            pm1=-1;
        end
        if k2<1
            k2=abs(k2)+1;
            n2=Nc+1-y;
            pm2=-1;
        end

        dPhiA((y-1)*NH+x)=pm1*angle(Peaks(k1,n1))-pm2*angle(Peaks(k2,n2));
        dMagA((y-1)*NH+x)=abs(Peaks(k2,n2))/abs(Peaks(k1,n1));
        %              dMagA((y-
1)*NH+x,j)=sqrt(abs(Peaks(k2,n2,j)))/sqrt(abs(Peaks(k1,n1,j)));

        if (y-1)*NH+x > 1
            diff = dPhiA((y-1)*NH+x) - dPhiA((y-1)*NH+x-1);
            if abs(diff)>1.5*pi
                dPhiA((y-1)*NH+x)=dPhiA((y-1)*NH+x)-sign(diff)*2*pi;
            end
        end

        PhiA((y-1)*NH+x+1)=dPhiA((y-1)*NH+x)+PhiA((y-1)*NH+x);
        MagA((y-1)*NH+x+1)=dMagA((y-1)*NH+x)*MagA((y-1)*NH+x);
    end
end
```

```
%CombB(High) Retrieval
piShiftedVals=[];

dPhiB(1:Nc-1)=angle(Peaks(kmax-EO,2:Nc))+angle(Peaks(kmax-1+EO,Nc:-1:2));
dMagB(1:Nc-1)=abs(Peaks(kmax-EO,2:Nc))./abs(Peaks(kmax-1+EO,Nc:-1:2));

diff = dPhiB(2:Nc-1) - dPhiB(1:Nc-2);
diff=diff -(abs(diff)>1.5*pi).*sign(diff)*2*pi;
diff=diff -(abs(diff)>.8*pi ).*sign(diff)*1*pi;
dPhiB(2:Nc-1)=dPhiB(1)+cumsum(diff);

PhiB(2:Nc)=PhiB(1)+cumsum(dPhiB);
MagB(2:Nc)=MagB(1)*cumprod(dMagB);
```

Various Plots Function

```
function
MH_RFSpectrum_Plots_v27(frq,Iw,PeakLocs,Peaks,dPhiA,MagA,PhiA,dPhiB,MagB,PhiB
)

global frepLow
global frepHigh
global kmax

fA=(1:length(MagA))*frepLow;
fB=(1:length(MagB))*frepHigh;

figure
subplot(2,4,[1,2,3,4]); %Plot RF Spectrum with identified Peaks
plot(frq/1e9,10*log10(abs(Iw).^2),'b'); hold on
plot(PeakLocs(:,:)/1e9,10*log10(abs(Peaks(:,:)).^2),'ro'); hold off
axis([(kmax-2)*frepLow/2/1e9  kmax*frepLow/2/1e9 -130 -85])
title('Multi-heterodyne Spectrum: Beat Sets Nd & Nd+1')
xlabel('Frequency (GHz)');ylabel('Power Spectrum (dB)');

subplot(2,4,5); %Plot dPhiA
plot(fA(1:end-1),dPhiA*1e9/(frepLow*2*pi),'bo')
title('Low Rep Rate Group Delay'); ylabel('Group Delay (ns)');
xlabel('Frequency (GHz)')
xlim([0 fA(end)])

subplot(2,4,6) %Plot Comb A Magnitude and Phase
set(gcf,'DefaultAxesColorOrder',[0 0 1;0 0 1])
[AX,H1,H2]=plotyy(fA,10*log10(MagA.^2)-
min(10*log10(MagA.^2)),fA,detrend(PhiA),'stem','plot');
set(H1,'Marker','none');set(H2,'Marker','o')
linkaxes([AX(1),AX(2)],'x')
set(get(AX(1),'Ylabel'),'String','Power Spectrum (dB)');
set(AX(1),'YLim',[min(10*log10(MagA.^2)-min(10*log10(MagA.^2)))
max(10*log10(MagA.^2)-min(10*log10(MagA.^2)))+30]);
set(get(AX(2),'Ylabel'),'String','Phase (rad)');
set(AX(2),'YLim',[min(detrend(PhiA))-60 max(detrend(PhiA))+5]);
title('Comb "A" Optical Spectrum');xlabel('Frequency [GHz]')
```

```
xlim([0 fA(end)])

subplot(2,4,7); %Plot dPhiB
plot(fB(1:end-1),dPhiB*1e9/(frepHigh*2*pi),'ro')
title('High Rep Rate Group Delay'); ylabel('Group Delay (ns)');
xlabel('Frequency (GHz)')
xlim([0 fB(end)])

subplot(2,4,8); %Plot Comb B Magnitude and Phase
set(gcf,'DefaultAxesColorOrder',[1 0 0;1 0 0])
[AX,H1,H2]=plotyy(fB,10*log10(MagB.^2)-
min(10*log10(MagB.^2)),fB,detrend(PhiB),'stem','plot');
set(H1,'Marker','none');set(H2,'Marker','o');
linkaxes([AX(1),AX(2)],'x');
set(get(AX(1),'Ylabel'),'String','Power Spectrum (dB)');
set(AX(1),'YLim',[min(10*log10(MagB.^2)-min(10*log10(MagB.^2)))
max(10*log10(MagB.^2)-min(10*log10(MagB.^2)))+30]);
set(get(AX(2),'Ylabel'),'String','Phase (rad)');
set(AX(2),'YLim',[min(detrend(PhiB))-60 max(detrend(PhiB))+5]);
title('Comb "B" Optical Spectrum');xlabel('Frequency (GHz)');xlim([0
fB(end)])
```

APPENDIX B: COPYRIGHT PERMISSION

IEEE Copyright Permission

Requirements to be followed when using any portion (e.g., figure, graph, table, or textual material) of an IEEE copyrighted paper in a thesis:

1) In the case of textual material (e.g., using short quotes or referring to the work within these papers) users must give full credit to the original source (author, paper, publication) followed by the IEEE copyright line © 2011 IEEE.
2) In the case of illustrations or tabular material, we require that the copyright line © [Year of original publication] IEEE appear prominently with each reprinted figure and/or table.
3) If a substantial portion of the original paper is to be used, and if you are not the senior author, also obtain the senior author's approval.

Requirements to be followed when using an entire IEEE copyrighted paper in a thesis:

1) The following IEEE copyright/ credit notice should be placed prominently in the references: © [year of original publication] IEEE. Reprinted, with permission, from [author names, paper title, IEEE publication title, and month/year of publication]
2) Only the accepted version of an IEEE copyrighted paper can be used when posting the paper or your thesis on-line.
3) In placing the thesis on the author's university website, please display the following message in a prominent place on the website: In reference to IEEE copyrighted material which is used with permission in this thesis, the IEEE does not endorse any of [university/educational entity's name goes here]'s products or services. Internal or personal use of this material is permitted. If interested in reprinting/republishing IEEE copyrighted material for advertising or promotional purposes or for creating new collective works for resale or redistribution, please go tohttp://www.ieee.org/publications_standards/publications/rights/rights_link.html to learn how to obtain a License from RightsLink.

If applicable, University Microfilms and/or ProQuest Library, or the Archives of Canada may supply single copies of the dissertation.

REFERENCES

[1] S. A. Diddams, et al., "Design and control of femtosecond lasers for optical clocks and the synthesis of low-noise optical and microwave signals," *IEEE J. Sel. Topics Quantum Electron.,* **9**, 1072-1080,(2003).

[2] D. J. Jones, et al., "Carrier-envelope phase control of femtosecond mode-locked lasers and direct optical frequency synthesis," *Science,* **288**, 635-639,(2000).

[3] S. A. Diddams, et al., "An optical clock based on a single trapped (199)Hg(+) ion," *Science,* **293**, 825-828,(2001).

[4] J. Ye, et al., "Precision phase control of an ultrawide-bandwidth femtosecond laser: a network of ultrastable frequency marks across the visible spectrum," *Opt. Lett.,* **25**, 1675-1677,(2000).

[5] L. E. Hargrove, et al., "Locking og He–Ne Laser Modes Induced by Synchronous Intracavity Modulation," *Appl Phys Lett,* **5**, 4-5,(1964).

[6] E. Braun, et al., *Revolution in Miniature: The History and Impact of Semiconductor Electronics*. New York, NY: Cambridge University Press, 1982.

[7] P. J. Delfyett, et al., "Signal processing at the speed of lightwaves," *Ieee Circuits Device,* **18**, 28-35,(2002).

[8] B. L. Shoop, *Photonic Analog-to-Digital Conversion*. New York: Springer, 2001.

[9] G. C. Valley, "Photonic analog-to-digital converters," *Opt. Express,* **15**, 1955-1982,(2007).

[10] E. W. Jacobs, et al., "Optically clocked track-and-hold for high-speed high-resolution analog-to-digital conversion," in *Microwave Photonics, 2004. MWP'04. 2004 IEEE International Topical Meeting on*, 4-6 Oct. 2004 2004, pp. 190-192.

[11] P. W. Juodawlkis, et al., "Optically sampled analog-to-digital converters," *Microwave Theory and Techniques, IEEE Transactions on,* **49**, 1840-1853,(2001).

[12] M. Johansson, et al., "Study of an ultrafast analog-to-digital conversion scheme based on diffractive optics," *Appl Optics,* **39**, 2881-2887,(2000).

[13] H. F. Taylor, "Optical Analog-to-Digital Converter - Design and Analysis," *IEEE J. Quantum Electron.,* **15**, 210-216,(1979).

[14] I. Ozdur, et al., "A Semiconductor-Based 10-GHz Optical Comb Source With Sub 3-fs Shot-Noise-Limited Timing Jitter and similar to 500-Hz Comb Linewidth," *IEEE Photon. Technol. Lett.,* **22**, 431-433,(2010).

[15] I. Coddington, et al., "Coherent multiheterodyne spectroscopy using stabilized optical frequency combs," *Phys. Rev. Lett.,* **100**, 013902,(2008).

[16] I. Coddington, et al., "Coherent dual-comb spectroscopy at high signal-to-noise ratio," *Phys. Rev. A,* **82**, 043817,(2010).

[17] E. Baumann, et al., "Spectroscopy of the methane nu(3) band with an accurate midinfrared coherent dual-comb spectrometer," *Phys. Rev. A,* **84**, 062513,(2011).

[18] A. M. Zolot, et al., "Broad-band frequency references in the near-infrared: Accurate dual comb spectroscopy of methane and acetylene," *J Quant Spectrosc Ra,* **118**, 26-39,(2013).

[19] P. Giaccari, et al., "Active Fourier-transform spectroscopy combining the direct RF beating of two fiber-based mode-locked lasers with a novel referencing method," *Opt. Express,* **16**, 4347-4365,(2008).

[20] J. D. Deschenes, et al., "Optical referencing technique with CW lasers as intermediate oscillators for continuous full delay range frequency comb interferometry," *Opt. Express,* **18**, 23358-23370,(2010).

[21] T. Ideguchi, et al., "Adaptive dual-comb spectroscopy in the green region," *Opt. Lett.,* **37**, 4847-4849,(2012).

[22] T. Ideguchi, et al., "Adaptive real-time dual-comb spectroscopy," *arXiv preprint arXiv:1201.4177*, 2012).

[23] B. Bernhardt, et al., "Cavity-enhanced dual-comb spectroscopy," *Nat. Photon.,* **4**, 55-57,(2010).

[24] A. M. Zolot, et al., "Direct-comb molecular spectroscopy with accurate, resolved comb teeth over 43 THz," *Opt. Lett.,* **37**, 638-640,(2012).

[25] G. Rieker, et al., "Open-Path Dual-Comb Spectroscopy of Greenhouse Gases," 2013, p. CTh5C.9.

[26] T. Ideguchi, et al., "Raman-induced Kerr-effect dual-comb spectroscopy," *Opt. Lett.,* **37**, 4498-4500,(2012).

[27] A. Hipke, et al., "Highly Multiplexed Dual-Comb Two-Photon Excitation Spectroscopy," in *CLEO: Science and Innovations*2013.

[28] A. L. Schawlow, et al., "Infrared and optical masers," *Physical Review,* **112**, 1940,(1958).

[29] T. A. Yilmaz, et al., "Noise in fundamental and harmonic modelocked semiconductor lasers: Experiments and simulations," *IEEE J. Quantum Electron.,* **39**, 838-849,(2003).

[30] C. Williams, et al., "Injection-Locked Mode-Locked Laser With Long-Term Stabilization and High Power-per-Combline," *IEEE Photon. Technol. Lett.,* **21**, 94-96,(2009).

[31] S. Gee, et al., "Simultaneous optical comb frequency stabilization and super-mode noise suppression of harmonically mode-locked semiconductor ring laser using an intracavity etalon," *IEEE Photon. Technol. Lett.,* **17**, 199-201,(2005).

[32] J. Davila-Rodriguez, et al., "Ultralow Noise, Etalon Stabilized, 10 GHz Optical Frequency Comb Based on a SCOW Amplifier," *IEEE Photon. Technol. Lett.,* **24**, 2159-2162,(2012).

[33] H. Lee, et al., "Ultra-low-loss optical delay line on a silicon chip," *Nat Commun,* **3**, 867,(2012).

[34] J. F. Bauters, et al., "Planar waveguides with less than 0.1 dB/m propagation loss fabricated with wafer bonding," *Opt. Express,* **19**, 24090-24101,(2011).

[35] A. Bartels, et al., "Passively mode-locked 10 GHz femtosecond Ti : sapphire laser," *Opt. Lett.,* **33**, 1905-1907,(2008).

[36] T. M. Fortier, et al., "Octave-spanning Ti : sapphire laser with a repetition rate > 1 GHz for optical frequency measurements and comparisons," *Opt. Lett.,* **31**, 1011-1013,(2006).

[37] A. Bartels, et al., "Spectrally resolved optical frequency comb from a self-referenced 5 GHz femtosecond laser," *Opt. Lett.,* **32**, 2553-2555,(2007).

[38] T. R. Schibli, et al., "Optical frequency comb with submillihertz linewidth and more than 10 W average power," *Nat. Photon.,* **2**, 355-359,(2008).

[39] I. Hartl, et al., "Fully Stabilized GHz Yb-Fiber Laser Frequency Comb," in *Advanced Solid-State Photonics,* Denver, Colorado, 2009/02/01 2009, p. MF9.

[40] F. Quinlan, et al., "Ultralow phase noise microwave generation with an Er:fiber-based optical frequency divider," *Opt. Lett.,* **36**, 3260-3262,(2011).

[41] B. R. Washburn, et al., "Fiber-laser-based frequency comb with a tunable repetition rate," *Opt. Express,* **12**, 4999-5004,(2004).

[42] P. Del'Haye, et al., "Octave Spanning Tunable Frequency Comb from a Microresonator," *Phys. Rev. Lett.,* **107**, 063901,(2011).

[43] A. A. Savchenkov, et al., "Tunable optical frequency comb with a crystalline whispering gallery mode resonator," *Phys. Rev. Lett.,* **101**, 093902,(2008).

[44] S. B. Papp, et al., "Parametric seeding of a microresonator optical frequency comb," *Opt. Express,* **21**, 17615-17624,(2013).

[45] M. A. Foster, et al., "Silicon-based monolithic optical frequency comb source," *Opt. Express*, **19**, 14233-14239,(2011).

[46] D. Mandridis, et al., "Low-noise, low repetition rate, semiconductor-based mode-locked laser source suitable for high bandwidth photonic analog-digital conversion," *Appl Optics*, **49**, 2850-2857,(2010).

[47] M. Akbulut, et al., "Measurement of carrier envelope offset frequency for a 10 GHz etalon-stabilized semiconductor optical frequency comb," *Opt. Express*, **19**, 16851-16865,(2011).

[48] D. S. Seo, et al., "Tuning power spectrum of semiconductor and intracavity-etalon based modelocked laser via detuning," *Electron Lett*, **49**, 1173-1174,(2013).

[49] S. Schiller, "Spectrometry with frequency combs," *Opt. Lett.*, **27**, 766-768,(2002).

[50] F. Keilmann, et al., "Time-domain mid-infrared frequency-comb spectrometer," *Opt. Lett.*, **29**, 1542-1544,(2004).

[51] S. Kray, et al., "Dual femtosecond laser multiheterodyne optical coherence tomography," *Opt. Lett.*, **33**, 2092-2094,(2008).

[52] N. R. Newbury, et al., "Low-noise fiber-laser frequency combs (Invited)," *J. Opt. Soc. Am. B*, **24**, 1756-1770,(2007).

[53] F. Ferdous, et al., "Dual-comb electric-field cross-correlation technique for optical arbitrary waveform characterization," *Opt. Lett.*, **34**, 3875-3877,(2009).

[54] J. Davila-Rodriguez, et al., "Multiheterodyne Detection for Spectral Compression and Downconversion of Arbitrary Periodic Optical Signals," *J. Lightw. Technol.*, **29**, 3091-3098,(2011).

[55] N. K. Fontaine, et al., "Simultaneous and self-referenced amplitude and phase measurement of two frequency combs using multi-heterodyne spectroscopy," in *Proc. Opt. Fiber Commun. Conf.*, Paper OW1C.1, Mar. 2012, pp. 1-3.

[56] A. Klee, et al., "Characterization of Semiconductor-Based Optical Frequency Comb Sources Using Generalized Multiheterodyne Detection," *Selected Topics in Quantum Electronics, IEEE Journal of*, **19**, 1100711-1100711,(2013).

[57] A. Klee, et al., "Generalized Spectral Magnitude and Phase Retrieval Algorithm for Self-Referenced Multiheterodyne Detection," *J. Lightw. Technol.*, **31**, 3758-3764,(2013).

[58] M. G. Taylor, "Phase Estimation Methods for Optical Coherent Detection Using Digital Signal Processing," *J. Lightw. Technol.*, **27**, 901-914,(2009).

[59] C. Williams, et al., "Stabilization of an injection locked harmonically mode-locked laser via polarization spectroscopy for frequency comb generation," in *Proc. Lasers Electro-Opt. Conf. Quantum Electron. Laser Sci.*, Paper JTH2A.50, May 2012, pp. 1-2.

[60] R. Trebino, *Frequency-resolved optical gating: the measurement of ultrashort laser pulses*: Springer, 2000.

[61] G. H. Liu, et al., "Compensation of phase noise in OFDM systems using an ICI reduction scheme," *IEEE Trans. Broadcast.,* **50**, 399-407,(2004).

[62] T. W. Hansch, et al., "Laser Frequency Stabilization by Polarization Spectroscopy of a Reflecting Reference Cavity," *Opt. Commun.,* **35**, 441-444,(1980).

[63] F. Quinlan, et al., "Self-Stabilization of the Optical Frequencies and the Pulse Repetition Rate in a Coupled Optoelectronic Oscillator," *J. Lightw. Technol.,* **26**, 2571-2577,(2008).

[64] W. Loh, et al., "Noise Figure of Watt-Class Ultralow-Confinement Semiconductor Optical Amplifiers," *IEEE J. Quantum Electron.,* **47**, 66-75,(2011).

[65] P. W. Juodawlkis, et al., "High-power 1.5-μm InGaAsP-InP slab-coupled optical waveguide amplifier," *IEEE Photon. Technol. Lett.,* **17**, 279-281,(2005).

[66] P. J. Delfyett, et al., "High-Power Ultrafast Laser-Diodes," *IEEE J. Quantum Electron.,* **28**, 2203-2219,(1992).

[67] I. Ozdur, et al., "Modified Pound-Drever-Hall scheme for high-precision free spectral range measurement of Fabry-Perot etalon," *Electron Lett,* **44**, 927-929,(2008).

[68] R. W. P. Drever, et al., "Laser Phase and Frequency Stabilization Using an Optical-Resonator," *Appl Phys B-Photo,* **31**, 97-105,(1983).

[69] R. L. Barger, et al., "Frequency Stabilization of a Cw Dye Laser," *Appl Phys Lett,* **22**, 573-575,(1973).

[70] E. D. Black, "An introduction to Pound-Drever-Hall laser frequency stabilization," *Am J Phys,* **69**, 79-87,(2001).

[71] A. Klee, et al., "Dispersion optimization in a semiconductor optical frequency comb," in *Photonics Conference (IPC), 2014 IEEE,* 12-16 Oct. 2014 2014, pp. 248-249.

[72] E. Rubiola, *Phase Noise and Frequency Stability in Oscillators*. New York: Cambridge University Press, 2009.

[73] E. Rouvalis, et al., "High-Power and High-Linearity Photodetector Modules for Microwave Photonic Applications," *J. Lightw. Technol.,* **32**, 3810-3816,(2014).

[74] F. Quinlan, et al., "Exploiting shot noise correlations in the photodetection of ultrashort optical pulse trains," *Nat. Photon.,* **7**, 290-293,(2013).

[75] X. S. Yao, et al., "Converting light into spectrally pure microwave oscillation," *Opt. Lett.,* **21**, 483-485,(1996).

[76] X. S. Yao, et al., "Dual microwave and optical oscillator," *Opt. Lett.,* **22**, 1867-1869,(1997).

[77] N. Yu, et al., "Ultralow-noise mode-locked laser with coupled optoelectronic oscillator configuration," *Opt. Lett.,* **30**, 1231-1233,(2005).

[78] E. Salik, et al., "An ultralow phase noise coupled optoelectronic oscillator," *IEEE Photon. Technol. Lett.,* **19**, 444-446,(2007).

[79] D. Eliyahu, et al., "Improving short and long term frequency stability of the opto-electronic oscillator," in *Frequency Control Symposium and PDA Exhibition, 2002. IEEE International*, 2002 2002, pp. 580-583.

[80] H. R. Telle, et al., "Kerr-lens, mode-locked lasers as transfer oscillators for optical frequency measurements," *Appl Phys B-Lasers O,* **74**, 1-6,(2002).

[81] F. Quinlan, et al., "Measurement of the comb dynamics for feedback control of an etalon-based coupled optoelectronic oscillator," *Opt. Lett.,* **33**, 1422-1424,(2008).